SIV-specific neutralizing antibody induction following selection of a PI3K drive-attenuated *nef* variant

Hiroyuki Yamamoto[*1,2,3] and Tetsuro Matano[*1,3,4]

[1]AIDS Research Center, National Institute of Infectious Diseases, 4-7-1 Gakuen, Musashi-Murayama City, Tokyo 208-0011, Japan

[2]Department of Biomedicine, University Hospital Basel, Hebelstrasse 20, Basel 4031, Switzerland

[3]Joint Research Center for Human Retrovirus Infection, Kumamoto University, 2-2-1 Honjo, Kumamoto 860-0811, Japan

[4]The Institute of Medical Science, The University of Tokyo, 4-6-1 Shirokanedai, Minato-ku, Tokyo 108-8639, Japan

*Correspondence:

Hiroyuki Yamamoto, AIDS Research Center, National Institute of Infectious Diseases, 4-7-1 Gakuen, Musashi-Murayama City, Tokyo 208-0011, Japan. Phone: +81-42-848-7154; Fax: +81-42-848-7155. Email: h-yamato@niid.go.jp

Tetsuro Matano, National Institute of Infectious Diseases, 1-23-1 Toyama, Shinjuku-ku, Tokyo 162-8640, Japan. Phone: +81-3-4582-2811; Fax: +81-3-5285-1165. Email: tmatano@niid.go.jp

Running title: SIV neutralization post-PI3K diminution

Abstract

HIV and simian immunodeficiency virus (SIV) infections are known for impaired neutralizing antibody (NAb) responses. While sequential virus-host B cell interaction appears to be basally required for NAb induction, driver molecular signatures predisposing to NAb induction still remain largely unknown. Here we describe SIV-specific NAb induction following a virus-host interplay decreasing aberrant viral drive of phosphoinositide 3-kinase (PI3K). Screening of seventy difficult-to-neutralize SIV_{mac239}-infected macaques found nine NAb-inducing animals, with seven selecting for a specific $CD8^+$ T-cell escape mutation in viral *nef* before NAb induction. This Nef-G63E mutation reduced excess Nef interaction-mediated drive of B-cell maturation-limiting PI3K/mammalian target of rapamycin complex 2 (mTORC2). *In vivo* imaging cytometry depicted preferential Nef perturbation of cognate Envelope-specific B cells, suggestive of polarized contact-dependent Nef transfer and corroborating cognate B-cell maturation post-mutant selection up to NAb induction. Results collectively exemplify a NAb induction pattern extrinsically reciprocal to human PI3K gain-of-function antibody-dysregulating disease, and indicate that harnessing the PI3K/mTORC2 axis may facilitate NAb induction against difficult-to-neutralize viruses including HIV/SIV.

Keywords

neutralizing antibody; B cells; $CD8^+$ T cells; PI3 kinase; inborn errors of immunity; HIV/SIV

45 **Introduction**

46

47 Virus-specific neutralizing antibody (NAb) responses by B cells are induced by a tight
48 cooperation of adaptive immune cells (Kumar et al., 2010; Shulman et al., 2014; Giltin et al.,
49 2014; Wang et al., 2014) and often play a central role in clearance of acute viral infections
50 (Junt et al., 2007). In contrast, persistence-prone viruses such as human immunodeficiency
51 virus type 1 (HIV-1), simian immunodeficiency virus (SIV) and lymphocytic choriomeningitis
52 virus (LCMV) variously equip themselves with B cell/antibody-inhibitory countermeasures
53 (Moir et al., 2001; Mattapallil et al., 2005; Sommerstein et al., 2015; Sammicheli et al., 2016;
54 Fallet et al., 2016; Mason et al., 2016) and NAb responses are impaired (Levesque et al.,2009;
55 Mikell et al., 2011). These viruses successfully suppress elicitation of potent NAb responses
56 particularly in acute infection (Hunziker et al., 2003; Tomaras et al., 2008) and establish viral
57 persistence, posing considerable challenge for developing protective strategies. Particularly,
58 HIV and SIV establish early a large *in vivo* body of infection with a distinct host genome-
59 integrating retroviral life cycle (Whitney et al., 2014). In addition, lentiviruses HIV/SIV are
60 unique in launching a matrix of host immune-perturbing interactions mainly by their six
61 remarkably pleiotropic accessory viral proteins optimally fueling pathogenesis (Kirchhoff et al.,
62 1995; Sheehy et al., 2002; Harris et al., 2003; Schindler et al., 2006; Neil et al., 2008; Zhang
63 et al., 2009; Laguette et al., 2011; Yamada et al., 2018; Joas et al., 2018; Langer et al., 2019;
64 Yan et al., 2019; Joas et al., 2020; Khan et al., 2020; Volcic et al., 2020; Reuschl et al., 2022).
65 A body of evidence has depicted this over these 30 years, whereas its entity, including focal
66 mechanisms of humoral immune perturbation in HIV/SIV infection, still remains elusive.

67 Contrasting this detrimental consequence of acute-phase endogenous NAb absence
68 driven by adverse virus-host interactions in early HIV/SIV infection, we and others have
69 previously described in *in vivo* experimental models that acute-phase passive NAb infusion
70 can trigger an endogenous T-cell synergism resulting in robust SIV/SHIV (simian/human
71 immunodeficiency virus) replication control (Haigwood et al., 1996; Yamamoto et al., 2007; Ng
72 et al., 2010; Iseda et al., 2016; Nishimura et al., 2017). This shows that virus-specific NAbs

73 not only confer sterile protection but also can evoke T-cell-mediated non-sterile viral control,
74 suggesting the importance of inducing endogenous NAb responses during an optimal time
75 frame as well as humoral-cellular response synergisms. Therefore, identifying mechanisms
76 driving NAb induction against such viruses is an important step to eventually design NAb-
77 based HIV control strategies.

78 As an approach, analysis of *in vivo* immunological events linked with NAb induction
79 against difficult-to-neutralize SIVs in a non-human primate model can provide important
80 insights into this goal. Various *in vivo* signatures of HIV-specific NAb induction, such as
81 antibody-NAb coevolution (Moore et al., 2012), autoimmune-driven induction (Moody et al.,
82 2016) and natural killer cell-related host polymorphisms (Bradley et al., 2018) have been
83 reported to date. The variety collectively, and interestingly, indicates that pathways to NAb
84 induction against difficult-to-neutralize viruses including HIV/SIV are redundant, conversely
85 implicating as-yet-unknown mechanisms driving NAb induction. For example, the
86 neutralization resistance of certain SIV strains apparently is not explanatory by any of the
87 aforementioned, posing such models as attractive analytic targets of NAb induction
88 mechanisms.

89 In the present study, we examined virus-specific antibody responses in rhesus
90 macaques infected with a highly difficult-to-neutralize SIV strain, SIV_{mac239}. This virus is
91 pathogenic in rhesus macaques causing simian AIDS across a broad range of geographical
92 origin of macaques (Cumont et al., 2008), shows persistent viremia and hosts lack NAb
93 responses throughout infection (Kestler et al., 1991; Nomura et al., 2012). Yet, upon
94 performing a large-scale screening of SIV_{mac239}-infected Burmese rhesus macaques for up to
95 100 weeks, we noticed a subgroup inducing NAbs in the chronic phase. Interestingly, these
96 animals commonly selected for a specific $CD8^+$ cytotoxic T lymphocyte (CTL) escape mutation
97 in the viral Nef-coding gene before NAb induction. The mutant Nef, compared with wild-type
98 (WT) Nef, manifested a decrease in aberrant interaction with phosphoinositide 3-kinase
99 (PI3K)/mammalian target of rapamycin complex 2 (mTORC2), resulting in decreased
100 downstream hyperactivation of the canonical B-cell negative regulator Akt (Omori et al., 2006;

101 Limon et al., 2014). Nef was graphically identified via machine learning-assisted imaging
102 cytometry to preferentially target Env-specific B cells *in vivo*, and in those macaques inducing
103 NAbs, the NAb induction was linked with sustained Env-specific B-cell responses after or
104 during the mutant Nef selection. Results describe a B-cell functional boosting phenotypically
105 reciprocal to a recently found human PI3K gain-of-function and antibody-dysregulating inborn
106 error of immunity (IEI), activated PI3 kinase delta syndrome (APDS) (Angulo et al., 2013;
107 Lucas et al., 2014), and suggest that intervening PI3K/mTORC2 signaling can potentially
108 result in harnessing NAb induction against difficult-to-neutralize viruses.

109 **Results**

110

111 **Identification of macaques inducing SIV_{mac239}-neutralizing antibodies**

112 We performed a retrospective antibody profile screening in rhesus macaques infected
113 with NAb-resistant SIV_{mac239} (*n* = 70) (**Figure 1A**) and identified a group of animals inducing
114 anti-SIV_{mac239} NAb responses (*n* = 9), which were subjected to characterization. These NAb
115 inducers showed persistent viremia with no significant difference in viral loads compared with
116 a profile-clarified naïve, major histocompatibility complex class I (MHC-I) haplotype-balanced
117 subgroup of NAb non-inducers (*n* = 19) representatively utilized for comparison hereafter
118 (**Figure 1B** and **Figure 1-figure supplement 1**). Plasma SIV_{mac239}-NAb titers measured by 10
119 $TCID_{50}$ SIV_{mac239} virus-killing assay showed an average maximum titer of 1:16, being induced
120 at an average of 48 weeks post-infection (p.i.) (**Figure 1C**). Two of the nine NAb inducers
121 showed detectable NAb responses before six months p.i., while the remaining seven induced
122 NAbs after six months. Anti-SIV_{mac239} neutralizing activity was confirmed in immunoglobulin G
123 (IgG) purified from plasma of these NAb inducers (**Figure 1-figure supplement 2**). SIV Env-
124 binding IgGs developed from early infection in NAb inducers as well as non-rapid-progressing
125 NAb non-inducers, the latter differing from rapid progressors known to manifest serological
126 failure (Hirsch et al., 2004; Nakane et al., 2013) (**Figure 1-figure supplement 3A**); titers were
127 not higher but rather lower at year 1 p.i. in the NAb inducers (**Figure 1-figure supplement 3B**
128 and **3C**). This was consistent with other reports (Havenar-Daughton et al., 2016) and differing
129 with gross B-cell enhancement in Nef-deleted SIV infection with enhanced anti-SIV binding
130 antibody titers accompanying marginal neutralization (Adnan et al., 2016). NAb inducers and
131 non-inducers showed similar patterns of variations in viral *env* sequences (Burns et al., 1993),
132 mainly in variable regions 1, 2 and 4 (V1, V2 and V4) (**Figure 1-figure supplement 4**).

133

134 **Selection of a viral *nef* mutation (Nef-G63E) precedes chronic-phase SIV_{mac239}-specific**
135 **NAb induction**

136 Viral nonsynonymous polymorphisms outside *env* were next assessed. Strikingly, we

137 found selection of a viral genome mutation resulting in G (glycine)-to-E (glutamic acid)
138 substitution at residue 63 of Nef (Nef-G63E) in seven of the nine NAb inducers (**Figure 2A**).
139 This 63rd residue lies in the unstructured N-terminus of Nef, flanked by two α-helices
140 conserved in SIVmac/SIVsmm (**Figure 2B**). This region is generally polymorphic among HIV-
141 1/HIV-2/SIV, occasionally being deleted in laboratory and primary isolate HIV-1 strains (Geyer
142 et al., 2001). AlphaFold2-based structure prediction did not derive palpable change except for
143 low-probability disruption of the alpha helices (data not shown). The Nef G63E mutation was
144 not observed in two early NAb inducers (with detectable NAbs before 6 months p.i.) but
145 selected in all of the remaining seven inducing detectable NAb responses after 6 months. In
146 contrast, this mutation was found only in two of the nineteen NAb non-inducers, including one
147 rapid progressor (**Figure 1-figure supplement 1**) and selection was significantly enriched in
148 the NAb inducers as compared to the nineteen non-inducers (**Figure 2C**). Analysis of Nef-
149 G63E mutation frequencies in plasma viruses showed that Nef-G63E selection preceded or
150 at least paralleled NAb induction (**Figure 2D**).
151
152 **Nef-G63E is a CD8$^+$ T-cell escape mutation**
153 These seven NAb inducers selecting this mutation elicited CD8$^+$ T-cell responses
154 specific for a 9-mer peptide Nef$_{62–70}$ QW9 (QGQYMNTPW) (**Figure 3A**). This Nef$_{62–70}$ QW9
155 epitope is restricted by MHC-I molecules Mamu-B*004:01 and Mamu-B*039:01 (Evans et al.,
156 1999; Sette et al., 2012). Possession of these accounted for six cases of Nef-G63E selection
157 (**Figure 3A**), and the remaining one animal possessed Mamu-A1*032:02 predicted to bind to
158 Nef$_{63–70}$ GW8 (NetMHCpan). Ten of nineteen NAb non-inducers also had either of these alleles
159 (**Figure 1-figure supplement 1**). This did not significantly differ with the NAb inducer group
160 (P = 0.25 by Fisher's exact test, data not shown), indicating that NAb induction was not simply
161 linked with possession of these MHC-I genotypes but instead required furthermore specific
162 selection of the Nef-G63E mutation (**Figure 2C**). Nef-G63E was confirmed to be an escape
163 mutation from Nef$_{62-70}$-specific CD8$^+$ T-cell responses (**Figure 3B**). NAb non-inducers
164 possessing these alleles elicited little or no Nef$_{62-70}$-specific CD8$^+$ T-cell responses (**Figure 3-**

165 **figure supplement 1A**), suggesting that *in vivo* selection and fixation of this Nef-G63E SIV
166 was indeed Nef_{62-70}-specific $CD8^+$ T cell-dependent. Replication kinetics of SIV carrying the
167 Nef-G63E mutation was comparable with wild-type (WT) on a cynomolgus macaque HSC-F
168 $CD4^+$ T-cell line (Akari et al., 1996), excluding the possibility that the mutation critically impairs
169 viral replication (**Figure 3-figure supplement 1B**), and plasma viral loads were comparable
170 between Nef-G63E mutant-selecting NAb inducers versus non-inducers (**Figure 3-figure**
171 **supplement 1C**). These results indicate NAb induction following *in vivo* selection and fixation
172 of the $CD8^+$ T-cell escape *nef* mutation, Nef-G63E under viral persistence.
173
174 **G63E mutation reduces aberrant Nef interaction-mediated drive of PI3K/mTORC2**
175 We next focused on the functional phenotype of this highlighted Nef-G63E mutant SIV
176 in infected cells. An essence of host perturbation by Nef is its wide-spectrum molecular
177 downregulation, ultimately increasing viral replication (Schindler et al., 2004; Zhang et al.,
178 2009). To address possible amelioration, we compared downregulation of major targets CD3,
179 CD4, MHC-I, CXCR4 and BST-2 (Jia et al., 2009) in infected HSC-F cells. Nef-G63E mutation
180 did not confer notable change compared with wild-type (WT) [*P* = not significant (*n.s.*) for all
181 molecules, data not shown], implicating other non-canonical changes (**Figure 4A**). Literature
182 suggested ferritin to exert negative influence on B cells proportionate to HIV-infected
183 macrophage-derived production (Swingler et al., 2008). Here, plasma ferritin levels showed
184 no differences (**Figure 4-figure supplement 1A**) and viral loads were comparable between
185 Nef-G63E-selecting NAb inducers and non-inducers (**Figure 4-figure supplement 1B** and
186 **1C**), arguing against gross involvement of ferritin as well as other viral replication-changing
187 Nef phenotypes at least in this model.
188 Thus, we took interest in immunosignaling-modulating properties of Nef-G63E SIV.
189 Analysis of Akt, the predominant immune-intrinsic negative brake of B-cell maturation and
190 AFC/antibody responses *in vivo* (Omori et al., 2006; Limon et al., 2014; Fruman et al., 1999;
191 Ray et al., 2015; Sander et al., 2015), revealed that its serine 473 phosphorylation, non-
192 canonically known for Nef-mediated upregulation (Kumar et al., 2016), was significantly lower

193 on day 3 after Nef-G63E SIV infection at low multiplicity of infection (MOI) compared with WT
194 (**Figure 4B**), stronger than histogram deviation levels in PI3K gain-of-function mice with full
195 recapitulation of B-cell/antibody-dysregulating human APDS disease phenotype (Avery et al.,
196 2018). The threonine 308-phosphorylated Akt (pAkt Thr308) level remained unaffected
197 (**Figure 4-figure supplement 1B**).

198 We further assessed properties of serine 473-phoyphorylated Akt (pAkt Ser473)
199 inhibition by Nef-G63E SIV, and found that external PI3K stimuli (serum starvation) (Kennedy
200 et al., 1997) accelerated phenotype appearance from day 3 to day 1 post-infection (**Figure**
201 **4C**, left). A similar trend was obtained by short-term PI3K stimulation with interferon-γ (Nguyen
202 et al., 2001), interleukin-2 (Marzec et al., 2008) and SIV Env (François & Klotman, 2003)
203 (**Figure 4-figure supplement 1C**). A high-MOI SIV infection, comprising higher initial
204 concentration of extracellular Env stimuli, also accelerated phenotype appearance from day 3
205 to day 1 post-infection, with stronger pAkt reduction (**Figure 4C**, right). These showed that the
206 Akt-inhibitory G63E mutant Nef phenotype is PI3K stimuli-dependent. Transcriptome analysis
207 signatured decrease in PI3K-pAkt-FoxO1-related genes in mutant SIV infection (**Figure 4-**
208 **figure supplement 1D**). As Akt is also a survival mediator this implicated that Nef-G63E
209 mutation may be Th-cytopathic, decreasing Th dysfunctional expansion (Baumjohann et al.,
210 2013) as had been observed in LCMV strain WE (Recher et al., 2004) and chronic HIV/SIV
211 (Gray et al., 2011; Lindqvist et al., 2012; Petrovas et al., 2012) infections. Here, reduced
212 chronic-phase peripheral $CXCR3^{-}CXCR5^{+}PD\text{-}1^{+}$ memory follicular Th (Tfh), linked with
213 antibody cross-reactivity in one cohort (Locci et al., 2013), was somewhat in line with this
214 notion (**Figure 4-figure supplement 1E** and **1F**). We additionally examined another CTL
215 escape mutant Nef-G63R, selected with marginal statistical significance primarily in early
216 stage (**Figure 4-figure supplement 2A**). This mutant did not associate with NAb induction in
217 one control animal (R06-034) even upon preferential selection (**Figure 4-figure supplement**
218 **2B**) and Nef-G63R mutant was not similarly decreased in pAkt drive (**Figure 4-figure**
219 **supplement 2C**), implicating that the Nef-G63E mutation was more tightly linked with NAb
220 induction in terms of an immunosignaling phenotype.

221 We further explored molecular traits of this decreased Akt hyperactivation. We reasoned
222 that comparing endogenous Nef binding patterns would be adequate and analyzed SIV-
223 infected HSC-F cells with a flow cytometry-based proximity ligation assay (PLA) (Leuchowius
224 et al., 2009; Avin et al., 2017), by calculating a mean fluorescence intensity (MFI) deviation-
225 based binding index for each. We found that this Nef-G63E mutation causes significant
226 decrease in Nef binding to PI3K p85/p110α and downstream mTORC2 components mTOR
227 (Sarbassov et al., 2005) and GβL/mLST8 (Kim et al., 2003) in the $CD4^{lo}$-SIV Gag $p27^{+}$ infected
228 population (**Figure 4D**). Results were biochemically confirmed by a decrease in G63E-
229 mutated Nef binding to the mTORC2-intrinsic cofactor Sin1 in coimmunoprecipitation analysis
230 of infected HSC-F cells (**Figure 4E**). Collectively, the Nef-G63E mutation results in decreased
231 aberrant Nef bridging and signal transduction of PI3K/mTORC2, explaining decreased
232 substrate Akt Ser473 phosphorylation by mTORC2. These properties were in keeping with an
233 acceleration in CD4-downregulated/infected HSC-F cell apoptosis upon Nef-G63E SIV
234 infection (**Figure 4F**). Thus, Nef-G63E SIV is a mutant virus decreased in aberrant
235 interaction/drive of B-cell-inhibitory PI3K/mTORC2 signaling, manifesting a molecular
236 signature reciprocal to human APDS (Angulo et al., 2013; Lucas et al., 2014; Avery et al.,
237 2018).
238
239 **Targeting of lymph node Env-specific B cells by Nef *in vivo***
240 Next, we analyzed *in vivo* targeting of virus-specific B cells by Nef in lymph nodes to
241 explore the potential B-cell-intrinsic influence of the G63E-Nef phenotype. Previously
242 suggested influence of soluble Nef itself (Qiao et al., 2006) and/or related host factors
243 (Swingler et al., 2008) may derive generalized influence on B cells; however, SIV antigen-
244 specific binding antibody responses were rather decreased in NAb inducers (**Figure 1-figure**
245 **supplement 1**), viremia was comparable (**Figure 3-figure supplement 1C**) and ferritin levels
246 were not altered (**Figure 4-figure supplement 1A**), differing from the aforementioned
247 literature stating positive correlation between the three. Therefore, we surmised that some
248 targeted Nef intrusion against Env-specific B cells may be occurring and that the decreased

249 aberrant Nef-PI3K/mTORC2 drive may result in their enhanced lymph node maturation.

250 While reports (Xu et al., 2009) histologically proposed Nef B-cell transfer, quantitative
251 traits, e.g., invasion frequency and influence on virus-specific B cells, have remained unvisited.
252 Intracellular Nef staining is dim (particularly for B cell-acquired Nef), difficult to examine by
253 conventional flow cytometry. Defining staining cutline requires single-cell images, overcoming
254 confounding of high Nef false-staining via pre-permeation rupture and post-permeation
255 confounding as judged by biologically discontinuous staining and/or batch-inflated signals.
256 Collectively, at the expense of spatial information, we judged that sophisticating imaging
257 cytometry would best visualize Nef-mediated B-cell perturbation *in vivo*. We analyzed lymph
258 node B cells with Image Stream X MKII, with high-power (> 10-fold) antigen detection [e.g.,
259 molecules of equivalent soluble fluorochrome (MESF) 5 *vs.* MESF 80 in an average flow
260 cytometer for FITC detection] ideal for detection/single-cell verification.

261 We designed a triple noise cancellation strategy to overcome the above. Firstly, amine
262 reactive dye staining (Perfetto et al., 2006) gated out B cells being Nef-positive due to pre-
263 experimental membrane damage (**Figure 5-figure supplement 1A**, left). Next, we deployed
264 secondary quantitative parameters of Nef signals deriving from each pixel of the images.
265 Definition of a gray-level cooccurrence matrix (GLCM) (Haralick et al., 1973) numerating
266 adjacent signal deviation as their frequencies on a transpose matrix enables calculation of a
267 variety of feature values summarizing traits of the whole image. A biological assumption of Nef
268 signal continuity in a true staining suggested that the sum of weighted square variance of
269 GLCM, i.e., the {sum of [square of (value – average signal strength) × frequency of each value
270 occurrence]} would separate natural versus artificial Nef signals. This value, Haralick variance,
271 was computed for multiple directions and averaged, deriving Haralick variance mean (**Figure
272 5-figure supplement 1A**, X axis), proportionate with staining image unnaturalness. Finally,
273 Nef signal intensity threshold (**Figure 5-figure supplement 1A**, Y axis) gated out overtly-
274 stained cells void for true-false verification. These excluded B cells showing non-specific,
275 strong-signal binary-clustered staining pixels for Nef deriving a large summated variance (X
276 axis), and/or cells batch-stained for Nef (Y axis), likely originating from post-experimental

277 membrane damage.

278 With this approach we acquired images of a Live/Dead^{-}-Nef signal Haralick variance
279 mean^{lo}-Nef signal intensity threshold^{lo}-Nef^{+}CD19^{+} B-cells, with fine-textured gradation of Nef^{int-}
280 ^{lo} staining with continuity from membrane-proximal regions without sporadic staining speckles
281 (**Figure 5A** and **Figure 5-figure supplement 1**). A linear discriminant analysis-based machine
282 learning module, scoring segregation of typical void/valid images, showed this gating to
283 provide the highest two-dimensional separation (**Figure 5-figure supplement 1**). Combined
284 with biotinylated Env/streptavidin staining, this reproducibly obtained images of Env-specific
285 (Ch 12) CD19^{+} (Ch 11) B cells without membrane ruptures (Ch 08) and showing fine-textured
286 transferred Nef (Ch 02) (**Figure 5B**). Nef invasion upregulated pAkt Ser473 (Ch 03) to a range
287 resembling *in vitro* analysis (**Figure 5C**), stating that Nef-driven aberrant PI3K/mTORC2
288 signaling does occur in Nef-invaded B cells *in vivo* and the current phenotypic change likely
289 affects B-cell dynamics. Strikingly, lymph node Env-specific B cells showed significantly higher
290 Nef-positive frequencies as compared with batch non-Env-specific B cells (**Figure 5D**). This
291 indicated that infected cell-generated Nef preferentially targets adjacent Env-specific B cells,
292 putatively through infected CD4^{+} cell-to-B-cell contact/transfer (Xu et al., 2009; Hashimoto et
293 al., 2016) and that a Nef phenotypic change likely dictates Env-specific B-cell maturation.
294

295 **Cell contact-dependent B-cell invasion from infected cells *in vitro***

296 To understand cell-intrinsic properties enhancing B-cell Nef acquisition *in vivo*, we
297 addressed in an *in vitro* coculture reconstitution how infected cell-to-B-cell Nef invasion may
298 take place or be modulated. We performed imaging cytometry on a twelve-hour coculture of
299 SIV-disseminating HSC-F cells (reaching around 30% Nef-positivity at moment of coculture)
300 with Ramos B cells (**Figure 6A**, top left), independent of MHC-related interactions known to
301 enhance T-cell/B-cell contact (Wülfing et al., 1998). Machine learning-verified noise
302 cancellation of fragmented signal acquisition (**Figure 6A**, middle left) filtered reproducible
303 images of Nef-positive HSC-F cells directly adhering to Ramos B cells within the doublet
304 population (**Figure 6A**, top to middle right). Importantly, addition of a soluble macaque CD3

305 stimulation-competent antibody resulted in enhanced Nef$^+$ T-cell adhesion to B cells (**Figure**
306 **6A**, bottom center), accompanying images of polarized Nef protrusion/injection from T cells to
307 B cells (second column, filled wedges) as well as trogocytosed B-cell membranes (third
308 column, open wedge), in keeping with dynamic B-cell Nef acquisition. Centrifugation strengths
309 upon cell collection and staining (190 x *g* versus 1,200 x *g* and 600 x *g* versus 1,200 x *g*,
310 respectively) shifted the tendency between enriched Nef$^+$ HSC-F-B-cell doublet versus Nef$^+$
311 B-cell singlet detection via CD3 stimulation, respectively (**Figure 6A**, lower right).
312 Substantiated by the acquired images, an enhancement of live singlet Ramos B-cell Nef
313 acquisition (Nef$^+$ frequencies/total) was also observed by CD3 stimulation in conventional flow
314 cytometry (**Figure 6B**). We observed a similar enhancement by phytohemagglutinin (PHA)
315 stimulation whereas phorbol-12-myristate-13-acetate (PMA)/ionomycin did not enhance B-cell
316 Nef acquisition. In a similar 72-hour static infected cell coculture with primary CD20$^+$ B cells,
317 we detected recapitulation of the decreased B-cell pAkt Ser473 phosphorylation upon G63E
318 Nef transfer compared to that of WT Nef (**Figure 6C**), implicating that the Nef-G63E mutation
319 can directly alleviate maturation inhibition in preferentially Nef-targeted Env-specific B cells.
320

321 **Enhanced Env-specific B-cell responses after PI3K-diminuting mutant selection**

322 Finally, peripheral SIV Env-specific IgG$^+$ B-cell responses comprising plasmablasts
323 (PBs) and memory B cells (B_{mem}) were analyzed to assess *in vivo* B-cell quality in NAb
324 inducers with Nef-G63E mutant selection. After excluding lineage-specific cells [T/NK/pro-B
325 cells/monocytes/myeloid dendritic cells (DCs)/plasmacytoid DCs], we defined IgG$^+$ PBs as
326 showing: high replication (Ki-67$^+$), post-activation (HLA-DR$^+$), transcriptional switching for
327 terminal differentiation (IRF4^{hi}) and downregulated antigen surface binding (surface [s]Env^{lo}-
328 cytoplasmic [Cy]Env$^+$) (Nutt et al., 2015; Silveira et al, 2015). Env-specific PBs were defined
329 as CD3$^-$CD8$^-$CD10$^-$CD14$^-$CD16$^-$CD11c$^-$CD123$^-$CD19$^-$CyIgG$^+$Ki-67$^+$IRF4^{hi}HLA-DR$^+$ (total PB)
330 sEnv^{lo}CyEnv$^+$ (Env-specific) (**Figure 7A** and **Figure 7-figure supplement 1**). NAb inducers
331 showed significantly higher Env-specific IgG$^+$ PB responses around week 30 p.i., after Nef-
332 G63E selection, compared to those in NAb non-inducers (**Figures 7B** and **7C**). At 1 year, this

333 difference became enhanced; Env-specific PB frequencies were reduced in non-inducers,
334 while this reduction was ameliorated in the NAb inducers with Nef-G63E.

335 Concomitant determination of Env-specific $IgD^{-}CD27^{+}IgG^{+}$ B_{mem} responses allowed pair-
336 wise analysis of Env-specific IgG^{+} B_{mem}/PB as a projection of germinal center (GC) output as
337 an indicator of overall B-cell response quality (Zotos et al., 2010) (**Figure 7D**, left). In this two-
338 dimensional vector charting of Env-specific B_{mem}/PB responses, vector protrusion towards
339 upper right reasonably represents higher gross GC output of antibody-forming cells (AFCs)
340 (B_{mem}/PBs). In NAb non-inducers, all vectors converged on an empirically defined polygonal
341 attractor area D_n (gray area surrounded with dotted lines in **Figure 7D**, right) at year 1 p.i. and
342 beyond, describing that these NAb non-inducers failed to sustain Env-specific GC output. In
343 contrast, the vectors were consistently tracked outside D_n in the NAb inducers with Nef G63E
344 (**Figure 7D**). At the moment of NAb induction, they converged on another upper-right GC
345 output attractor area D_i (red area surrounded with dotted lines in **Figure 7D**, right), mutually
346 exclusive with D_n ($P < 0.0001$ by Fisher's exact test on NAb non-inducer/inducer vector
347 distribution frequency within D_n). These suggest more robust virus-specific IgG^{+} B-cell
348 responses following Nef-G63E $CD8^{+}$ T-cell escape mutant selection, predisposing to NAb
349 induction. This enhanced cognate B-cell signature was also an inverted pattern of impaired
350 terminally-differentiated B-cell responses in APDS (Al Qureshah et al., 2021).

351 Taken together, in the current model, Nef_{62-70}-specific $CD8^{+}$ T-cell responses in
352 persistently SIV_{mac239}-infected macaques selected for an escape mutant, Nef-G63E SIV, which
353 decreased aberrant Nef binding and drive of B-cell-inhibitory PI3K/mTORC2. B-cell Nef
354 invasion *in vivo* occurred more preferentially in Env-specific B cells, suggesting diminution in
355 tonic Nef-mediated B-cell dysregulation after mutant selection. These predisposed to
356 enhanced Env-specific B-cell responses and subsequent SIV_{mac239}-specific NAb induction,
357 altogether, in a manner reciprocal to human APDS-mediated immune dysregulation.

358 **Discussion**

359

360 In the present study, we found NAb induction against an NAb-resistant SIV after
361 selection of a $CD8^+$ T-cell escape *nef* mutant virus. The Nef-G63E mutation, positioned in
362 cognate B cells, results in reduction of binding/drive of PI3K/mTORC2, being concordant with
363 *in vivo* enhancement of Env-specific IgG^+ B cells up to NAb induction following mutant
364 selection. Importantly, this manifested through a pAkt deviation level more vivid than wild-type
365 versus germline *PIK3CD* gain-of-function mutation heterozygote mice recapitulating full
366 human APDS phenotype (Avery et al., 2018). Thus, the current Nef-G63E-associated B-
367 cell/NAb phenotype likely occurs in a "reciprocal APDS-like" manner. This proposition was
368 enhanced based on extension of immune cell-intrinsic Nef influence on cognate B cells (Fig.
369 5), in addition to infected T cells. This work is, to our knowledge, the first to interlink a
370 PI3K/mTORC2-modulating viral signature and enhanced B-cell/NAb responses in a viral
371 infection model.

372 A link between viral T-cell escape and consequent immune modulation has been
373 previously partially explored, including enhanced mutant HIV-1 epitope peptide binding to
374 inhibitory MHC-I receptor on DCs impairing T cells (Lichterfeld et al., 2007) and decreased
375 CTL-mediated lymph node immunopathology rather driving LCMV-specific antibody
376 production (Battegay et al., 1993). Our results now evidence a new pattern of NAb responses
377 bivalently shaped through viral interactions with both humoral and cellular immunity in AIDS
378 virus infection. SIV_{mac239} infection of macaques possessing MHC-I alleles associated with Nef-
379 G63E mutation can be one unique model to analyze virus-host interaction for B cell maturation
380 leading to NAb induction. The time frame of Nef-G63E mutant selection versus moment of
381 NAb induction was variable in the inducers, for which we did not obtain a clear explanation.
382 This may be influenced by certain basal competitive balance between humoral versus cellular
383 adaptive immunity, as observed in certain vaccination settings (Querec et al., 2009).

384 Identification of the current Nef-G63E candidate phenotype adds one aspect to the
385 wealth of evidence documenting the multifaceted impact of Nef in HIV/SIV infection (Kirchhoff

386 et al., 1995; Gauduin et al., 2006; Stolp et al., 2012). It appeared unique that the current
387 phenotype differed from decreased replication-related properties or generalized amelioration
388 in immune impairment such as those documented in delta-Nef HIV/SIV infection (Kirchhoff et
389 al., 1995; Johnson et al., 1997; Gauduin et al., 2006; Fukazawa et al., 2012). The SIV Nef N-
390 terminal unstructured region comprising Nef-G63E is not conserved in HIV-1 (Schindler et al.,
391 2004) and beyond this model study it remains to be addressed whether a mutant HIV-1 with a
392 similar immunosignaling-affecting phenotype can be obtained and how much lentiviral
393 conservation exists for such interactions. Cognate B-cell maturation analysis on cohort basis
394 (Hau et al., 2022) may potentially assist this approach.

395 Obtained results on preferential Nef transfer to Env-specific B cells (**Figure 5**) implicate
396 involvement of polarized cognate immune cell perturbation *in vivo*, best depicted for
397 preferential infectivity of HIV-specific $CD4^+$ T cells (Douek et al., 2002) and HIV condensation
398 to the dendritic cell-T-cell interface (McDonald et al., 2003). As cognate MHC class II
399 interactions (Wülfing et al., 1998; Giltin et al., 2014) regularly occur between HIV/SIV-specific
400 $CD4^+$ T cells and Env-specific B cells in the germinal center, results may show that Env-
401 specific B-cell dysregulation stems from a negative consequence of exploited cognate T-
402 cell/B-cell orchestration. Enhanced T-cell attachment and transfer of Nef to B cells *in vitro* by
403 CD3 activation (**Figure 6**), mimicking peptide/MHC (pMHC) signaling, may facilitate recovery
404 from viral T-cell cytoskeletal impairment (Campbell et al., 2004; Jolly et al., 2004; Stolp et al.,
405 2009) antagonizing reduced motility (Stolp et al., 2012), resulting in *in vivo* “filtering” of
406 enhanced cognate $CD4^+$ T-cell interaction with cognate B cells. Combined with recent *in vivo*
407 detection of trogocytosed CD20-bearing follicular $CD4^+$ T cells positive for viral DNA and
408 showing increase during SIV infection (Samer et al., 2023), results suggest occurrence of
409 contact-dependent, polarized interactions facilitating Nef transfer to cognate B cells.

410 The major *in vivo* readout of this study is autologous neutralization of a highly difficult-
411 to-neutralize SIV, differing from HIV-specific broadly neutralizing antibodies (bNAbs).
412 Importantly, however, obtained signatures of enhanced IgG^+ Env-specific AFC B cells (class
413 switch/terminal differentiation) and virus neutralization (hypermutation) directly evidence

414 enhanced activity of activation-induced cytidine deaminase (AID), the canonical positive driver
415 of B-cell fate, showing a strong conceptual continuity with bNAb regulation by AID.

416 Our results extracted an *in vivo* link between a decreased aberrant Nef-PI3K/mTORC2
417 interaction and major enhancement in B-cell responses. The relationship is indeed reciprocal
418 to immunogenetic mechanisms of human PI3K gain-of-function mutations resulting in APDS
419 with multiply impaired anti-viral B-cell responses. APDS occurs from germline mutations in
420 leukocyte-intrinsic p110δ catalytic subunit-coding *PIK3CD* or the ubiquitous p85α regulatory
421 subunit-coding *PIK3R1*, both deriving class IA PI3K gain-of-function residue substitutions
422 (Dornan et al., 2017). Such mutations lead to immune cell-intrinsic perturbations with cognate
423 B-cell blockade, manifesting as impaired class-switched B-cell responses and susceptibility
424 against various infections (Angulo et al., 2013; Lucas et al., 2014; Coulter et al., 2017). In the
425 current work, we conversely document a decrease in virally induced tonic PI3K drive,
426 enhanced IgG class-switched cognate B-cell responses and NAb induction against a notably
427 difficult-to-neutralize SIV. While the exact hierarchy of binding between Nef and
428 PI3K/mTORC2 components (including PI3K isoforms) and its perturbation by Nef-G63E
429 mutation remains to be investigated, PI3Kp85 did reasonably show the strongest Nef-binding
430 index in PLA assay (**Figure 4D**) as Nef and PI3Kp85 possess SH3-binding PxxP and SH3
431 domains, respectively (Rickles et al., 1994). Binding decrease in canonical partner PI3Kp85
432 may domino-trigger decrease with others, resulting in quintuple PI3K/mTORC2 binding
433 decrease and fragile downstream Akt signaling. Such domino-triggering is also observed from
434 gain-of-function-mutated p85 to p110 evoking its activation (Dornan et al., 2017) similarly
435 highlighting the fine-tuned nature of the pathway.

436 A limitation of this study is the use of retrospective samples, posing constraints for
437 detecting exact temporal changes in tonic viral B-cell perturbation. Related with this, sampling
438 of lymph node cells in animals belonging to the subgroup of interest at the optimal moment
439 was unpredictable. Certain plasma and cellular samples were also unavailable in differing
440 experiments. While partially addressed in *in vitro* reconstitution, much remains to be
441 investigated for the observed polarity of Env-specific B-cell perturbation *in vivo*. Similarly,

442 influence of the Nef-G63E phenotype on CD4$^+$ T cells *in vivo* and its consequence on B-cell
443 modulation remains largely elusive, and in the current work we focused mainly on molecular
444 properties of the NAb-correlating Nef-G63E mutant strain. As HIV/SIV infection uniquely
445 shows a biphasic Tfh dysregulation of acute-phase destruction (Mattapallil et al., 2005;
446 Moukambi et al., 2015; Moukambi et al., 2019) followed by dysregulated chronic-phase hyper-
447 expansion (Lindqvist et al., 2012; Petrovas et al., 2012; Cubas et al., 2013; Xu et al., 2015), it
448 is of interest how the PI3K drive-ameliorated and proapoptotic mutant influenced this axis
449 post-*in vivo* selection, warranting further studies ahead. While influence on B cells appears to
450 be stronger by unexplained reasons (Asano et al., 2018), it is noteworthy that PI3K gain-of-
451 function also evokes basal dysregulation in peripheral CD4$^+$ T cells, locally recapitulating the
452 consequence of immunodeficiency virus replication and implicating importance of this
453 signaling axis in HIV/SIV infection. In any event, usage of specific animal models does help to
454 depict a temporal cascade of *in vivo* events leading to NAb induction, assisting human
455 immunology. As future extension of this study extracting the NAb-involved molecular axis,
456 manipulation/reconstitution experiments shall be designed.
457 In conclusion, we exemplify in a non-human primate AIDS model that NAb induction
458 against a highly resistant SIV occurs after selection of a CD8$^+$ T-cell escape variant reduced
459 in excess PI3K/mTORC2 drive. These results provide an understanding of how
460 immunodeficiency virus-specific NAb responses can be shaped by both wings of adaptive
461 immune pressure and depicts that immune cell-intrinsic PI3K/mTORC2 manipulation may be
462 pivotal for harnessing antiviral NAb responses. As human IEIs are increasingly becoming
463 discovered with various immune-perturbing phenotypes and inheritance patterns (Jauch et al.,
464 2023), search of other types of analogies between viral immune dysregulations and human
465 IEIs may lead to identification of novel targets to modulate and harness immune responses in
466 translational settings.
467

Acknowledgments

This work was supported by Japanese Initiative for Progress of Research on Infectious Diseases for Global Epidemic (J-PRIDE) (JP19fm0208017 to H.Y.), Japan Program for Infectious Diseases Research and Infrastructure (Interdisciplinary Cutting-edge Research) (JP22wm0325006 to H.Y.), Research Programs on HIV/AIDS, Emerging and Re-emerging Infectious Diseases, and Global Health Issues (JP20fk0410022 and JP24fk0410066 to H.Y.; JP18fk0410003, JP20fk0410011, JP20fk0108125, JP20jm0110012, JP21fk0410035, and JP21jk0210002 to T.M.) from Japan Agency for Medical Research and Development, the Ministry of Education, Culture, Sports, Science, and Technology in Japan ([JSPS] KAKENHI Grants 17H02185, 18K07157 and 24K21287 to H.Y.; 21H02745 to T.M.), the Takeda Science Foundation (to H.Y.), the Imai Memorial Trust for AIDS Research (to H.Y.), and the Mitsui-Sumitomo Insurance Welfare Foundation (to H.Y.). We thank Fumiko Ono, Koji Hanari, Katsuhiko Komatsuzaki, Akio Hiyaoka, Hiromi Ogawa, Keiko Oto, Hirofumi Akari, Yasuhiro Yasutomi, Hiromi Sakawaki, Tomoyuki Miura and Yoshio Koyanagi for animal experiment assistance; Hiroyuki Kogure, Sayuri Seki and Julia R. Hirsiger for imaging cytometry technical assistance; Masako Nishizawa, Trang Thi Thu Hau, Shigeyoshi Harada, Takushi Nomura, Akiko Takeda, Taku Nakane, Nami Iwamoto, Taeko K. Naruse, Akinori Kimura and Mark S. de Souza for their help. H.Y. thanks Jun Abe, Shoi Shi, Bettina Stolp, Jens V. Stein, Makoto Yamagishi and Yusuke Yanagi for conceptual discussions, and Mike Recher for collaborative support.

Author Contributions

H.Y. conceived/designed/performed study and wrote manuscript; T.M. provided animal cohort, co-edited manuscript and co-directed study.

CRediT taxonomy:

Conceptualization: HY

Methodology: HY

Validation: HY

Formal analysis: HY

Investigation: HY

Resources: HY, TM

Data curation: HY

Writing—original draft: HY

Writing—review & editing: HY, TM

Visualization: HY

Supervision: HY, TM

Project administration: HY

Funding acquisition: HY, TM

Declaration of Interests

The authors declare no competing interests.

513 **Figure Legends**

514

515 **Figure 1. NAb induction against NAb-resistant SIV_{mac239}.**

516 **(A)** Study design.

517 **(B)** Plasma viral loads (SIV *gag* RNA copies/ml plasma) in NAb non-inducers (left) and

518 inducers (right).

519 **(C)** Plasma SIV_{mac239} 100% neutralizing end point titers by 10 $TCID_{50}$ killing assay on MT4-R5

520 cells. Points on the dotted line show marginally NAb-positive results (< 1:2). In some animals,

521 titers were comparable with our reported results using MT4 cells.

522

523 **Figure 2. Selection of a viral *nef* mutation (Nef-G63E) before NAb induction.**

524 **(A)** Viral *nef* mutations in NAb inducers. A linear schema indicating Nef functional domains is

525 aligned above. Mutations at timepoints with NAb^- (indicated by white wedge; mostly before 6

526 months p.i.), $NAb^{+/-}$ (green wedge) and NAb^+) (purple wedge; mostly after 1 year) are shown

527 in individual animals. Black and dark gray represent dominant and subdominant mutations (or

528 deletion in R-360) by direct sequencing, respectively. Red and pink indicate dominant and

529 subdominant G63E detection, respectively.

530 **(B)** Schema of SIV_{mac239} Nef structure and Nef-G63E mutation orientation.

531 **(C)** Comparison of frequencies of macaques having Nef-G63E in plasma viruses between

532 NAb non-inducers and inducers. Compared by Fisher's exact test.

533 **(D)** Temporal relationship of Nef G63E frequencies in plasma virus and NAb induction. Black

534 boxes (left Y axis) show log_2 NAb titers; red triangles and blue diamonds (right Y axis) show

535 percentage of G63E and G63R mutations detected by subcloning (15 clones/point on average),

536 respectively.

537

538 **Figure 3. Nef-G63E is a $CD8^+$ T-cell escape mutation.**

539 **(A)** $Nef_{62–70}$ QW9-specific $CD8^+$ T-cell frequencies and related MHC-I alleles in seven NAb

540 inducers selecting Nef-G63E. Mamu-B*039:01 and Mamu-B*004:01 are known to restrict

541 $Nef_{62–70}$ QW9 epitope and binding of $Nef_{63–70}$ peptide to Mamu-A1*032:02 was predicted.

542 **(B)** $CD8^+$ T-cell responses specific to wild-type $Nef_{62–70}$ or mutant $Nef_{62–70}$.G63E or $Nef_{62–}$

543 $_{70}$.G63R peptides.

544

545 **Figure 4. Nef-G63E mutation reduces PI3K/mTORC2 binding and pAkt drive.**

546 **(A)** Representative surface expression level histograms of CD3, CD4, MHC class I, CXCR4

547 and BST-2 in $CD4^{lo}Nef^+$ subpopulations after wild-type (WT) or Nef-G63E mutant SIV infection

548 at multiplicity of infection (MOI) 0.1 on HSC-F cells.

549 **(B)** Left: representative histograms of relative pAkt serine (Ser) 473 levels in $p27^+$

550 subpopulations after WT or Nef-G63E mutant SIV infection at MOI 0.1 on HSC-F cells.

551 Numbers show pAkt Ser473 mean fluorescence intensities (MFIs) for each. Right: Deviation

552 of pAkt Ser473 MFIs in $p27^+$ HSC-F cells compared with mean MFI of uninfected cells.

553 Compared by unpaired t test.

554 **(C)** Left: Relative pAkt Ser473 levels (normalized to mean MFI of uninfected controls) in Nef^+

555 HSC-F cells assessed for serum starvation (MOI 0.2, 1 day p.i.). Adjusted *P* values show

556 results of comparison via Sidak's post-hoc test of 2-way ANOVA (C, left). Right: Deviation of

557 pAkt Ser473 MFIs in Nef^+ HSC-F cells assessed for high-MOI infection (MOI 5, 1-day p.i.).

558 Compared by unpaired t test.

559 **(D)** Proximity ligation assay (PLA) of Nef binding with mTOR, GβL/mLST8, PI3Kp85 and

560 PI3Kp110α. MFI-based binding index was calculated as (anti-Nef/anti-partner) - (isotype/anti-

561 partner) - (anti-Nef/isotype) + (isotype/isotype). Histograms for samples and isotype/isotype

562 are representatively shown. Differences in MFI binding indexes can be enhanced compared

563 with comparison of raw MFIs. Compared by paired t tests.

564 **(E)** Sin1 co-immunoprecipitation analysis of WT versus Nef-G63E mutant SIV-infected HSC-

565 F cells (infected at MOI 0.05, day 3). Immunoblotting of Nef (37 kDa) in whole cell lysates

566 (lanes 4-6) and anti-Sin1 antibody immunoprecipitates (lanes 1-3) are shown.

567 **(F)** Cell death frequencies of SIV-infected cells measured by Annexin V positivity (% of $CD4^{lo}$)

568 (infected at MOI 0.1, day 3). Compared by unpaired t test.

569 Data represent one of two [(A); (B); (C, right)] independent experiments in quadruplicate, four
570 independent experiments performed in triplicate [(C, left)], four independent single-well
571 comparison experiments pooled for statistical analysis (D), two experiments (E) or two
572 experiments performed with six wells/control (F). Bars: mean ± SD (B, C right), mean ± SEM
573 (C left, F).
574
575 **Figure 5. Preferential targeting of lymph node Env-specific B cells by Nef *in vivo*.**
576 **(A)** Representative gating of triple noise-cancellation *in vivo* Nef staining in B cells analyzed
577 by ImageStreamX MKII. Pre-experimental damaged cells are first excluded with Live/Dead
578 from focused/centroid/singlet image-acquired $CD19^+$ B cells (first lane right/R4 gated on
579 "Focused"). Following Nef^+ gating (second lane left/R5 gated on R4), a second step of Nef
580 noise cancellation (second lane middle/R7 on R5) comprises double-negative removal of post-
581 experimental stochastic irregular staining building a disparate intracellular staining gradient (X
582 axis, Nef signal pixel Haralick variance mean) and post-experimental batch overt cellular
583 staining (Y axis, Nef signal pixel intensity threshold). This outputs a B-cell population with a
584 fine-textured pericellular $Nef^{int\text{-}lo}$ staining, biologically concordant with Nef membrane-
585 anchoring. Probing of anti-Env BCR (αEnv) by recombinant SIV Env (second lane, right) is
586 combined, resulting in a 2-D panel of intracellular Nef versus αEnv for noise-cancelled Nef^+ B
587 cells (R7) plus Nef^- B cells (R8) (third lane left/"R7+R8"). pAkt Ser473 expression (third lane
588 right) and cellular morphology (B) was further analyzed. DN, double-negative.
589 **(B)** Typical images of Nef-transferred Env-specific B cells defined αEnv^+-intracellular Nef^+-Nef
590 Haralick variance $mean^{lo}$-Nef Intensity $threshold^{lo}$-$Live/Dead^-$-$CD19^+$ cells ["Nef^+aEnv^+"
591 population of lower left panel in (A), gated on "R7, R8"]. Note the pericellular pAkt Ser473
592 upregulation in these cells (Ch 03/yellow). Data on inguinal lymph node lymphocytes of
593 macaque R10-007 at week 62 post-SIV_{mac239} infection are shown in (A) and (B).
594 **(C)** Comparison of pAkt Ser473 median fluorescence (medFI) intensity levels in Nef^- B cells
595 (R8) versus noise-cancelled Nef^+ B cells (R7). Analyzed by paired t test.
596 **(D)** Comparison of Nef-positive cell frequencies in non-Env-specific (left) versus Env-specific

597 (right) B cells in lymph nodes of persistently SIV-infected macaques (*n* = 6). Analyzed by paired
598 t test.
599
600 **Figure 6. Contact-dependent enhancement of B-cell Nef acquisition in reconstitution.**
601 **(A)** Imaging flow cytometric analyses of stimuli-dependent enhancement of infected HSC-F
602 cell adhesion to non-permissive $CD19^+$ Ramos B cells with the indicated gating (left).
603 Cocultured doublet cells subjected to machine learning-verified filtration of fragmented signal
604 acquisition (via gating Nef pixel signal $contrast^{lo}$-Nef mean pixel per $object^{hi}$ cells) deriving
605 typical images of infected HSC-F cell (Nef stain shown in pale blue pseudocolor) adhesion to
606 Ramos cells (CD19 stain shown in purple pseudocolor) are shown. Analyzed by unpaired t
607 test for doublet formation in the unstimulated versus anti-CD3 monoclonal antibody (clone FN-
608 18)-stimulated group.
609 **(B)** Flow cytometric analyses of Nef-acquiring live $CD19^+$ Ramos B cells upon coculture with
610 SIV-infected HSC-F cells with or without the indicated stimuli. Analyzed by one-way ANOVA
611 with Tukey's post-hoc multiple comparison tests.
612 **(C)** Representative flow cytometric plot (left), histogram (middle) and pAkt Ser473 signal
613 deviation in wild type versus G63E Nef-acquiring $CD20^+$ primary B cells (six wells/control).
614 Analyzed by unpaired t test. Data represent pooled data of two (A) or three [(B) and (C)]
615 independent experiments with indicated number of replicates showing similar results.
616
617 **Figure 7. Enhanced SIV Env-specific B-cell output up to NAb induction following Nef-**
618 **G63E selection.**
619 **(A)** Representative gating (R02-004, week 32 p.i.) of SIV Env gp140-specific memory B cells
620 (B_{mem}) and plasmablasts (PBs). Two panels for PB gating are shown in lower resolution for
621 visibility. B_{mem} staining was performed separately and gating are merged with PB panels
622 (second row, panels 2–4). For lineage-specific exclusion (first row, panel 4), CD10 was stained
623 independently for B_{mem} (see parenthesis).
624 **(B)** Changes in SIV Env gp140-specific plasmablast (PB) frequencies in viremic NAb non-

625 inducers (left, n = 12) and Nef-G63E-selecting NAb inducers (right, n = 6). Available samples
626 of twelve viremic NAb non-inducers (including ten with ≥ 1-year survival) and six NAb inducers
627 were tracked. In the right panel, the frequencies in NAb non-inducers are shown in background
628 (gray) for comparison.
629 **(C)** Comparison of Env gp140-specific PB frequencies between NAb non-inducers and
630 inducers by Mann Whitney U tests. In the right, the frequencies at NAb induction were
631 compared with those at year 1 in NAb non-inducers with ≥ 1-year survival (n = 10). Bars: mean
632 ± SD.
633 **(D)** Left: vector chart of Env gp140-specific memory B cell (B_{mem}) and PB levels. Legends for
634 each animal correspond to the ones in (B). Right: NAb non-inducer vectors empirically define
635 a polygonal GC output attractor area D_n (gray area surrounded with dotted lines) on which
636 they converge by and beyond year 1 p.i. The NAb inducer vectors (shown up to the time of
637 NAb induction) remained outside of D_n. At the moment of NAb induction they converged on a
638 second GC output attractor area D_i (red area surrounded with dotted lines), mutually exclusive
639 with D_n (P < 0.0001 by Fisher's exact test on NAb inducer vector convergence frequency within
640 D_n). Legends for year 1 p.i. in the NAb non-inducers and moment of NAb induction in the NAb
641 inducers are specified.

642 **Materials and Methods**

643

644 **Material availability**

645 This study did not generate new unique reagents.

646

647 **Data and code availability**

648 Data were analyzed using existing computational packages. The accession number for the
649 transcriptome data [wild-type SIV_{mac239}-infected HSC-F cell line (*n* = 3), Nef-G63E SIV_{mac239}-
650 infected HSC-F cell line (*n* = 3) and uninfected HSC-F cell line (*n* = 3)] has been deposited
651 under the accession number GenBank: GSE65806.

652

653 **Rhesus macaques retrospectively utilized for samples**

654 Seventy Burmese rhesus macaques (*macaca mulatta*) (57 males and 13 females) were
655 retrospectively analyzed in this study. Experiments were previously carried out (Matano et al.,
656 2004; Yamamoto et al., 2007; Iseda et al., 2016; Nomura et al., 2012; Ishii et al., 2012;
657 Takahashi et al., 2013; Nakane et al., 2013; Shi et al., 2013; Iwamoto et al., 2014; Terahara et
658 al., 2014) in the Tsukuba Primate Research Center, National Institutes of Biomedical
659 Innovation, Health and Nutrition (NIBIOHN) with the help of the Corporation for Production
660 and Research of Laboratory Primates and the Institute for Frontier Life and Medical Sciences,
661 Kyoto University (IFLMS-KU) after approval by the Committee on the Ethics of Animal
662 Experiments of NIBIOHN and IFLMS-KU under the guidelines for animal experiments at
663 NIBIOHN, IFLMS-KU and National Institute of Infectious Diseases in accordance with the
664 Guidelines for Proper Conduct of Animal Experiments established by Science Council of
665 Japan (http://www.scj.go.jp/ja/info/kohyo/pdf/kohyo-20-k16-2e.pdf). The experiments were in
666 accordance with the "Weatherall report for the use of non-human primates in research"
667 recommendations (https://royalsociety.org/topics-policy/publications/2006/weatherall-report/).
668 Animals were housed in adjoining individual primate cages allowing them to make sight and
669 sound contact with one another for social interactions, where the temperature was kept at

670 25°C with light for 12 hours per day. Animals were fed with apples and commercial monkey
671 diet (Type CMK-2, Clea Japan, Inc.). Blood collection and virus challenge were performed
672 under ketamine anesthesia.
673
674 **Cells and viruses**
675 MT4-R5 cells were maintained in RPMI1640 (Invitrogen) supplemented with 10% fetal bovine
676 serum (FBS) (Clontech) and antibiotics. HSC-F cells (cynomolgus $CD4^+$ T-cell line) and
677 HSR5.4 cells (rhesus macaque $CD4^+$ T-cell line) were maintained in RPMI1640 (Invitrogen)
678 supplemented with 10% fetal bovine serum (FBS) (Clontech), human interleukin-2 (IL-2) (10
679 IU/ml, Roche), 4-(2-hydroxyethyl)-1-piperazineethanesulfonic acid (HEPES) (Invitrogen) and
680 2-mercaptoethanol (Gibco). SIV_{mac239} molecular clone derivative was generated by
681 mutagenesis PCR (Agilent Technologies) using the primers listed. For virus preparation, COS-
682 1 cells were transfected with pBR_{mac239} proviral DNA using FuGENE 6 (Promega). At 48 h post-
683 transfection, culture supernatants were harvested, centrifuged and filtered through a 0.45-μm
684 pore-size filter (Merck Millipore). To titrate infectivity, prepared viruses were serially diluted and
685 infected on HSC-F cells in 96-well plates (Falcon) in quadruplicate. At 10 days post-infection,
686 the endpoint was determined using SIV p27 antigen enzyme-linked immunosorbent assay
687 (ELISA) kit (ABL), and virus infectivity was calculated as the 50 percent tissue culture infective
688 dose ($TCID_{50}$) according to the Reed-Muench method.
689
690 **Identification of SIV_{mac239}-NAb inducers**
691 Burmese rhesus macaques previously challenged with the highly pathogenic molecular clone
692 virus SIV_{mac239} (n = 70) were retrospectively examined approximately up to 2 years for their
693 plasma NAb profiles. Animals were challenged intravenously with 1,000 $TCID_{50}$ of SIV_{mac239}.
694 In the current study, virological and immunological profiles were compared between the newly
695 identified NAb inducers (n = 9) and representative NAb non-inducers (n = 19). Sex distribution
696 of the NAb inducers (eight males and one female) did not significantly differ with the total non-
697 inducers (49 males and 12 females, P = 0.99 by Fisher's exact test). These NAb non-inducers

698 and eight NAb inducers except R06-032 were previously partially reported for their plasma
699 viral loads (Yamamoto et al., 2007; Iseda et al., 2016; Nomura et al., 2012; Takahashi et al.,
700 2013; Nakane et al., 2013; Iwamoto et al., 2014) (**Figure 1B**). MHC-I haplotypes and alleles
701 were determined by reference strand-mediated conformation analysis, PCR-SSP (PCR
702 amplification utilizing sequence-specific priming) and cloning as described (Naruse et al.,
703 2010). MHC-I binding prediction was made on April 27, 2013 using the IEDB analysis resource
704 NetMHCpan tool (Hoof et al., 2009). Alleles of interest in the study have been previously
705 identified in macaques (Nomura et al., 2012; Evans et al., 1999; Sette et al., 2012). Macaques
706 R06-032, R03-015, R01-010 and R05-010 received a prime-boost vaccination (Matano et al.,
707 2004) composed of a DNA prime/intranasal Sendai virus vector expressing SIV_{mac239} Gag
708 (SeV-Gag). R03-015, R06-019, R06-038 and R10-001 received 300 mg of non-specific rhesus
709 IgG at day 7 post-SIV_{mac239} challenge as an experimental control in our previous reports
710 (Yamamoto et al., 2007; Iseda et al., 2016; Nakane et al., 2013).
711
712 **Plasma viral load quantitation**
713 Plasma viral RNA samples were extracted with High Pure Viral RNA kit (Roche Diagnostics).
714 Serial fivefold sample dilutions were amplified in quadruplicate by reverse transcription and
715 nested PCR using SIV_{mac239} *gag*-specific primers to determine end point via the Reed-Muench
716 method as described previously (Matano et al., 2004; Iseda et al., 2016). The lower limit of
717 detection is approximately 400 viral RNA copies/ml plasma. Viral loads have been previously
718 partially reported (Yamamoto et al., 2007; Nomura et al., 2012; Takahashi et al., 2013; Nakane
719 et al., 2013; Iwamoto et al., 2014).
720
721 **SIV_{mac239}-specific neutralization assay**
722 NAbs were titrated as described (Yamamoto et al., 2007; Iseda et al., 2016). Serial twofold
723 dilutions of heat-inactivated plasma, or polyclonal IgG affinity-purified with Protein G
724 Sepharose 4 Fast Flow (GE Healthcare) from heat-inactivated and filtered plasma were mixed
725 with 10 $TCID_{50}$ of SIV_{mac239} at a 1:1 ratio (5 μl:5 μl) in quadruplicate. After 45-min incubation at

726 room temperature, the 10 µl mixtures were added into 5 x 10^4 MT4-R5 cells/well in 96-well
727 plates. Progeny virus production in day 12 culture supernatants was examined by SIV p27
728 ELISA (ABL) to determine 100% neutralizing endpoint. The lower limit of titration is 1:2.
729 Neutralization in three out of four wells at a dilution of 1:2 is defined as marginally NAb-positive
730 (< 1:2). Results were comparable when the same assay was performed with macaque HSC-
731 F cells (Akari et al., 1996) as targets. NAb inducers R01-012, R02-004, R01-010, R02-007
732 and NAb non-inducer R01-011 were previously partially reported for their NAb titers measured
733 with the same method using MT4 cells as targets (Kawada et al., 2007), which derived
734 comparable results. For assessment of neutralizing activity in IgG, SIV_{mac239}-specific IgGs
735 purified from pools of plasma with SIV_{mac239}-specific NAb titers were obtained from each animal
736 as described (Yamamoto et al., 2007). After complement heat-inactivation at 56°C, 30 min and
737 0.45 µm filtration, IgGs were purified by Protein G Sepharose 4 Fast Flow (GE Healthcare)
738 and concentrated by Amicon Ultra 4, MW 50,000 (Millipore) to 30 mg/ml and similarly
739 examined for their 10 $TCID_{50}$ SIV_{mac239} killing titers on MT4-R5 cells.
740
741 **SIV Env-specific IgG ELISA and immunoblotting**
742 Plasma Env-specific IgG titers were measured as described (Nakane et al., 2013). SIV_{mac251}
743 Env gp120 (ImmunoDiagnostics) were coated on 96-well assay plates (BD) at 1000 ng/ml
744 (100 µl/well). Wells were prewashed with phosphate-buffered saline (PBS), blocked with 0.5%
745 bovine serum albumin (BSA)/PBS overnight and plasma samples were incubated at a 1:20
746 dilution (5 µl:95 µl) for 2 hours. Wells were washed with PBS and SIV Env-bound antibodies
747 were detected with a horseradish peroxidase (HRP)-conjugated goat anti-monkey IgG (H+L)
748 (Bethyl Laboratory) and SureBlue TMB 1-Component Microwell Peroxidase Substrate (KPL).
749 Absorbance at 450 nm was measured. Samples from week 0 pre-challenge and month 3,
750 month 6 and year 1 post-challenge were assessed in duplicate. Week 0 average values were
751 subtracted from corresponding later time point values for calibration. For immunoblotting, SIV
752 virion-specific IgGs in plasma were detected with a SIV_{mac239}-cross-reactive western blotting

753 system (ZeptoMetrix). In the NAb non-inducers, samples from those close to rapid progression
754 (euthanized due to AIDS progression within approximately 1 year) known for low plasma anti-
755 SIV reactivity (Hirsch et al., 2004; Nakane et al., 2013) were not included.
756
757 **Sequencing**
758 Sequencing was performed as described (Matano et al., 2004; Iseda et al., 2016). Viral cDNA
759 fragments spanning from nt (nucleotide) 4829 to nt 7000, nt 6843 to nt 8831 and nt 8677 to nt
760 10196 in SIV_{mac239} (GenBank accession number MM33262) covering SIV *env* and *nef* were
761 amplified from plasma viral RNA by nested RT-PCR using Prime-Script one-step RT-PCR kit
762 v2 (TaKaRa) and KOD-Plus v2 (Toyobo). PCR products were either directly sequenced or
763 subcloned with a TOP10-transforming TOPO blunt-end cloning system (Invitrogen).
764 Sequencing was performed using dye terminator chemistry with an ABI 3730 DNA sequencer
765 (Applied Biosystems). On average, 15 clones were obtained per sample and 20 clones were
766 assessed when *nef* mutations of interest in early time points were subdominant.
767
768 **SIV_{mac239}-specific $CD8^+$ T-cell responses**
769 Virus-specific $CD8^+$ T-cell frequencies were measured as described (Matano et al., 2004;
770 Iseda et al., 2016). Peripheral blood mononuclear cells (PBMCs) were cocultured for 6 hours
771 with autologous herpesvirus papio-immortalized B lymphoblastoid cell lines (B-LCLs) pulsed
772 with Nef peptides (Sigma-Aldrich Japan) at 1 μM concentration or as indicated otherwise
773 under GolgiStop (monensin, BD) presence. Intracellular gamma interferon (IFN-γ) staining
774 was performed using Cytofix/Cytoperm kit (BD) and the following conjugated anti-human
775 monoclonal antibodies (mAbs): anti-CD4-FITC (M-T477, BD Pharmingen), anti-CD8-PerCP
776 (SK1, BD Biosciences), anti-CD3-APC (SP34-2, BD Pharmingen) and anti-IFN-γ-PE (4S.B3,
777 BioLegend). Specific $CD8^+$ T-cell frequencies were determined by subtracting nonspecific IFN-
778 γ^+ $CD8^+$ T-cell frequencies from those after peptide-specific stimulation; frequencies beneath
779 100 cells/million PBMCs were considered negative. Cells acquired by FACS Canto II (BD)

780 were analyzed by FACS Diva (BD) and FlowJo (Treestar). Approximately 1 x 10^5 PBMCs were
781 gated per test.
782
783 **Nef-mediated signaling perturbation analysis**
784 Virus supernatants obtained from COS-1 cells after transfection with wild-type or mutant
785 SIV_{mac239} molecular clones were used for infection of $CD4^+$ T-cell lines, cynomolgus macaque-
786 derived HSC-F and rhesus macaque-derived HSR5.4 (Akari et al., 1996). QuikChange II XL
787 site-directed mutagenesis kit (Agilent Technologies) was used to construct mutant SIV_{mac239}
788 molecular clones possessing *nef* mutations Nef-G63E (G-to-A mutation at nt 9520) and Nef-
789 G63R (G-to-A mutation at nt 9519) from the wild-type SIV_{mac239} molecular clone (Kestler et al.,
790 1991) (nt number from GenBank accession number M33262). Cells (1 x 10^5 cells/well in U-
791 bottomed 96-well culture plates [BD]) were infected with wild-type or mutant SIV_{mac239} cultured
792 in RPMI-1640 medium supplemented with 10% fetal bovine serum (FBS) for indicated periods
793 at MOI 0.1 (intracellular signaling analysis) or 0.001 (supernatant analysis). Culture
794 supernatants were subjected to measurement of SIV capsid p27 concentrations by ELISA.
795 Harvested cells were fixed and permeabilized with Cytofix/Cytoperm kit, washed twice and
796 subjected to immunostaining. The following antibodies were used; anti-SIV_{mac251} Gag p27 mAb
797 (ABL) manually conjugated with Alexa 647 (Life Technologies), anti-SIV_{mac251} Nef mAb (clone
798 17, epitope peptide corresponding to SIV_{mac239} Nef 71-80 not including the residue G63:
799 Thermo Fisher Scientific/Pierce) manually conjugated with Alexa 488 or Alexa 647, anti-
800 human CD3-APC-Cy7 (SP34-2, BD Pharmingen), anti-human CD4-PerCP (L200, BD
801 Pharmingen), anti-human HLA-ABC-FITC (G46-2.6, BD Pharmingen), anti-human CXCR4-
802 APC (12G5, BioLegend), BST2-Alexa 647 (RS38E, BioLegend), Alexa 488-conjugated anti-
803 phospho-Akt (Ser473) (D9E, CST) and Alexa 488-conjugated anti-phospho-Akt (Thr308)
804 (C31E5E, CST). Cells acquired by FACS Canto II were analyzed by FACS Diva and FlowJo.
805 Approximately 5 x 10^4 cells were gated for each test.
806
807 **Ferritin ELISA**

808 Plasma ferritin levels in NAb inducers and control animals were analyzed by monkey ferritin
809 sandwich ELISA kit (LS Bio) according to the manufacturer's instructions.
810
811 **PI3K stimulation assay**
812 5 x 10^4 HSC-F cells were infected with wild-type or Nef G63E mutant SIV_{mac239} at MOI 0.2 and
813 cultured for 1 day in medium supplemented with 10% (normal), 1% (1/10 starvation) or 0.1%
814 (1/100 starvation) FBS. For ligand stimulation (**Figure 4-figure supplement 1C**), cells at the
815 end of 1-day culture were pulsed for 20 minutes with 40 ng/ml of recombinant human IFN-γ
816 (Gibco/Thermo Fisher Scientific), 100 IU/ml of recombinant human IL-2 (Roche Diagnostics)
817 or 10 μg/ml of SIV_{mac251} Env gp130 (ImmunoDx). Cells were intracellularly stained using
818 Cytofix/Cytoperm kit with anti-SIV_{mac251} Nef mAb or anti-SIV_{mac251} p27 mAb manually
819 conjugated to Alexa 647 and PE-conjugated anti-human phospho-Akt (Ser473) (D9E, CST) or
820 Alexa 488-conjugated anti-human phospho-Akt (Ser473). Cells acquired by FACS Canto II
821 were analyzed by FACS Diva and FlowJo. Approximately 7 x 10^4 HSC-F cells were gated per
822 test.
823
824 **Transcriptome analysis**
825 Total RNAs were extracted using RNeasy Plus Mini kit (Qiagen) from 2 x 10^6 HSC-F cells 1
826 day after infection with wild-type or Nef G63E mutant SIV_{mac239} at MOI 5. Negative control RNA
827 samples were extracted from 2 x 10^6 uninfected HSC-F cells after culture with the same
828 condition. Three sets of experiments were performed. Total RNA samples were subjected to a
829 quality control (QC) analysis using an Agilent 2100 Bioanalyzer. The obtained amounts of total
830 RNAs were: 12.37 ± 0.39 (uninfected), 8.80 ± 0.44 (wild-type) and 9.02 ± 0.17 (Nef G63E) μg
831 (P = 0.66 for wild-type versus Nef G63E by unpaired t test). In all samples, two bands of 18S
832 and 28S rRNA were confirmed and the RNA integrity number (RIN) was 10. 500 ng of total
833 RNA samples were processed with GeneChip WT Plus reagent (Affymetrix/Thermo Fisher
834 Scientific) to produce 150 μl of fragmented and labeled cDNA samples. These were incubated

835 with a Human Gene 2.0 ST Array (Affymetrix/Thermo Fisher Scientific) for 16 hours, 60 rpm
836 at 45°C using GeneChip hybridization oven 645 (Affymetrix/Thermo Fisher Scientific). Results
837 were scanned with GeneChip Scanner 3000 7G (Affymetrix/Thermo Fisher Scientific) and
838 processed with Affymetrix Expression Console Software (Affymetrix/Thermo Fisher Scientific)
839 according to the manufacturer's instructions. Expression values were normalized by the RMA
840 method. Genes above mean background expression within the cognate sample and showing
841 significant difference between wild-type and Nef G63E SIV ($P < 0.05$ via unpaired t test for
842 $\log_2$-transformed values, 768 candidates) were determined. Akt-related genes exhibiting a
843 change of approximately 10% or more were representatively extracted and manually aligned
844 by the authors.
845
846 **Peripheral CD4$^+$ T-cell surface staining**
847 Cryopreserved/thawed PBMCs were stained for 30 minutes at 4°C with the following reagents
848 or conjugated anti-human mAbs: Live/Dead Aqua (Life Technologies), anti-CD4-PerCP (L200,
849 BD Pharmingen), anti-CD8-APC-Cy7 (RPA-T8, BD Pharmingen), anti-CD3-Alexa 700 (SP34-
850 2, BD Pharmingen), anti-CD95-PE-Cy7 (DX2, eBioscience), anti-CXCR5-PE (87.1,
851 eBioscience), anti-PD-1-Brilliant Violet 421 (EH12.2H7, BioLegend) and anti-CXCR3-Alexa
852 488 (G025H7, BioLegend). Cells acquired by FACS LSRII Fortessa (BD) were analyzed by
853 FACS Diva and FlowJo. Approximately 1.5 x 10^5 PBMCs were gated per test.
854
855 **Proximity ligation assay (PLA)**
856 A flow cytometry-based arrangement of proximity ligation assay (PLA) (Avin et al., 2017) was
857 performed to quantitatively assess Nef binding to candidate interacting molecules. 1 x 10^5
858 HSC-F cells were infected with SIV_{mac239} at MOI 0.05 in U-bottomed plates and permeated
859 with Cytofix/Perm kit (BD Biosciences). After two washes, they were resuspended in 0.5%
860 BSA/PBS for prevention of experimental procedure-related loss and stained with mouse anti-
861 SIV_{mac251} Nef mAb (clone 17, Thermo Fisher Scientific/Pierce) or mouse IgG1 isotype control

862 mAb (P3.6.2.8.1, Abcam) in combination with either of the following rabbit antibodies: anti-
863 GβL (86B8, CST), anti-mTOR (7C10, CST), polyclonal anti-human PI3K p85 (Merck Millipore),
864 anti-PI3 Kinase p110α (C73F8, CST) or rabbit IgG1 isotype control mAb (DA1E, CST).
865 Antibody-stained cells were subsequently probed with Duolink In Situ PLA Probe anti-mouse
866 PLUS and anti-mouse MINUS probes (Sigma/Merck). Next, they were detected for
867 intermolecular binding using Duolink flow PLA detection kit (Green) (Sigma/Merck) with a
868 reaction time of 100 minutes for post-mouse/rabbit probe linking amplification. Finally, these
869 PLA-subjected cells were additionally stained with anti-SIV_{mac251} Gag p27 mAb manually
870 conjugated with Alexa 647 and anti-CD4-PerCP for 30 minutes for 20 minutes at 4°C. Cells
871 acquired by FACS Canto II were analyzed by FACS Diva and FlowJo. Approximately 1 x 10^5
872 cells were gated per test. Binding index (Y axis) was calculated by deriving the deviation from
873 the summation of: {baseline P: (MFI of background reaction with mouse isotype control/rabbit
874 isotype control) + anti-Nef antibody-derived background Q: [(MFI of reaction with mouse anti-
875 Nef/rabbit isotype control) - (MFI of background reaction with mouse isotype control/rabbit
876 isotype control)] + anti-binding partner antibody-derived background R:[(MFI of reaction with
877 mouse isotype control/rabbit anti-binding partner molecule) - (MFI of background reaction with
878 mouse isotype control/rabbit isotype control)]}.
879
880 **Co-immunoprecipitation analysis**
881 1 x 10^5 HSC-F cells were infected with SIV_{mac239} at MOI 0.05 in U-bottomed plates in
882 quadruplicate for each SIV strain for three days and pooled for each for acquiring cell pellets.
883 These pellets were lysed with Capturem IP & Co-IP Kit lysis buffer (Takara) and portions for
884 each were immunoprecipitated by anti-Sin1 mAb (D7G1A, CST) (1:50 dilution, 20 minutes,
885 room temperature). Spin column membrane-bound immunoprecipitates were obtained by
886 centrifugation with Capturem IP & Co-IP Kit (Clontech/Takara). Whole cell lysates and Sin1-
887 immunoprecipitated products were subjected to SDS-polyacrylamide gel electrophoresis
888 separation on a Mini Protean TGX 4-15% gel (BioRad) and transferred to a Immun-Blot PVDF
889 membrane (BioRad). Immunoblotting was performed by mouse anti-SIV_{mac251} Nef mAb (clone

890 17, Thermo Fisher Scientific/Pierce) primary antibody probing (1:1000 dilution, 18 hours, 4°
891 C) and Mouse TrueBlot ULTRA anti-mouse Ig HRP (eB144, Rockland Immunochemicals)
892 secondary antibody incubation (1:1000 dilution, 30 minutes, room temperature). Nef-specific
893 bands in infected controls were visualized by enhanced chemiluminescence using
894 SuperSignal West Pico PLUS (Thermo Fisher Scientific). Bands auto-detectable by Image
895 Lab software (BioRad) were analyzed for signal intensities. Uncropped images are provided
896 as supplementary data.
897
898 **Cell death assay**
899 Infected cell apoptosis was measured by methods previously described (Jauch et al., 2023).
900 1 x 10^5 HSC-F cells were infected with SIV_{mac239} at MOI 0.1 in U-bottomed plates (six
901 wells/control) for each SIV strain for three days. These cells were stained with CD4-FITC (M-
902 T477, BD Pharmingen) for 15 minutes at room temperature, washed once and next stained
903 with APC Annexin V (Biolegend) in Annexin V Binding Buffer (Biolegend) for 20 minutes at
904 room temperature. Stained reactions were then diluted fivefold with Annexin V Binding Buffer
905 and subjected to analysis. Cells acquired by FACS Lyric were analyzed by FACS Suite and
906 FlowJo. Approximately 1 x 10^4 HSC-F cells were gated per test.
907
908 **Quantitative *in vivo* imaging flow cytometry**
909 Cryopreserved/thawed lymph node cells (LNCs) from several persistently SIV-infected
910 macaques used in previous experiments (Nakane et al., 2013; Takahashi et al., 2013; Iwamoto
911 et al., 2014) were seeded in V-bottomed 96-well plates (Nunc) and blocked with 25 μg/ml of
912 anti-human CD4 (clone L200: BD) in 100 μl volume for 15 minutes at 4°C. After three washes,
913 they were stained with 10 μg/ml of recombinant SIV_{mac239} Env gp140-biotin (Immune
914 Technology) for 30 minutes at 4°C. Cells were then stained with anti-CD19-PC5.5 (J3-119,
915 Beckman Coulter), Live/Dead Aqua (Invitrogen) and streptavidin-APC-Cy7 (BioLegend) for 30
916 minutes at 4°C. After two washes, cells were processed with Cytofix/Cytoperm kit (BD) for 20

917 minutes at 4°C, washed twice, and next intracellularly stained with PE-conjugated anti-human
918 phospho-Akt (Ser473) (D9E, CST) and anti-SIV_{mac251} Nef mAb (clone 17, Thermo Fisher
919 Scientific/Pierce) manually conjugated with Alexa 488 or mouse IgG1 isotype control mAb
920 (P3.6.2.8.1, Abcam) for 30 minutes at 4°C. After final two washes, cells were suspended in
921 0.8% PFA/PBS. All centrifugations for washing (1,200 x g, 2 minutes) were performed at 4°C.
922 Cells were subjected to image acquisition with Image Stream X MKII imaging flow cytometer
923 (Amnis/Merck Millipore/Luminex) and analyzed with IDEAS 6.3 software (Amnis/Merck
924 Millipore/Luminex). Approximately 5 x 10^5 LNCs were acquired for analyses (**Figure 5**). A
925 custom-implemented linear discriminant analysis-based machine learning module (Luminex)
926 was utilized for verifying candidate Nef staining signal-related secondary parameters (**Figure**
927 **5** and **Figure 5-figure supplement 1A**) for their efficacy of target population separation.
928

929 **B-cell Nef invasion *in vitro* assay**

930 For Nef invasion assay, 5 x 10^4 HSC-F cells were infected at MOI 1 for 48 hours. These were
931 then additionally cocultured with 7.5 x 10^4 Ramos B cells for 12 hours with or without addition
932 of macaque T cell-stimulating anti-CD3 antibody (FN-18, Abcam) at 1 µg/ml. Cells were
933 double-stained with Alexa 488-conjugated mouse anti-Nef (clone 17: Thermo
934 Scientific/Pierce) and anti-CD19-PC-5.5 (J3-119, Beckman Coulter). For graphical
935 visualization (**Figure 6A**), interacting Nef^+ infected cell-invaded B cell doublet images acquired
936 with ImageStream X MKII (Amnis/Merck Millipore) were analyzed by IDEAS 6.3 (Amnis/Merck
937 Millipore/Luminex) with the defined noise-cancelling gating (via gating Nef pixel signal
938 $contrast^{lo}$-Nef mean pixel per $object^{hi}$ cells). For Nef invasion modulation verification on
939 conventional flow cytometry, the aforementioned culture condition was similarly used. Anti-
940 CD3 antibody (FN-18, Abcam) addition at 1 µg/ml and phorbol 12-myristate 13-acetate (PMA,
941 Sigma) plus ionomycin (Sigma) addition (10 ng/ml and 50 ng/ml, respectively) l were evaluated.
942 Cells were stained with Alexa 647-conjugated mouse anti-Nef (clone 17: Thermo
943 Scientific/Pierce), anti-CD19-PC-5.5 (J3-119, Beckman Coulter), anti-human phospho-Akt

944 (Ser473)-Alexa 488 (D9E, CST) and Live/Dead Near-IR (Invitrogen) for dead cell exclusion.
945 Dead cell frequencies were less than 3%. For viral phenotype evaluation, 1 x 10^5 HSC-F cells
946 (surface $CD40L^+$) were pre-infected at MOI 0.2 with wild type or Nef-G63E mutant SIV_{mac239}
947 six hours before coculture. 1.5 x 10^5 $CD20^+$ B cells, positively selected from fresh PBMCs of
948 uninfected rhesus macaques via anti-CD20 microbeads (Miltenyi Biotec), were cocultured with
949 these HSC-F cells at an E:T ratio of 2:3 for 3 days in the presence of 40 ng/ml carrier-free
950 recombinant human IL-4 (R&D Systems). Cells were surface-stained with anti-human CD20-
951 PerCP (2H7, BioLegend) and intracellularly stained using Cytofix/Cytoperm kit with anti-
952 SIV_{mac251} Nef mAb manually conjugated to Alexa 488 and Alexa 647-conjugated anti-human
953 phospho-Akt (Ser473) (D9E, CST). For **Figure 6B** and **Figure 6C**, Cells acquired by FACS
954 Canto II were analyzed by FACS Diva and FlowJo. Approximately 5 x 10^4 $CD20^+$ primary B
955 cells and 3 x 10^4 $CD19^+$ Ramos B cells were analyzed.
956
957 **Peripheral SIV Env-specific B-cell responses**
958 Peripheral SIV Env gp140-specific memory B cells (B_{mem}) and plasmablasts (PBs) were
959 measured by flow cytometry with procedures modified from previous reports and our
960 experience (Silveira et al., 2015; Hau et al., 2022). First, cryopreserved/thawed PBMCs
961 seeded in V-bottomed 96-well plates (Nunc) were blocked with 25 μg/ml of anti-human CD4
962 (clone L200: BD) in 100 μl volume for 15 minutes at 4°C. This concentration attains blockade
963 of promiscuous SIV Env binding to CD4 comparable to levels by magnetic depletion of $CD3^+$
964 T cells (data not shown). After three washes, they were next stained with 10 μg/ml of
965 recombinant SIV_{mac239} Env gp140-biotin (Immune Technology) for 30 minutes at 4°C. They
966 were subsequently stained with the following anti-human antibodies and fluorochromes for 30
967 minutes at 4°C with combinations as follows; PB/B_{mem}: anti-CD3-APC-Cy7 (SP34-2, BD
968 Pharmingen), anti-CD8-APC-Cy7 (RPA-T8, BD Pharmingen), anti-CD14-APC-Cy7 (M5E2,
969 BioLegend), anti-CD16-APC-Cy7 (3G8, BioLegend), streptavidin-Brilliant Violet 421
970 (BioLegend), anti-CD19-PC5.5 (J3-119, Beckman Coulter) and Live/Dead Aqua (Invitrogen);

971 PB: anti-CD10-APC-Cy7 (HI10a, BioLegend), anti-CD11c-PE-Cy7 (3.9, BioLegend), anti-
972 CD123-PE-Cy7 (6H6, BioLegend) and anti-HLA-DR-PE-Texas Red (TU36, Invitrogen); B_{mem}:
973 anti-CD27-PE/Dazzle 594 (M-T271, BioLegend), anti-CD10-PE-Cy7 (HI10a, BioLegend), anti-
974 IgD-FITC (DaKo), anti-CD38-Alexa 647 (AT1, Santa Cruz Biotechnology), anti-IgG-Alexa 700
975 (G18-145, BD Pharmingen) and anti-CD138-PE (DL-101, eBioscience). After two washes,
976 B_{mem} samples were suspended in 0.8% PFA/PBS. For PB staining, surface-stained cells were
977 further processed with Cytofix/Cytoperm kit (BD) for 20 minutes at 4°C, washed twice, and
978 next intracellularly stained with 10 μg/ml of recombinant SIV_{mac239} Env gp140-biotin (Immune
979 Technology) for 30 minutes at 4°C. After three washes, they were next stained with anti-human
980 IgG-PE (G18-145, BD), anti-human/mouse IRF4-eFluor 660 (3E4, eBioscience), anti-human
981 Ki67-Alexa 700 (B56, BD Pharmingen) and streptavidin-Alexa 488 (BioLegend) for 30 minutes
982 at 4°C. After final two washes, cells were suspended in 0.8% PFA/PBS. Cells acquired with
983 FACS LSRII Fortessa were analyzed with FACS Diva and FlowJo. Approximately 1.5 x 10^5
984 PBMCs were acquired for B_{mem} and 4 x 10^5 PBMCs were acquired for PB analyses (**Figure**
985 **6**). All centrifugations for washing (1,200 x g, 2 minutes) were performed at 4°C. Env-specific
986 PB frequencies were 0 cells/million PBMCs for pre-challenge samples in all animals examined,
987 ruling out background confounding for high-sensitivity quantitation of the population.
988
989 **Statistical Analysis**
990 Analyses were performed via Prism 8 (GraphPad Software). $P < 0.05$ were considered
991 significant in two-tailed unpaired t tests, paired t tests, Mann Whitney U tests, Fisher's exact
992 tests, Wilcoxon signed-rank tests, one-way ANOVA with Tukey's post-hoc multiple comparison
993 tests and two-way ANOVA with Sidak's post-hoc multiple comparison tests. For analysis of
994 Nef-invaded B-cell pAkt levels, median fluorescence intensities (mFIs) were analyzed due to
995 relatively small numbers of Nef^+ B cells. Analyses involving pAkt Ser473 levels all derived
996 comparable results between mFI and MFI for wild type versus Nef G63E virus. Machine

997 learning-based rating of Nef signal parameters was verified with IDEAS 6.3 Machine Learning

998 Module (Luminex).

References

Adnan, S., Reeves, R.K., Gillis, J., Wong, F.E., Yu, Y., Camp, J.V., Li, Q., Connole, M., Li, Y., Piatak, M. Jr., et al. (2016). Persistent low-level replication of SIVΔnef drives maturation of antibody and CD8 T cell responses to induce protective immunity against vaginal SIV infection. *PLoS Pathog*. 12, e1006104.

Akari, H., Mori, K., Terao, K., Otani, I., Fukasawa, M., Mukai, R., and Yoshikawa, Y. (1996). In vitro immortalization of Old World monkey T lymphocytes with Herpesvirus saimiri: its susceptibility to infection with simian immunodeficiency viruses. *Virology* 218, 382–388.

Al Qureshah, F., Sagadiev, S., Thouvenel, C.D., Liu, S., Hua, Z., Hou, B., Acharya, M., James, R.G., and Rawlings, D.J. (2021). Activated PI3Kδ signals compromise plasma cell survival via limiting autophagy and increasing ER stress. *J. Exp. Med.* 218, e20211035.

Angulo, I., Vadas, O., Garçon, F., Banham-Hall, E., Plagnol, V., Leahy, T.R., Baxendale, H., Coulter, T., Curtis, J., Wu, C., et al. (2013). Phosphoinositide 3-kinase δ gene mutation predisposes to respiratory infection and airway damage. *Science* 342, 866–871.

Asano, T., Okada, S., Tsumura, M., Yeh, T.W., Mitsui-Sekinaka, K., Tsujita, Y., Ichinose, Y., Shimada, A., Hashimoto, K., Wada, T., et al. (2018). Enhanced AKT phosphorylation of circulating B cells in patients with activated PI3Kδ syndrome. *Front. Immunol.* 9, 568.

Avery, D.T., Kane, A., Nguyen, T., Lau, A., Nguyen, A., Lenthall, H., Payne, K., Shi, W., Brigden, H., French, E., et al. (2018). Germline-activating mutations in PIK3CD compromise B cell development and function. *J. Exp. Med.* 215, 2073–2095.

1026 Avin, A., Levy, M., Porat, Z., and Abramson, J. (2017) Quantitative analysis of protein-protein
1027 interactions and post-translational modifications in rare immune populations. *Nat. Commun.*
1028 8, 1524.
1029
1030 Battegay, M., Moskophidis, D., Waldner, H., Bründler, M.A., Fung-Leung, W.P., Mak, T.W.,
1031 Hengartner, H., and Zinkernagel, R.M. (1993). Impairment and delay of neutralizing antiviral
1032 antibody responses by virus-specific cytotoxic T cells. *J. Immunol.* 151, 5408–5415.
1033
1034 Baumjohann, D., Preite, S., Reboldi, A., Ronchi, F., Ansel, K.M., Lanzavecchia, A., and
1035 Sallusto, F. (2013). Persistent antigen and germinal center B cells sustain T follicular helper
1036 cell responses and phenotype. *Immunity* 38, 596–605.
1037
1038 Bradley, T., Peppa, D., Pedroza-Pacheco, I., Li, D., Cain, D.W., Henao, R., Venkat, V., Hora,
1039 B., Chen, Y., Vandergrift, N.A., et al. (2018). RAB11FIP5 Expression and Altered Natural Killer
1040 Cell Function Are Associated with Induction of HIV Broadly Neutralizing Antibody Responses.
1041 *Cell* 175, 387–399.e17.
1042
1043 Burns, D.P., Collignon, C., and Desrosiers, R.C. (1993). Simian immunodeficiency virus
1044 mutants resistant to serum neutralization arise during persistent infection of rhesus monkeys.
1045 *J. Virol.* 67, 4104–4113.
1046
1047 Campbell, E.M., Nunez, R., and Hope, T.J. (2004). Disruption of the actin cytoskeleton can
1048 complement the ability of Nef to enhance human immunodeficiency virus type 1 infectivity. *J.*
1049 *Virol.* 78, 5745–5755.
1050
1051 Coulter, T.I., Chandra, A., Bacon, C.M., Babar, J., Curtis, J., Screaton, N., Goodlad, J.R.,
1052 Farmer, G., Steele, C.L., Leahy, T.R., et al. (2017). Clinical spectrum and features of activated

1053 phosphoinositide 3-kinase δ syndrome: A large patient cohort study. *J. Allergy Clin. Immunol.*
1054 139, 597–606.e4.
1055
1056 Cubas, R.A., Mudd, J.C., Savoye, A.L., Perreau, M., van Grevenynghe, J., Metcalf, T., Connick,
1057 E., Meditz, A., Freeman, G.J., Abesada-Terk, G. Jr., et al. (2013). Inadequate T follicular cell
1058 help impairs B cell immunity during HIV infection. *Nat. Med.* 19, 494–499.
1059
1060 Cumont, M.C., Diop, O., Vaslin, B., Elbim, C., Viollet, L., Monceaux, V., Lay, S., Silvestri, G.,
1061 Le Grand, R., Müller-Trutwin, M., et al. (2008). Early divergence in lymphoid tissue apoptosis
1062 between pathogenic and nonpathogenic simian immunodeficiency virus infections of
1063 nonhuman primates. *J. Virol.* 82, 1175–1184.
1064
1065 Dornan, G.L., Siempelkamp, B.D., Jenkins, M.L., Vadas, O., Lucas, C.L., and Burke, J.E.
1066 (2017). Conformational disruption of PI3Kδ regulation by immunodeficiency mutations in
1067 PIK3CD and PIK3R1. *Proc. Natl. Acad. Sci. USA* 114, 1982–1987.
1068
1069 Douek, D.C., Brenchley, J.M., Betts, M.R., Ambrozak, D.R., Hill, B.J., Okamoto, Y., Casazza,
1070 J.P., Kuruppu, J., Kunstman, K., Wolinsky, S., et al. (2002). HIV preferentially infects HIV-
1071 specific $CD4^+$ T cells. *Nature* 417, 95–98.
1072
1073 Evans, D.T., O'Connor, D.H., Jing, P., Dzuris, J.L., Sidney, J., da Silva, J., Allen, T.M., Horton,
1074 H., Venham, J.E., Rudersdorf, R.A., et al. (1999). Virus-specific cytotoxic T-lymphocyte
1075 responses select for amino-acid variation in simian immunodeficiency virus Env and Nef. *Nat.*
1076 *Med.* 5, 1270–1276.
1077
1078 Fallet, B., Narr, K., Ertuna, Y.I., Remy, M., Sommerstein, R., Cornille, K., Kreutzfeldt, M., Page,
1079 N., Zimmer, G., Geier, F., et al. (2016). Interferon-driven deletion of antiviral B cells at the onset
1080 of chronic infection. *Sci. Immunol.* 1, pii: eaah6817.

1081

1082 François, F., and Klotman, M.E. (2003). Phosphatidylinositol 3-kinase regulates human
1083 immunodeficiency virus type 1 replication following viral entry in primary CD4+ T lymphocytes
1084 and macrophages. *J. Virol.* 77, 2539–2549.

1085

1086 Fruman, D.A., Snapper, S.B., Yballe, C.M., Davidson, L., Yu, J.Y., Alt, F.W., and Cantley, L.C.
1087 (1999). Impaired B cell development and proliferation in absence of phosphoinositide 3-kinase
1088 p85alpha. *Science* 283, 393–397.

1089

1090 Fukazawa, Y., Park, H., Cameron, M.J., Lefebvre, F., Lum, R., Coombes, N., Mahyari, E.,
1091 Hagen, S.I., Bae, J.Y., Reyes, M.D. 3rd., et al. (2012). Lymph node T cell responses predict
1092 the efficacy of live attenuated SIV vaccines. *Nat. Med.* 18, 1673–1681.

1093

1094 Gauduin, M.C., Yu, Y., Barabasz, A., Carville, A., Piatak, M., Lifson, J.D., Desrosiers, R.C.,
1095 and Johnson, R.P. (2006). Induction of a virus-specific effector-memory CD4+ T cell response
1096 by attenuated SIV infection. *J. Exp. Med.* 203, 2661–2672.

1097

1098 Geyer, M., Fackler, O.T., and Peterlin, B.M. (2001). Structure--function relationships in HIV-1
1099 Nef. *EMBO Rep.* 2, 580–585.

1100

1101 Gitlin, A.D., Shulman, Z. and Nussenzweig, M.C. (2014). Clonal selection in the germinal
1102 centre by regulated proliferation and hypermutation. *Nature* 509, 637–640.

1103

1104 Gray, E.S., Madiga, M.C., Hermanus, T., Moore, P.L., Wibmer, C.K., Tumba, N.L., Werner, L.,
1105 Mlisana, K., Sibeko, S., Williamson, C., et al. (2011). The neutralization breadth of HIV-1
1106 develops incrementally over four years and is associated with CD4+ T cell decline and high
1107 viral load during acute infection. *J. Virol.* 85, 4828–4840.

1108

1109 Haigwood, N.L., Watson, A., Sutton, W.F., McClure, J., Lewis, A., Ranchalis, J., Travis, B.,
1110 Voss, G., Letvin, N.L., Hu, S.L., et al. (1996). Passive immune globulin therapy in the
1111 SIV/macaque model: early intervention can alter disease profile. *Immunol. Lett.* 51, 107–114.
1112
1113 Haralick, R.M., Shanmugam, K., and Dinstein, I. (1973) Textural features for image
1114 classification. *IEEE Transactions on Systems, Man, and Cybernetics* SMC-3, 610–621.
1115
1116 Harris, R.S., Bishop, K.N., Sheehy, A.M., Craig, H.M., Petersen-Mahrt, S.K., Watt, I.N.,
1117 Neuberger, M.S., and Malim, M.H. (2003). DNA deamination mediates innate immunity to
1118 retroviral infection. *Cell* 113, 803–809.
1119
1120 Hashimoto, M., Bhuyan, F., Hiyoshi, M., Noyori, O., Nasser, H., Miyazaki, M., Saito, T., Kondoh,
1121 Y., Osada, H., Kimura, S., et al. (2016). Potential role of the formation of tunneling nanotubes
1122 in HIV-1 spread in macrophages. *J. Immunol.* 196, 1832–1841.
1123
1124 Hau, T.T.T., Nishizawa, M., Harada, S., Phan, M.H., Kanno, Y., Nomura, T., Matsuoka, S.,
1125 Kawana-Tachikawa, A., Hall, W.W., Matano, T., et al. (2022). Association of envelope-specific
1126 B-cell differentiation and viral selective pressure signatures in HIV-1 CRF01_AE infection.
1127 *AIDS* 36, 1629–1641.
1128
1129 Havenar-Daughton, C., Carnathan, D.G., Torrents de la Peña, A., Pauthner, M., Briney, B.,
1130 Reiss, S.M., Wood, J.S., Kaushik, K., van Gils, M.J., Rosales, S.L., et al. (2016). Direct Probing
1131 of Germinal Center Responses Reveals Immunological Features and Bottlenecks for
1132 Neutralizing Antibody Responses to HIV Env Trimer. *Cell Rep.* 17, 2195–2209.
1133
1134 Hirsch, V.M., Santra, S., Goldstein, S., Plishka, R., Buckler-White, A., Seth, A., Ourmanov, I.,
1135 Brown, C.R., Engle, R., Montefiori, D., et al. (2004). Immune failure in the absence of profound
1136 CD4+ T-lymphocyte depletion in simian immunodeficiency virus-infected rapid progressor

1137 macaques. *J. Virol.* 78, 275–284.
1138
1139 Hoof, I., Peters, B., Sidney, J., Pedersen, L.E., Sette, A., Lund, O., Buus, S., and Nielsen, M..
1140 (2009). NetMHCpan, a method for MHC class I binding prediction beyond humans.
1141 *Immunogenetics* 61, 1–13.
1142
1143 Hunziker, L., Recher, M., Macpherson, A.J., Ciurea, A., Freigang, S., Hengartner, H., and
1144 Zinkernagel, R.M. (2003). Hypergammaglobulinemia and autoantibody induction mechanisms
1145 in viral infections. *Nat. Immunol.* 4, 343–349.
1146
1147 Iseda, S., Takahashi, N., Poplimont, H., Nomura, T., Seki, S., Nakane, T., Nakamura, M., Shi,
1148 S., Ishii, H., Furukawa, S., et al. (2016). Biphasic CD8+ T-cell defense in simian
1149 immunodeficiency virus control by acute-phase passive neutralizing antibody immunization. *J.*
1150 *Virol.* 90, 6276–6290.
1151
1152 Ishii, H., Kawada, M., Tsukamoto, T., Yamamoto, H., Matsuoka, S., Shiino, T., Takeda, A.,
1153 Inoue, M., Iida, A., Hara, H., et al. (2012). Impact of vaccination on cytotoxic T lymphocyte
1154 immunodominance and cooperation against simian immunodeficiency virus replication in
1155 rhesus macaques. *J. Virol.* 86, 738–745.
1156
1157 Iwamoto, N., Takahashi, N., Seki, S., Nomura, T., Yamamoto, H., Inoue, M., Shu, T., Naruse,
1158 T.K., Kimura, A., and Matano, T. (2014). Control of simian immunodeficiency virus replication
1159 by vaccine-induced Gag- and Vif-specific $CD8^+$ T cells. *J. Virol.* 88, 425–433.
1160
1161 Jauch, A.J., Bignucolo, O., Seki, S., Ghraichy, M., Delmonte, O.M., von Niederhäusern, V.,
1162 Higgins, R., Ghosh, A., Nishizawa, M., Tanaka, M., et al. (2023). Autoimmunity and
1163 immunodeficiency associated with monoallelic LIG4 mutations via haploinsufficiency. *J.*
1164 *Allergy Clin. Immunol.* 152, 500–516.

1165

1166 Jia, B., Serra-Moreno, R., Neidermyer, W., Rahmberg, A., Mackey, J., Fofana, I.B., Johnson,
1167 W.E., Westmoreland, S., and Evans, D.T. (2009). Species-specific activity of SIV Nef and HIV-
1168 1 Vpu in overcoming restriction by tetherin/BST2. *PLoS Pathog.* 5, e1000429.

1169

1170 Joas, S., Parrish, E.H., Gnanadurai, C.W., Lump, E., Stürzel, C.M., Parrish, N.F., Learn, G.H.,
1171 Sauermann, U., Neumann, B., Rensing, K.M., et al. (2018) Species-specific host factors rather
1172 than virus-intrinsic virulence determine primate lentiviral pathogenicity. *Nat. Commun.* 9, 1371.

1173

1174 Joas, S., Sauermann, U., Roshani, B., Klippert, A., Daskalaki, M., Mätz-Rensing, K., Stolte-
1175 Leeb, N., Heigele, A., Tharp, G.K., Gupta, P.M., et al. (2020). Nef-Mediated CD3-TCR
1176 Downmodulation Dampens Acute Inflammation and Promotes SIV Immune Evasion. *Cell Rep.*
1177 30, 2261–2274.e7.

1178

1179 Johnson, R.P., Glickman, R.L., Yang, J.Q., Kaur, A., Dion, J.T., Mulligan, M.J., and Desrosiers,
1180 R.C. (1997). Induction of vigorous cytotoxic T-lymphocyte responses by live attenuated simian
1181 immunodeficiency virus. *J. Virol.* 71, 7711–7718.

1182

1183 Jolly, C., Kashefi, K., Hollinshead, M., and Sattentau, Q.J. (2004). HIV-1 cell to cell transfer
1184 across an Env-induced, actin-dependent synapse. *J. Exp. Med.* 199, 283–293.

1185

1186 Junt, T., Moseman, E.A., Iannacone, M., Massberg, S., Lang, P.A., Boes, M., Fink, K.,
1187 Henrickson, S.E., Shayakhmetov, D.M., Di Paolo, N.C., et al. (2007). Subcapsular sinus
1188 macrophages in lymph nodes clear lymph-borne viruses and present them to antiviral B cells.
1189 *Nature* 450, 110–114.

1190

1191 Kawada, M., Tsukamoto, T., Yamamoto, H., Takeda, A., Igarashi, H., Watkins, D.I., and Matano,
1192 T. (2007). Long-term control of simian immunodeficiency virus replication with central memory

1193 CD4+ T-cell preservation after nonsterile protection by a cytotoxic T-lymphocyte-based
1194 vaccine. *J. Virol.* 81, 5202–5211.
1195
1196 Kennedy, S.G., Wagner, A.J., Conzen, S.D., Jordán, J., Bellacosa, A., Tsichlis, P.N., and Hay,
1197 N. (1997). The PI 3-kinase/Akt signaling pathway delivers an anti-apoptotic signal. *Genes Dev.*
1198 11, 701–713.
1199
1200 Kestler, H.W. 3rd, Ringler, D.J., Mori, K., Panicali, D.L., Sehgal, P.K., Daniel, M.D., and
1201 Desrosiers, R.C. (1991). Importance of the nef gene for maintenance of high virus loads and
1202 for development of AIDS. *Cell* 65, 651–662.
1203
1204 Khan, H., Sumner, R.P., Rasaiyaah, J., Tan, C.P., Rodriguez-Plata, M.T., Van Tulleken, C.,
1205 Fink, D., Zuliani-Alvarez, L., Thorne, L., Stirling, D., et al. (2020). HIV-1 Vpr antagonizes innate
1206 immune activation by targeting karyopherin-mediated NF-κB/IRF3 nuclear transport. *Elife* 9,
1207 e60821.
1208
1209 Kim, D.H., Sarbassov, D.D., Ali, S.M., Latek, R.R., Guntur, K.V., Erdjument-Bromage, H.,
1210 Tempst, P., and Sabatini, D.M. (2003). GbetaL, a positive regulator of the rapamycin-sensitive
1211 pathway required for the nutrient-sensitive interaction between raptor and mTOR. *Mol. Cell* 11,
1212 895–904.
1213
1214 Kirchhoff, F., Greenough, T.C., Brettler, D.B., Sullivan, L.L. and Desrosiers, R.C. (1995).
1215 Absence of intact nef sequences in a long-term, nonprogressing survivor of HIV-1 infection. *N.*
1216 *Engl. J. Med. 332*, 228–232.
1217
1218 Kumar, A., Abbas, W., Colin, L., Khan, K.A., Bouchat, S., Varin, A., Larbi, A., Gatot, J.S.,
1219 Kabeya, K., Vanhulle, C., et al. (2016). Tuning of AKT-pathway by Nef and its blockade by

1220 protease inhibitors results in limited recovery in latently HIV infected T-cell line. *Sci. Rep.* 6,
1221 24090.
1222
1223 Kumar, V., Scandella, E., Danuser, R., Onder, L., Nitschké, M., Fukui, Y., Halin, C., Ludewig,
1224 B., and Stein, J.V. (2010). Global lymphoid tissue remodeling during a viral infection is
1225 orchestrated by a B cell-lymphotoxin-dependent pathway. *Blood* 115, 4725–4733.
1226
1227 Laguette, N., Sobhian, B., Casartelli, N., Ringeard, M., Chable-Bessia, C., Ségéral, E., Yatim,
1228 A., Emiliani, S., Schwartz, O., and Benkirane, M. (2011). SAMHD1 is the dendritic- and
1229 myeloid-cell-specific HIV-1 restriction factor counteracted by Vpx. *Nature* 474, 654–657.
1230
1231 Langer, S., Hammer, C., Hopfensperger, K., Klein, L., Hotter, D., De Jesus, P.D., Herbert, K.M.,
1232 Pache, L., Smith, N., van der Merwe, J.A., et al. (2019) HIV-1 Vpu is a potent transcriptional
1233 suppressor of NF-κB-elicited antiviral immune responses. *Elife* 8, e41930.
1234
1235 Leuchowius, K.J., Weibrecht, I., Landegren, U., Gedda, L., and Söderberg, O. (2009). Flow
1236 cytometric in situ proximity ligation analyses of protein interactions and post-translational
1237 modification of the epidermal growth factor receptor family. *Cytometry A* 75, 833–839.
1238
1239 Levesque, M.C., Moody, M.A., Hwang, K.K., Marshall, D.J., Whitesides, J.F., Amos, J.D.,
1240 Gurley, T.C., Allgood, S., Haynes, B.B., Vandergrift, N.A., et al. (2009). Polyclonal B cell
1241 differentiation and loss of gastrointestinal tract germinal centers in the earliest stages of HIV-
1242 1 infection. *PLoS Med.* 6, e1000107.
1243
1244 Lichterfeld, M., Kavanagh, D.G., Williams, K.L., Moza, B., Mui, S.K., Miura, T., Sivamurthy, R.,
1245 Allgaier, R., Pereyra, F., Trocha, A., et al. (2007). A viral CTL escape mutation leading to
1246 immunoglobulin-like transcript 4-mediated functional inhibition of myelomonocytic cells. *J. Exp.*
1247 *Med.* 204, 2813–2824.

1248

1249 Limon, J.J., So, L., Jellbauer, S., Chiu, H., Corado, J., Sykes, S.M., Raffatellu, M., and Fruman,
1250 D.A. (2014). mTOR kinase inhibitors promote antibody class switching via mTORC2 inhibition.
1251 *Proc. Natl. Acad. Sci. USA* 111, E5076–5085.

1252

1253 Lindqvist, M., van Lunzen, J., Soghoian, D.Z., Kuhl, B.D., Ranasinghe, S., Kranias, G.,
1254 Flanders, M.D., Cutler, S., Yudanin, N., Muller, M.I., et al. (2012). Expansion of HIV-specific T
1255 follicular helper cells in chronic HIV infection. *J. Clin. Invest.* 122, 3271–3280.

1256

1257 Locci, M., Havenar-Daughton, C., Landais, E., Wu, J., Kroenke, M.A., Arlehamn, C.L., Su, L.F.,
1258 Cubas, R., Davis, M.M., Sette, A., et al. (2013). Human circulating PD-1^{+}CXCR3^{-}CXCR5^{+}
1259 memory Tfh cells are highly functional and correlate with broadly neutralizing HIV antibody
1260 responses. *Immunity* 39, 758–769.

1261

1262 Lucas, C.L., Kuehn, H.S., Zhao, F., Niemela, J.E., Deenick, E.K., Palendira, U., Avery, D.T.,
1263 Moens, L., Cannons, J.L., Biancalana, M., et al. (2014). Dominant-activating germline
1264 mutations in the gene encoding the PI(3)K catalytic subunit p110δ result in T cell senescence
1265 and human immunodeficiency. *Nat. Immunol.* 15*,* 88–97.

1266

1267 Luo, W., Hawse, W., Conter, L., Trivedi, N., Weisel, F., Wikenheiser, D., Cattley, R.T., and
1268 Shlomchik, M.J. (2019). The AKT kinase signaling network is rewired by PTEN to control
1269 proximal BCR signaling in germinal center B cells. *Nat. Immunol.* 20, 736–746.

1270

1271 Marzec, M., Liu, X., Kasprzycka, M., Witkiewicz, A., Raghunath, P.N., El-Salem, M., Robertson,
1272 E., Odum, N., and Wasik, M.A. (2008). IL-2- and IL-15-induced activation of the rapamycin-
1273 sensitive mTORC1 pathway in malignant CD4+ T lymphocytes. *Blood* 111, 2181–2189.

1274

1275 Mason, R.D., Welles, H.C., Adams, C., Chakrabarti, B.K., Gorman, J., Zhou, T., Nguyen, R.,
1276 O'Dell, S., Lusvarghi, S., Bewley, C.A., et al. (2016). Targeted Isolation of Antibodies Directed
1277 against Major Sites of SIV Env Vulnerability. *PLoS Pathog.* 12, e1005537.
1278
1279 Matano, T., Kobayashi, M., Igarashi, H., Takeda, A., Nakamura, H., Kano, M., Sugimoto, C.,
1280 Mori, K., Iida, A., Hirata, T., et al. (2004). Cytotoxic T lymphocyte-based control of simian
1281 immunodeficiency virus replication in a preclinical AIDS vaccine trial. *J. Exp. Med.* 199, 1709–
1282 1718.
1283
1284 Mattapallil, J.J., Douek, D.C., Hill, B., Nishimura, Y., Martin, M., and Roederer, M. (2005).
1285 Massive infection and loss of memory CD4+ T cells in multiple tissues during acute SIV
1286 infection. *Nature* 434, 1093–1097.
1287
1288 McDonald, D., Wu, L., Bohks, S.M., KewalRamani, V.N., Unutmaz, D., and Hope, T.J. (2003).
1289 Recruitment of HIV and its receptors to dendritic cell-T cell junctions. *Science* 300, 1295–1297.
1290
1291 Mikell, I., Sather, D.N., Kalams, S.A., Altfeld, M., Alter, G., and Stamatatos, L. (2011).
1292 Characteristics of the earliest cross-neutralizing antibody response to HIV-1. *PLoS Pathog.* 7,
1293 e1001251.
1294
1295 Moir, S., Malaspina, A., Ogwaro, K.M., Donoghue, E.T., Hallahan, C.W., Ehler, L.A., Liu, S.,
1296 Adelsberger, J., Lapointe, R., Hwu, P., et al. (2001). HIV-1 induces phenotypic and functional
1297 perturbations of B cells in chronically infected individuals. *Proc. Natl. Acad. Sci. USA* 98,
1298 10362–10367.
1299
1300 Moody, M.A., Pedroza-Pacheco, I., Vandergrift, N.A., Chui, C., Lloyd, K.E., Parks, R.,
1301 Soderberg, K.A., Ogbe, A.T., Cohen, M.S., Liao, H.X., Gao, F., et al. (2016). Immune

1302 perturbations in HIV-1-infected individuals who make broadly neutralizing antibodies. *Sci.*
1303 *Immunol.* 1, aag0851.
1304
1305 Moore, P.L., Gray, E.S., Wibmer, C.K., Bhiman, J.N., Nonyane, M., Sheward, D.J., Hermanus,
1306 T., Bajimaya, S., Tumba, N.L., Abrahams, M.R., et al. (2012). Evolution of an HIV glycan-
1307 dependent broadly neutralizing antibody epitope through immune escape. *Nat. Med.* 18,
1308 1688–1692.
1309
1310 Moukambi, F., Rabezanahary, H., Rodrigues, V., Racine, G., Robitaille, L., Krust, B., Andreani,
1311 G., Soundaramourty, C., Silvestre, R., Laforge, M., et al. (2015). Early loss of splenic Tfh cells
1312 in SIV-infected rhesus macaques. *PLoS Pathog.* 11, e1005287.
1313
1314 Moukambi, F., Rabezanahary, H., Fortier, Y., Rodrigues, V., Clain, J., Benmadid-Laktout, G.,
1315 Zghidi-Abouzid, O., Soundaramourty, C., Laforge, M., and Estaquier, J. (2019) Mucosal T
1316 follicular helper cells in SIV-infected rhesus macaques: contributing role of IL-27. *Mucosal*
1317 *Immunol.* 12, 1038–1054.
1318
1319 Nakane, T., Nomura, T., Shi, S., Nakamura, M., Naruse, T.K., Kimura, A., Matano, T., and
1320 Yamamoto, H. (2013). Limited impact of passive non-neutralizing antibody immunization in
1321 acute SIV infection on viremia control in rhesus macaques. *PLoS ONE* 8, e73453.
1322
1323 Naruse, T.K., Chen, Z., Yanagida, R., Yamashita, T., Saito, Y., Mori, K., Akari, H., Yasutomi, Y.,
1324 Miyazawa, M., Matano, T., et al. (2010). Diversity of MHC class I genes in Burmese-origin
1325 rhesus macaques. *Immunogenetics* 62, 601–611.
1326
1327 Neil, S.J., Zang, T., and Bieniasz, P.D. (2008). Tetherin inhibits retrovirus release and is
1328 antagonized by HIV-1 Vpu. *Nature* 451, 425–430.
1329

1330 Ng, C.T., Jaworski, J.P., Jayaraman, P., Sutton, W.F., Delio, P., Kuller, L., Anderson, D.,
1331 Landucci, G., Richardson, B.A., Burton, D.R., et al. (2010). Passive neutralizing antibody
1332 controls SHIV viremia and enhances B cell responses in infant macaques. *Nat. Med.* 16, 1117–
1333 1119.
1334
1335 Nguyen, H., Ramana, C.V., Bayes, J., and Stark, G.R. (2001). Roles of phosphatidylinositol 3-
1336 kinase in interferon-gamma-dependent phosphorylation of STAT1 on serine 727 and activation
1337 of gene expression. *J. Biol. Chem.* 276, 33361–33368.
1338
1339 Nishimura, Y., Gautam, R., Chun, T.W., Sadjadpour, R., Foulds, K.E., Shingai, M., Klein, F.,
1340 Gazumyan, A., Golijanin, J., Donaldson, M., et al. (2017). Early antibody therapy can induce
1341 long-lasting immunity to SHIV. *Nature* 543, 559–563.
1342
1343 Nomura, T., Yamamoto, H., Shiino, T., Takahashi, N., Nakane, T., Iwamoto, N., Ishii, H.,
1344 Tsukamoto, T., Kawada, M., Matsuoka, S., et al. (2012). Association of major histocompatibility
1345 complex class I haplotypes with disease progression after simian immunodeficiency virus
1346 challenge in Burmese rhesus macaques. *J. Virol.* 86, 6481–6490.
1347
1348 Nutt, S.L., Hodgkin, P.D., Tarlinton, D.M., and Corcoran, L.M. (2015). The generation of
1349 antibody-secreting plasma cells. *Nat. Rev. Immunol.* 15, 160–171.
1350
1351 Omori, S.A., Cato, M.H., Anzelon-Mills, A., Puri, K.D., Shapiro-Shelef, M., Calame, K., and
1352 Rickert, R.C. (2006). Regulation of class-switch recombination and plasma cell differentiation
1353 by phosphatidylinositol 3-kinase signaling. *Immunity* 25, 545–557.
1354
1355 Perfetto, S.P., Chattopadhyay, P.K., Lamoreaux, L., Nguyen, R., Ambrozak, D., Koup, R.A.,
1356 and Roederer, M. (2006). Amine reactive dyes: an effective tool to discriminate live and dead
1357 cells in polychromatic flow cytometry. *J. Immunol. Methods* 313, 199–208.

1358

1359 Petrovas, C., Yamamoto, T., Gerner, M.Y., Boswell, K.L., Wloka, K., Smith, E.C., Ambrozak,
1360 D.R., Sandler, N.G., Timmer, K.J., Sun, X., et al. (2012). CD4 T follicular helper cell dynamics
1361 during SIV infection. *J. Clin. Invest.* 122, 3281–3294.

1362

1363 Qiao, X., He, B., Chiu, A., Knowles, D.M., Chadburn, A., and Cerutti, A. (2006). Human
1364 immunodeficiency virus 1 Nef suppresses CD40-dependent immunoglobulin class switching
1365 in bystander B cells. *Nat. Immunol.* 7, 302–310.

1366

1367 Querec, T.D., Akondy, R.S., Lee, E.K., Cao, W., Nakaya, H.I., Teuwen, D., Pirani, A., Gernert,
1368 K., Deng, J., Marzolf, B., et al. (2009). Systems biology approach predicts immunogenicity of
1369 the yellow fever vaccine in humans. *Nat. Immunol.* 10, 116–125.

1370

1371 Ray, J.P., Staron, M.M., Shyer, J.A., Ho, P.C., Marshall, H.D., Gray, S.M., Laidlaw, B.J., Araki,
1372 K., Ahmed, R., Kaech, S.M., et al. (2015). The interleukin-2-mTORc1 kinase axis defines the
1373 signaling, differentiation, and metabolism of T helper 1 and follicular B helper T cells. *Immunity*
1374 43, 690–702.

1375

1376 Recher, M., Lang, K.S., Hunziker, L., Freigang, S., Eschli, B., Harris, N.L., Navarini, A., Senn,
1377 B.M., Fink, K., Lötscher, M., et al. (2004). Deliberate removal of T cell help improves virus-
1378 neutralizing antibody production. *Nat. Immunol.* 5, 934–942.

1379

1380 Recher, M., Lang, K.S., Navarini, A., Hunziker, L., Lang, P.A., Fink, K., Freigang, S., Georgiev,
1381 P., Hangartner, L., Zellweger, R., et al. (2007). Extralymphatic virus sanctuaries as a
1382 consequence of potent T-cell activation. *Nat. Med.* 13, 1316–1323.

1383

1384 Reuschl, A.K., Mesner, D., Shivkumar, M., Whelan, M.V.X., Pallett, L.J., Guerra-Assunção,
1385 J.A., Madansein, R., Dullabh, K.J., Sigal, A., Thornhill, J.P., et al. (2022). HIV-1 Vpr drives a

1386 tissue residency-like phenotype during selective infection of resting memory T cells. *Cell Rep.*
1387 39, 110650.
1388
1389 Rickles, R.J., Botfield, M.C., Weng, Z., Taylor, J.A., Green, O.M., Brugge, J.S., and Zoller, M.J.
1390 (1994). Identification of Src, Fyn, Lyn, PI3K and Abl SH3 domain ligands using phage display
1391 libraries. *EMBO J.* 13, 5598–5604.
1392
1393 Samer, S., Chowdhury, A., Wiche Salinas, T.R., Estrada, P.M.D.R., Reuter, M., Tharp, G.,
1394 Bosinger, S., Cervasi, B., Auger, J., Gill, K., et al. (2023). Lymph-Node-based $CD3^+$ $CD20^+$
1395 cells emerge from membrane exchange between T follicular helper cells and B cells and
1396 increase their frequency following simian immunodeficiency virus infection. *J. Virol.* 97,
1397 e0176022.
1398
1399 Sammicheli, S., Kuka, M., Di Lucia, P., de Oya, N.J., De Giovanni, M., Fioravanti, J., Cristofani,
1400 C., Maganuco, C.G., Fallet, B., Ganzer, L., et al. (2016). Inflammatory monocytes hinder
1401 antiviral B cell responses. *Sci. Immunol.* 1, pii: eaah6789.
1402
1403 Sander, S., Chu, V.T., Yasuda, T., Franklin, A., Graf, R., Calado, D.P., Li, S., Imami, K., Selbach,
1404 M., Di Virgilio, M., et al. (2015). PI3 kinase and FOXO1 transcription factor activity differentially
1405 control B cells in the germinal center light and dark zones. *Immunity* 43, 1075–1086.
1406
1407 Sarbassov, D.D., Guertin, D.A., Ali, S.M., and Sabatini, D.M. (2005) Phosphorylation and
1408 regulation of Akt/PKB by the rictor-mTOR complex. *Science* 307, 1098–1101.
1409
1410 Schindler, M., Münch, J., Brenner, M., Stahl-Hennig, C., Skowronski, J., and Kirchhoff, F.
1411 (2004). Comprehensive analysis of nef functions selected in simian immunodeficiency virus-
1412 infected macaques. *J. Virol.* 78, 10588–10597.
1413

1414 Schindler, M., Münch, J., Kutsch, O., Li, H., Santiago, M.L., Bibollet-Ruche, F., Müller-Trutwin,
1415 M.C., Novembre, F.J., Peeters, M., Courgnaud, V., et al. (2006). Nef-mediated suppression of
1416 T cell activation was lost in a lentiviral lineage that gave rise to HIV-1. *Cell* 125, 1055–1067.
1417
1418 Sette, A., Sidney, J., Southwood, S., Moore, C., Berry, J., Dow, C., Bradley, K., Hoof, I., Lewis,
1419 M.G., Hildebrand, W.H., et al. (2012). A shared MHC supertype motif emerges by convergent
1420 evolution in macaques and mice, but is totally absent in human MHC molecules.
1421 *Immunogenetics* 64, 421–434.
1422
1423 Sheehy, A.M., Gaddis, N.C., Choi, J.D., and Malim, M.H. (2002). Isolation of a human gene
1424 that inhibits HIV-1 infection and is suppressed by the viral Vif protein. *Nature* (2002) 418, 646–
1425 650.
1426
1427 Shi, S., Seki, S., Matano, T., and Yamamoto, H. (2013). IL-21-producer $CD4^+$ T cell kinetics
1428 during primary simian immunodeficiency virus infection. *Microbes Infect.* 15, 697–707.
1429
1430 Shulman, Z., Gitlin, A.D., Weinstein, J.S., Lainez, B., Esplugues, E., Flavell, R.A., Craft, J.E.,
1431 and Nussenzweig, M.C. (2014). Dynamic signaling by T follicular helper cells during germinal
1432 center B cell selection. *Science* 345, 1058–1062.
1433
1434 Silveira, E.L., Kasturi, S.P., Kovalenkov, Y., Rasheed, A.U., Yeiser, P., Jinnah, Z.S., Legere,
1435 T.H., Pulendran, B., Villinger, F., and Wrammert, J. (2015). Vaccine-induced plasmablast
1436 responses in rhesus macaques: phenotypic characterization and a source for generating
1437 antigen-specific monoclonal antibodies. *J. Immunol. Methods* 416, 69–83.
1438
1439 Sommerstein, R., Flatz, L., Remy, M.M., Malinge, P., Magistrelli, G., Fischer, N., Sahin, M.,
1440 Bergthaler, A., Igonet, S., Ter Meulen, J., et al. (2015). Arenavirus glycan shield promotes
1441 neutralizing antibody evasion and protracted infection. *PLoS Pathog.* 11, e1005276.

1442

1443 Srinivasan, L., Sasaki, Y., Calado, D.P., Zhang, B., Paik, J.H., DePinho, R.A., Kutok, J.L.,
1444 Kearney, J.F., Otipoby, K.L., and Rajewsky, K. (2009). PI3 kinase signals BCR-dependent
1445 mature B cell survival. *Cell* 139, 573–586.

1446

1447 Stolp, B., Reichman-Fried, M., Abraham, L., Pan, X., Giese, S.I., Hannemann, S., Goulimari,
1448 P., Raz, E., Grosse, R., and Fackler, O.T. (2009). HIV-1 Nef interferes with host cell motility by
1449 deregulation of Cofilin. *Cell Host Microbe* 6, 174–186.

1450

1451 Stolp, B., Imle, A., Coelho, F.M., Hons, M., Gorina, R., Lyck, R., Stein, J.V., and Fackler, O.T.
1452 (2012). HIV-1 Nef interferes with T-lymphocyte circulation through confined environments in
1453 vivo. *Proc. Natl. Acad. Sci. USA* 109, 18541–18546.

1454

1455 Swingler, S., Zhou, J., Swingler, C., Dauphin, A., Greenough, T., Jolicoeur, P., and Stevenson,
1456 M. (2008). Evidence for a pathogenic determinant in HIV-1 Nef involved in B cell dysfunction
1457 in HIV/AIDS. *Cell Host Microbe* 4, 63–76.

1458

1459 Takahashi, N., Nomura, T., Takahara, Y., Yamamoto, H., Shiino, T., Takeda, A., Inoue, M., Iida,
1460 A., Hara,H., Shu, T., et al. (2013). A novel protective MHC-I haplotype not associated with
1461 dominant Gag-specific $CD8^+$ T-cell responses in SIV_{mac239} infection of Burmese rhesus
1462 macaques. *PLoS ONE* 8, e54300.

1463

1464 Terahara, K., Ishii, H., Nomura, T., Takahashi, N., Takeda, A., Shiino, T., Tsunetsugu-Yokota,
1465 Y., and Matano, T. (2014). Vaccine-induced $CD107a^+$ $CD4^+$ T cells are resistant to depletion
1466 following AIDS virus infection. *J. Virol.* 88, 14232–14240.

1467

1468 Tomaras, G.D., Yates, N.L., Liu, P., Qin, L., Fouda, G.G., Chavez, L.L., Decamp, A.C., Parks,
1469 R.J., Ashley, V.C., Lucas, J.T., et al. (2008). Initial B-cell responses to transmitted human

1470 immunodeficiency virus type 1: virion-binding immunoglobulin M (IgM) and IgG antibodies
1471 followed by plasma anti-gp41 antibodies with ineffective control of initial viremia. *J. Virol.* 82,
1472 12449–12463.
1473
1474 Volcic, M., Sparrer, K.M.J., Koepke, L., Hotter, D., Sauter, D., Stürzel, C.M., Scherer, M.,
1475 Stamminger, T., Hofmann, T.G., Arhel, N.J., et al. (2020). Vpu modulates DNA repair to
1476 suppress innate sensing and hyper-integration of HIV-1. *Nat. Microbiol.* 5, 1247–1261.
1477
1478 Wang, J., Sohn, H., Sun, G., Milner, J.D. and Pierce, S.K. (2014). The autoinhibitory C-terminal
1479 SH2 domain of phospholipase C-γ2 stabilizes B cell receptor signalosome assembly. *Sci.*
1480 *Signal.* 7, ra89.
1481
1482 Whitney, J.B., Hill, A.L., Sanisetty, S., Penaloza-MacMaster, P., Liu, J., Shetty, M., Parenteau,
1483 L., Cabral, C., Shields, J., Blackmore, S., et al. (2014). Rapid seeding of the viral reservoir
1484 prior to SIV viraemia in rhesus monkeys. *Nature* 512, 74–77.
1485
1486 Wülfing, C., Sjaastad, M.D., and Davis, M.M. (1998). Visualizing the dynamics of T cell
1487 activation: intracellular adhesion molecule 1 migrates rapidly to the T cell/B cell interface and
1488 acts to sustain calcium levels. *Proc. Natl. Acad. Sci. USA* 95, 6302–6307.
1489
1490 Xu, H., Wang, X., Malam, N., Aye, P.P., Alvarez, X., Lackner, A.A., and Veazey, R.S. (2015).
1491 Persistent simian immunodeficiency virus infection drives differentiation, aberrant
1492 accumulation, and latent infection of germinal center follicular T helper cells. *J. Virol.* 90,1578–
1493 1587.
1494
1495 Xu, W., Santini, P.A., Sullivan, J.S., He, B., Shan, M., Ball, S.C., Dyer, W.B., Ketas, T.J.,
1496 Chadburn, A., Cohen-Gould, L., et al. (2009). HIV-1 evades virus-specific IgG2 and IgA

1497 responses by targeting systemic and intestinal B cells via long-range intercellular conduits.
1498 *Nat. Immunol.* 10, 1008–1017.
1499
1500 Yamada, E., Nakaoka, S., Klein, L., Reith, E., Langer, S., Hopfensperger, K., Iwami, S.,
1501 Schreiber, G., Kirchhoff, F., Koyanagi, Y., et al. (2018) Human-specific adaptations in Vpu
1502 conferring anti-tetherin activity are critical for efficient early HIV-1 replication in vivo. *Cell Host*
1503 *Microbe* 23, 110–120.e7.
1504
1505 Yamamoto, H., Kawada, M., Takeda, A., Igarashi, H. and Matano, T. (2007). Post-infection
1506 immunodeficiency virus control by neutralizing antibodies. *PLoS ONE 2*, e540.
1507
1508 Yan, J., Shun, M.C., Zhang, Y., Hao, C., and Skowronski, J. (2019). HIV-1 Vpr counteracts
1509 HLTF-mediated restriction of HIV-1 infection in T cells. *Proc. Natl. Acad. Sci. USA.* 116, 9568–
1510 9577.
1511
1512 Zhang, F., Wilson, S.J., Landford, W.C., Virgen, B., Gregory, D., Johnson, M.C., Munch, J.,
1513 Kirchhoff, F., Bieniasz, P.D., and Hatziioannou, T. (2009). Nef proteins from simian
1514 immunodeficiency viruses are tetherin antagonists. *Cell Host Microbe 6*, 54–67.
1515
1516 Zotos, D., Coquet, J.M., Zhang, Y., Light, A., D'Costa, K., Kallies, A., Corcoran, L.M., Godfrey,
1517 D.I., Toellner, K.M., Smyth, M.J., et al. (2010). IL-21 regulates germinal center B cell
1518 differentiation and proliferation through a B cell-intrinsic mechanism. *J. Exp. Med.* 207, 365–
1519 378.
1520

1521 **Supplemental Information Legends**

1522

1523 **Fig. 1-Supplement 1. Profile of SIV_{mac239}-NAb non-inducer subgroup cohort.**

1524 Summary of a SIV_{mac239}-NAb non-inducer subgroup cohort (*n* = 19), composed from previously
1525 partially characterized, MHC class I haplotype-balanced naïve animals. Symbols A+, B+, E+,
1526 J+ and D+ represent possession of MHC-I haplotypes *90-120-Ia*, *90-120-Ib*, *90-010-Ie*, *90-*
1527 *088-Ij* and *90-010-Id*, respectively. For the titers, - represents negative; +/- represents
1528 neutralization in three out of four wells in a quadruplicate test. Gray shadings indicate
1529 euthanasia due to AIDS progression. Mamu-A and Mamu-B alleles of interest in this study are
1530 listed. These NAb non-inducers were previously partially reported for their plasma viral loads
1531 and MHC-I alleles (Nomura et al., 2012; Takahashi et al., 2013; Nakane et al., 2013; Iwamoto
1532 et al., 2014). R01-011 was previously partially reported for NAb titers measured with the same
1533 method using MT4 cells as targets (Kawada et al., 2007), which derived comparable results.

1534

1535 **Fig. 1-Supplement 2. IgG class-switched NAbs in the inducers.**

1536 Titration of SIV_{mac239}-neutralizing IgGs in the NAb inducers. SIV_{mac239}-specific IgGs, purified
1537 from pools of plasma with SIV_{mac239}-specific NAb titers, were obtained from each animal as
1538 described (Yamamoto et al., 2007) and examined for their neutralizing activity by 10 $TCID_{50}$
1539 SIV_{mac239} killing on MT4-R5 cells. NAb-negative anti-SIV IgG and control IgG were prepared
1540 from a representative animal (R01-011) with NAb-negative plasma and pooled plasma of
1541 uninfected rhesus macaques, respectively.

1542

1543 **Fig.1-Supplement 3. Anti-SIV binding IgG profiles in NAb inducers and non-inducers.**

1544 **(A)** Temporal changes in SIV_{mac251} Env gp120-specific antibody titers in the NAb non-inducers
1545 without rapid progression [NAb-negative non-rapid progressors, NAb(-) non-RPs] (left, *n* = 11)
1546 and NAb inducers [NAb(+)] (right, *n* = 9). NAb non-inducers showing rapid progression
1547 (euthanized with AIDS onset within approximately 1 year) were not included except for
1548 macaque R10-001 (shown in the left for aligned comparison). Samples for non-RPs R06-001

1549 and R10-002 were unavailable.

1550 **(B)** Unpaired t test of log-transformed anti-SIV Env Ab titers in NAb(-) non-RPs and NAb
1551 inducers. Bars represent geometric mean absorbance within each group.

1552 **(C)** Lysed SIV_{mac} virion linear antigen-binding at year 1 p.i. in NAb(-) non-RPs (left, *n* = 12)
1553 and NAb inducers (right, *n* = 9). Plasma anti-SIV_{mac251} IgGs were detected using a commercial
1554 western blotting system against the parental strain SIV_{mac251} (ZeptoMetrix). White arrowheads
1555 indicate Env gp120-specific bands. Experiments were performed twice with comparable
1556 results.

1557

1558 **Fig. 1-Supplement 4. Env sequence variation pattern is not a major characteristic of**
1559 **NAb induction.**

1560 SIV_{mac239} Env sequence variations before and after NAb induction. For each animal, the upper
1561 time point shows pre-induction and the lower time point (in purple) shows post-induction (first
1562 or second time point with NAb titer > 1:2). Dominant residue changes are shown as follows:
1563 gp120 (gray), variable regions V1-V5 (blue), and gp41 (blue gray). Subdominant mutations
1564 are uncolored. Unlabeled gray and black shadings show subdominant and dominant deletion
1565 of residues. Parental SIV_{mac239} sequence is listed for V1-V5. Residues mutated in multiple
1566 animals within V1-V5 are shown in red.

1567

1568 **Fig. 3-Supplement 1. Selection of Nef-G63E mutant SIV is linked with Nef_{62-70}-specific**
1569 **$CD8^+$ T-cell response positivity.**

1570 **(A)** Nef_{62-70}-specific CD8+ T-cell responses around week 20 post-SIV challenge in seven
1571 viremic NAb non-inducers possessing either of the MHC-I alleles Mamu-B*039:01, Mamu-
1572 B*004:01 or Mamu-A1*032:02.

1573 **(B)** Temporal supernatant SIV p27 concentrations after wild type (WT) or Nef-G63E mutant
1574 SIV infection at multiplicity of infection (MOI) 0.001 on HSC-F cells. Data represent one of two
1575 independent experiments performed in triplicate. Bars: mean ± SEM.

1576 **(C)** Comparison of plasma viral loads in Nef-G63E-selecting NAb non-inducers (*n* = 7) versus

1577 non-inducers at indicated time points post-SIV challenge. Bars represent geometric means.
1578 log10-transformed values are compared by unpaired t tests.
1579
1580 **Fig. 4-Supplement 1. Decreased Akt hyperactivation properties of Nef-G63E mutant SIV.**
1581 **(A)** Plasma ferritin levels (ng/ml) in examined NAb non-inducers versus Nef-G63E mutant SIV-
1582 selecting NAb inducers around year 1 post-infection. Bars represent mean in each group. Log-
1583 transformed values compared by unpaired t test.
1584 **(B)** Relative levels of pAkt Ser473 (left panel) and threonine (Thr) 308 (right panel) in SIV Nef^+
1585 HSR5.4 cells (MOI 0.1, 4 days p.i.).
1586 **(C)** Relative pAkt Ser473 levels in Nef^+ HSC-F cells without stimuli and transiently pulsed with
1587 IFN-γ, IL-2 or SIV_{mac} Env gp130 after infection (MOI 0.2, 1 day).
1588 **(D)** Gene expression significantly differing between WT and Nef-G63E SIV infection (MOI 5,
1589 1 day). Black bars show potentially Akt-related genes. Asterisks show dynamics concordant
1590 with the Nef-G63E phenotype (PI3K-pAkt Ser473 downstream downregulation or inhibition
1591 upregulation).
1592 **(E)** Representative flow cytometric gating (NAb inducer R01-012, wk 30 p.i.) of peripheral
1593 blood $CXCR3^-CXCR5^+PD\text{-}1^+$ memory follicular CD4+ T cells. Cells were gated as $CD3^+CD8^-$
1594 $CD4^+CD95^+CXCR5^+PD\text{-}1^+CXCR3^-$ live singlet PBMCs. Available samples of six NAb inducers
1595 showing peak Nef-G63E mutant selection around week 30 p.i. and thirteen viremic NAb non-
1596 inducers were tracked.
1597 **(F)** Comparison of peripheral $CXCR3^-CXCR5^+PD\text{-}1^+$ memory Tfh cell frequencies between
1598 pre-SIV infection and around week 30 post-infection in examined NAb non-inducers
1599 developing disease before week 60 (left: n = 5) and alive more than 70 weeks (middle: n = 8)
1600 and Nef-G63E-detected NAb inducers alive more than 70 weeks (right: n = 6). Analyzed by
1601 Wilcoxon signed-rank tests.
1602 MFIs relative to those in uninfected controls (%) are shown. **: $P < 0.01$, ***: $P < 0.001$, n.s.:
1603 not significant between WT and Nef-G63E mutant by unpaired t tests (B-C). Data represent
1604 one of two (B, C) independent experiments performed in triplicate (C: unstimulated) or

1605 quadruplicate (B, C: PI3K-pulsed). Bars: mean ± SEM.

1606

1607 **Fig. 4-Supplement 2. Nef-G63R mutant SIV properties.**

1608 **(A)** Comparison of frequencies of macaques selecting for Nef-G63R mutant in plasma
1609 between NAb non-inducers and inducers. Compared by Fisher's exact test.

1610 **(B)** Temporal relationship of Nef G63R frequencies in plasma virus in a NAb non-inducer
1611 macaque R06-034 preferentially selecting for Nef-G63R but not Nef-G63E mutant. Black
1612 boxes (left Y axis) show $\log_2$ NAb titers; red triangles and blue diamonds (right Y axis) show
1613 percentage of G63E and G63R mutations detected by subcloning (15 clones/point on average),
1614 respectively.

1615 **(C)** Left: representative histograms of relative pAkt serine (Ser) 473 levels in $p27^+$
1616 subpopulations after WT, Nef-G63E or Nef-G63R mutant SIV infection at MOI 0.1 on HSC-F
1617 cells. Numbers show pAkt Ser473 mean fluorescence intensities (MFIs) for each. Right:
1618 Deviation of pAkt Ser473 MFIs in $p27^+$ HSC-F cells compared with mean MFI of uninfected
1619 cells. Analyzed by one-way ANOVA with Tukey's post-hoc multiple comparison tests. Data
1620 represent one of two independent experiments performed in quadruplicate with similar results.

1621

1622 **Fig. 5-Supplement 1. Machine learning-verified morphological gating of Nef-invaded B**
1623 **cells *in vivo*.**

1624 **(A)** Representative gating strategy plus schematic of inguinal lymph node Nef^+CD19^+ B cells
1625 of an SIV_{mac239}-infected rhesus macaque analyzed by ImageStreamX MK II imaging flow
1626 cytometry (R10-012, week 160 p.i.). First-step incorporation of Live/Dead staining gates out
1627 $CD19^+$ B cells staining positive for Nef potentially due to pre-experimental membrane
1628 permeation (e.g., image #246896, #248952 and #71859). Second-step dual gating for
1629 intracellular Nef signal pixel Haralick variance mean (H Variance mean, X axis), a textural
1630 feature calculated from a gray level co-occurrence matrix (GLCM) for each image representing
1631 adjacent pixel signal strength heterogeneity and Nef signal intensity threshold (Y axis) gates
1632 out $CD19^+$ B cells showing potentially non-specific, strong intracellular binary clustered

1633 staining pixels for Nef deriving a large variance (X axis), and/or cells stained overtly strong for
1634 Nef and hence becoming void for feasible image verification (high threshold) (Y axis), both
1635 likely originating stochastically from post-experimental rupturing procedures including
1636 membrane permeation (e.g. image #18541). This two-step noise cancellation results in
1637 acquisition of a Live/Dead^{-}-Nef signal Haralick variance mean^{lo}-Nef signal intensity threshold^{lo}-
1638 Nef^{+}CD19^{+} B-cell population (e.g. image #116318, #116250 and #132927) with a pericellular
1639 Nef^{int-lo} staining, biologically concordant with Nef membrane anchoring, resembling Nef^{+} cells
1640 experimentally generated *in vitro* and showed the highest score in IDEAS6.3 machine learning
1641 module scoring for segregation of typical void vs. valid images (upper right). This gating was
1642 implemented for counting and analysis of Env-specific B-cell Nef invasion *in vivo* (**Figure 5**).
1643 **(B)** Detection of contact-dependent Nef invasion from SIV-infected HSC-F CD4^{+} T cells to
1644 cocultured Ramos B cells *in vitro*. One typical image of an intercellular conduit (SSC, purple)
1645 with Nef (green) protrusions from infected HSC-F cells to CD19^{+} (red) Ramos B cells from two
1646 independent experiments are shown.
1647
1648 **Fig. 7-Supplement 1. Full gating strategy of SIV$_{mac239}$ Env gp140-specific B-cell**
1649 **responses.**
1650 Full gating (R02-004, week 32 p.i.) of SIV Env gp140-specific memory B cells (B_{mem}) and
1651 plasmablasts (PBs) shown in **Figure 7**.

Figure 1

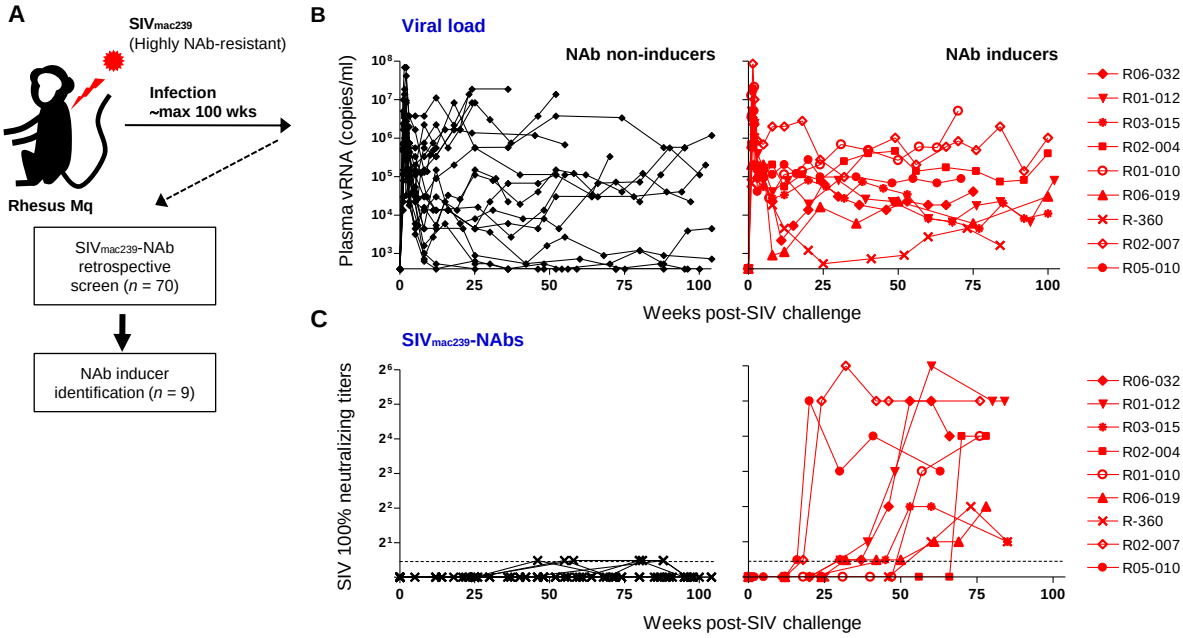
A
SIVmac239
(Highly NAb-resistant)
Infection
~max 100 wks
Rhesus Mq
SIVmac239-NAb
retrospective
screen (n = 70)
NAb inducer
identification (n = 9)
B
Viral load
NAb non-inducers
NAb inducers
Plasma vRNA (copies/ml)
Weeks post-SIV challenge
R06-032
R01-012
R03-015
R02-004
R01-010
R06-019
R-360
R02-007
R05-010
C
SIVmac239-NAbs
SIV 100% neutralizing titers
Weeks post-SIV challenge

Figure 2

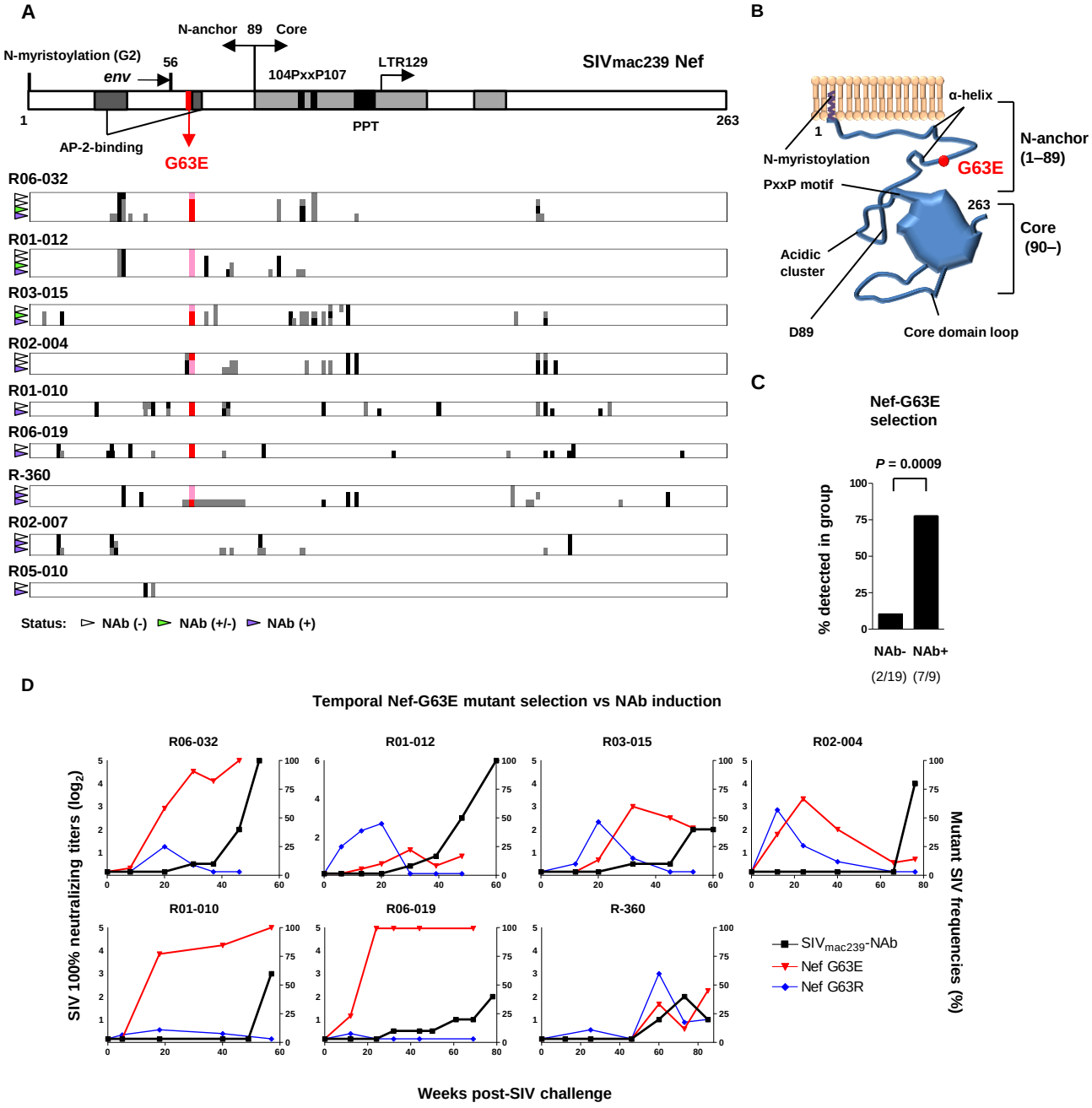
A
N-anchor 89 Core
N-myristoylation (G2)
56
env
104PxxP107
LTR129
SIVmac239 Nef
1
263
PPT
AP-2-binding
G63E
R06-032
R01-012
R03-015
R02-004
R01-010
R06-019
R-360
R02-007
R05-010
Status: NAb (-) NAb (+/-) NAb (+)
B
α-helix
N-anchor (1–89)
1
N-myristoylation
G63E
PxxP motif
263
Core (90–)
Acidic cluster
D89
Core domain loop
C
Nef-G63E selection
P = 0.0009
% detected in group
NAb- NAb+
(2/19) (7/9)
D
Temporal Nef-G63E mutant selection vs NAb induction
R06-032
R01-012
R03-015
R02-004
R01-010
R06-019
R-360
SIV 100% neutralizing titers (log2)
Mutant SIV frequencies (%)
SIVmac239-NAb
Nef G63E
Nef G63R
Weeks post-SIV challenge

Figure 3

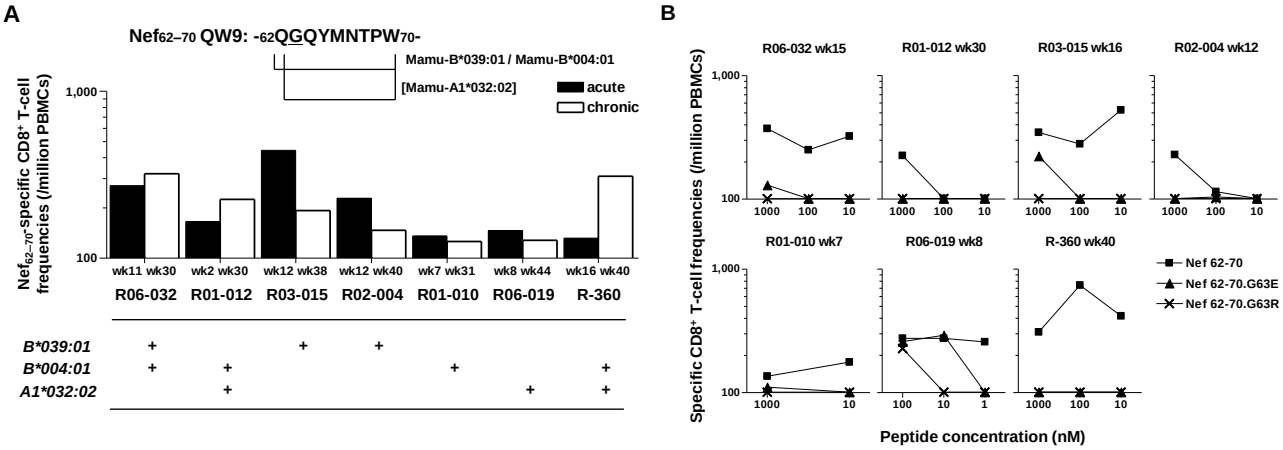
A
Nef62–70 QW9: -62QGQYMNTPW70-
Mamu-B*039:01 / Mamu-B*004:01
[Mamu-A1*032:02]
acute
chronic
Nef62–70-specific CD8+ T-cell frequencies (/million PBMCs)
1,000
100
wk11 wk30
wk2 wk30
wk12 wk38
wk12 wk40
wk7 wk31
wk8 wk44
wk16 wk40
R06-032
R01-012
R03-015
R02-004
R01-010
R06-019
R-360
B*039:01
B*004:01
A1*032:02
B
R06-032 wk15
R01-012 wk30
R03-015 wk16
R02-004 wk12
R01-010 wk7
R06-019 wk8
R-360 wk40
Nef 62-70
Nef 62-70.G63E
Nef 62-70.G63R
Specific CD8+ T-cell frequencies (/million PBMCs)
1000
100
10
1
Peptide concentration (nM)

Figure 4

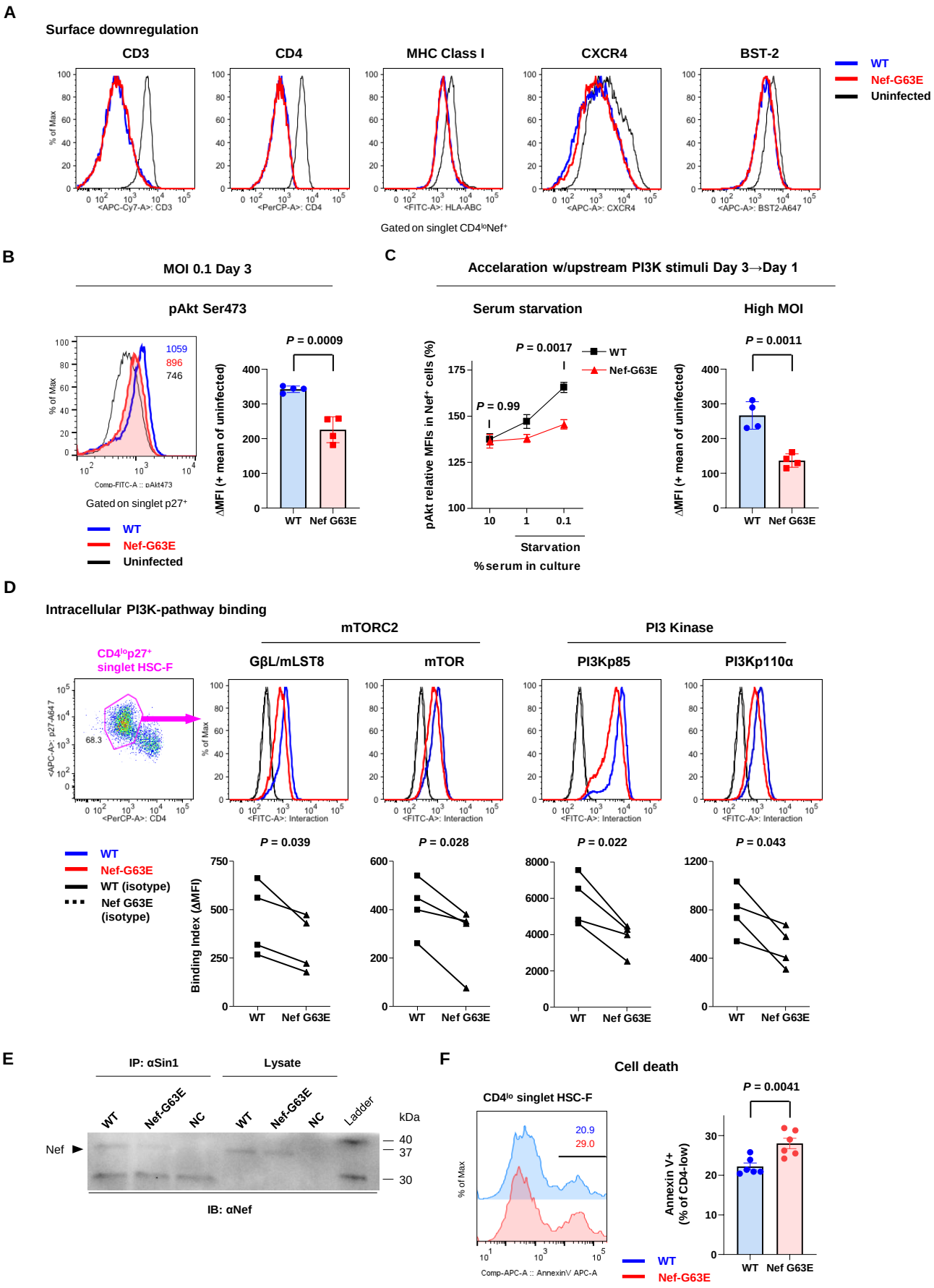
A
Surface downregulation
CD3
CD4
MHC Class I
CXCR4
BST-2
WT
Nef-G63E
Uninfected
% of Max
<APC-Cy7-A>: CD3
<PerCP-A>: CD4
<FITC-A>: HLA-ABC
<APC-A>: CXCR4
<APC-A>: BST2-A647
Gated on singlet CD4loNef+
B
MOI 0.1 Day 3
pAkt Ser473
1059
896
746
Comp-FITC-A :: pAkt473
Gated on singlet p27+
WT
Nef-G63E
Uninfected
P = 0.0009
ΔMFI (+ mean of uninfected)
WT
Nef G63E
C
Accelaration w/upstream PI3K stimuli Day 3→Day 1
Serum starvation
High MOI
P = 0.0017
P = 0.99
pAkt relative MFIs in Nef+ cells (%)
Starvation
% serum in culture
P = 0.0011
D
Intracellular PI3K-pathway binding
mTORC2
PI3 Kinase
CD4lop27+
singlet HSC-F
68.3
<APC-A>: p27-A647
<PerCP-A>: CD4
GβL/mLST8
mTOR
PI3Kp85
PI3Kp110α
<FITC-A>: Interaction
WT (isotype)
Nef G63E (isotype)
P = 0.039
P = 0.028
P = 0.022
P = 0.043
Binding Index (ΔMFI)
E
IP: αSin1
Lysate
Ladder
kDa
Nef
40
37
30
IB: αNef
F
Cell death
CD4lo singlet HSC-F
20.9
29.0
Comp-APC-A :: AnnexinV APC-A
P = 0.0041
Annexin V+ (% of CD4-low)

Figure 5

A

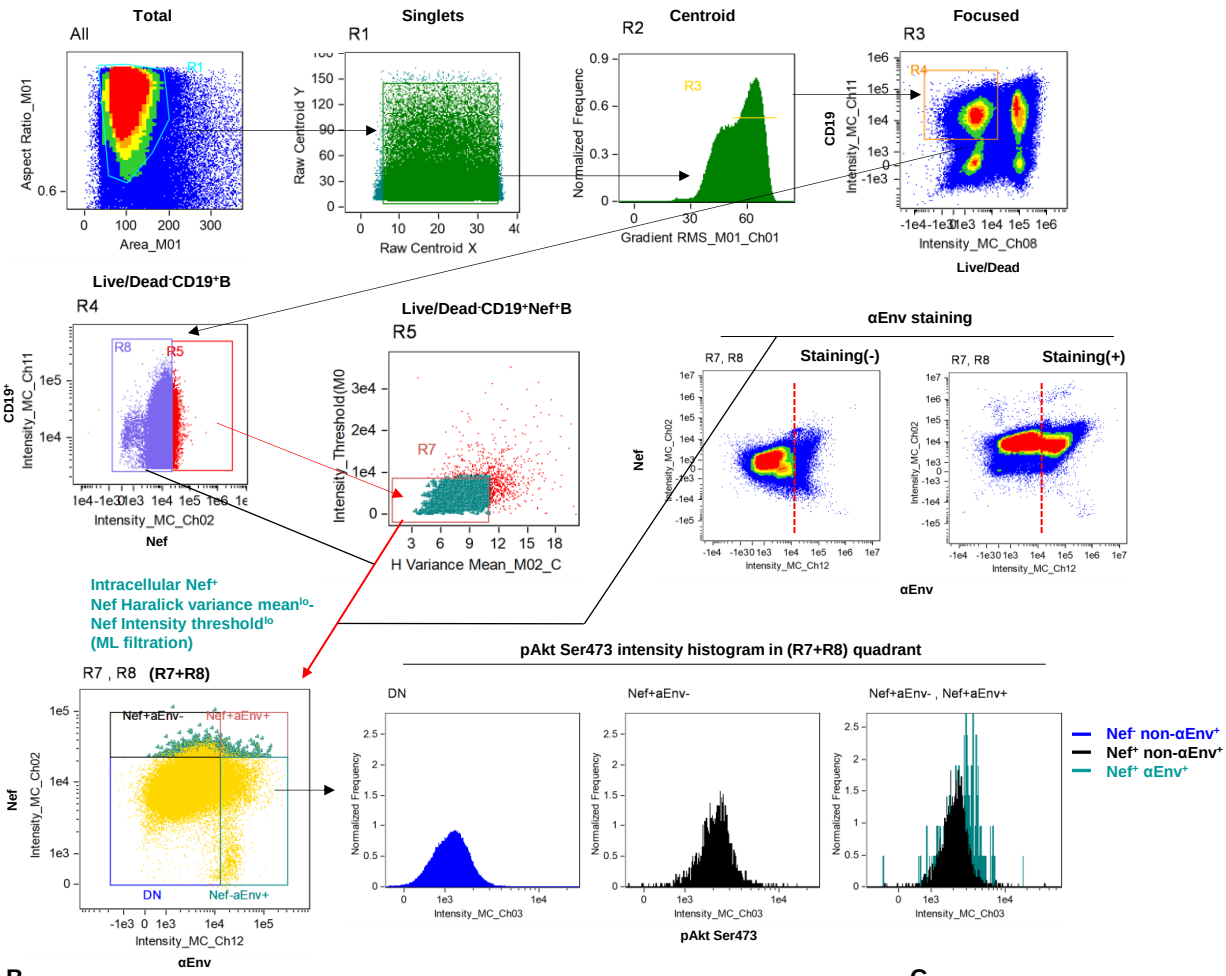

B

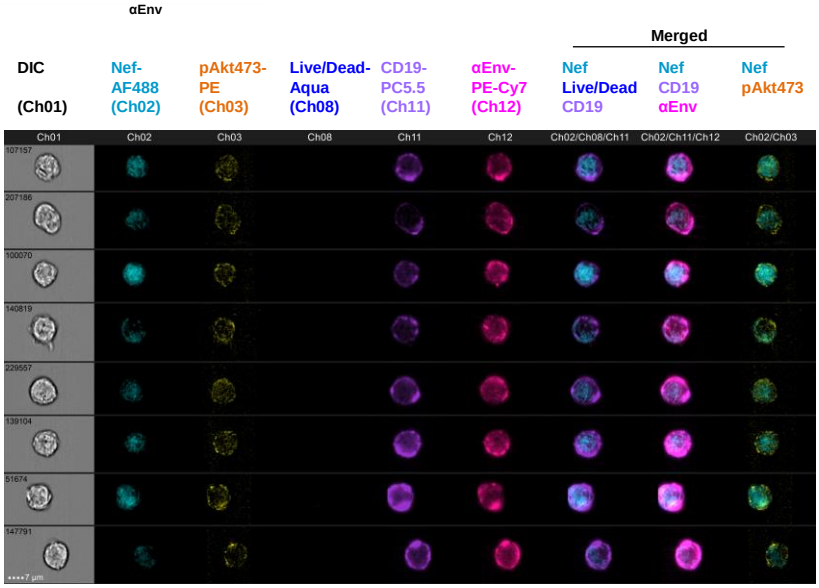

C

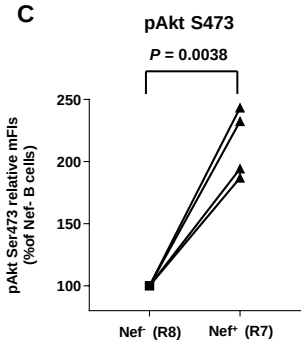

D

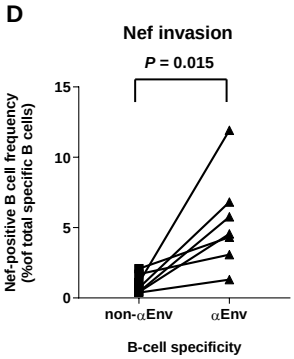

Figure 6

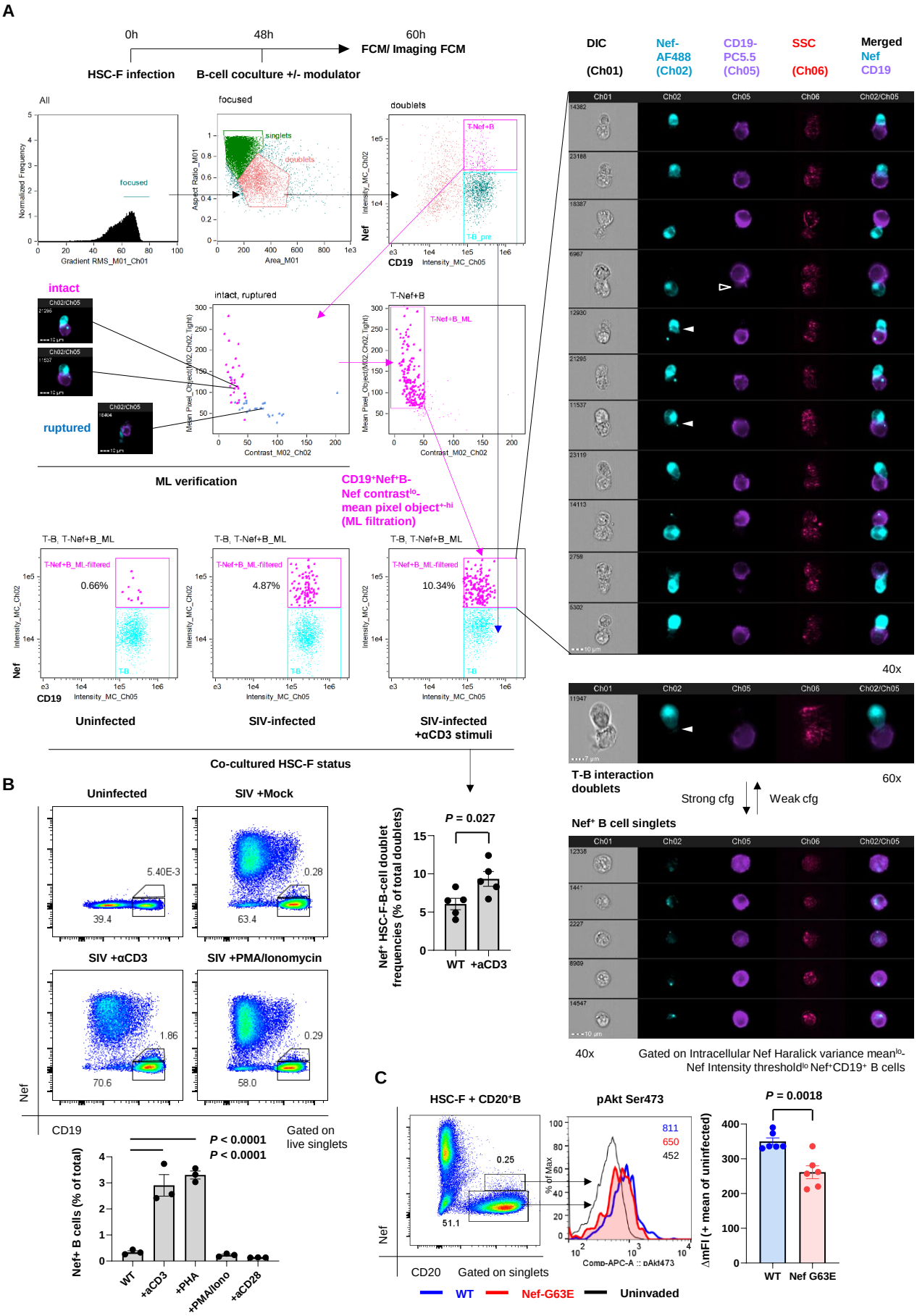
A
0h
48h
60h
FCM/ Imaging FCM
HSC-F infection
B-cell coculture +/- modulator
All
focused
doublets
singlets
Normalized Frequency
Gradient RMS_M01_Ch01
Aspect Ratio_M01
Area_M01
Nef
CD19
Intensity_MC_Ch05
Intensity_MC_Ch02
T-Nef+B
T-B_pre
intact
ruptured
intact, ruptured
T-Nef+B
T-Nef+B_ML
Mean Pixel_Object(M02 Ch02, Tight)
Contrast_M02_Ch02
ML verification
CD19+Nef+B-
Nef contrastlo-
mean pixel object+-hi
(ML filtration)
T-B, T-Nef+B_ML
T-Nef+B_ML-filtered
T-B
0.66%
4.87%
10.34%
Uninfected
SIV-infected
SIV-infected
+αCD3 stimuli
Co-cultured HSC-F status
DIC
(Ch01)
Nef-
AF488
(Ch02)
CD19-
PC5.5
(Ch05)
SSC
(Ch06)
Merged
Nef
CD19
Ch01
Ch02
Ch05
Ch06
Ch02/Ch05
40x
T-B interaction
doublets
60x
Strong cfg
Weak cfg
Nef+ B cell singlets
40x
Gated on Intracellular Nef Haralick variance meanlo-
Nef Intensity thresholdlo Nef+CD19+ B cells
B
Uninfected
SIV +Mock
SIV +αCD3
SIV +PMA/Ionomycin
5.40E-3
39.4
0.28
63.4
1.86
70.6
0.29
58.0
Nef
CD19
Gated on
live singlets
P = 0.027
Nef+ HSC-F-B-cell doublet
frequencies (% of total doublets)
WT
+αCD3
P < 0.0001
P < 0.0001
Nef+ B cells (% of total)
WT
+αCD3
+PHA
+PMA/Iono
+αCD28
C
HSC-F + CD20+B
pAkt Ser473
0.25
51.1
811
650
452
% of Max
Comp-APC-A :: pAkt473
CD20
Gated on singlets
P = 0.0018
ΔmFI (+ mean of uninfected)
WT
Nef G63E
WT
Nef-G63E
Uninvaded

Figure 7

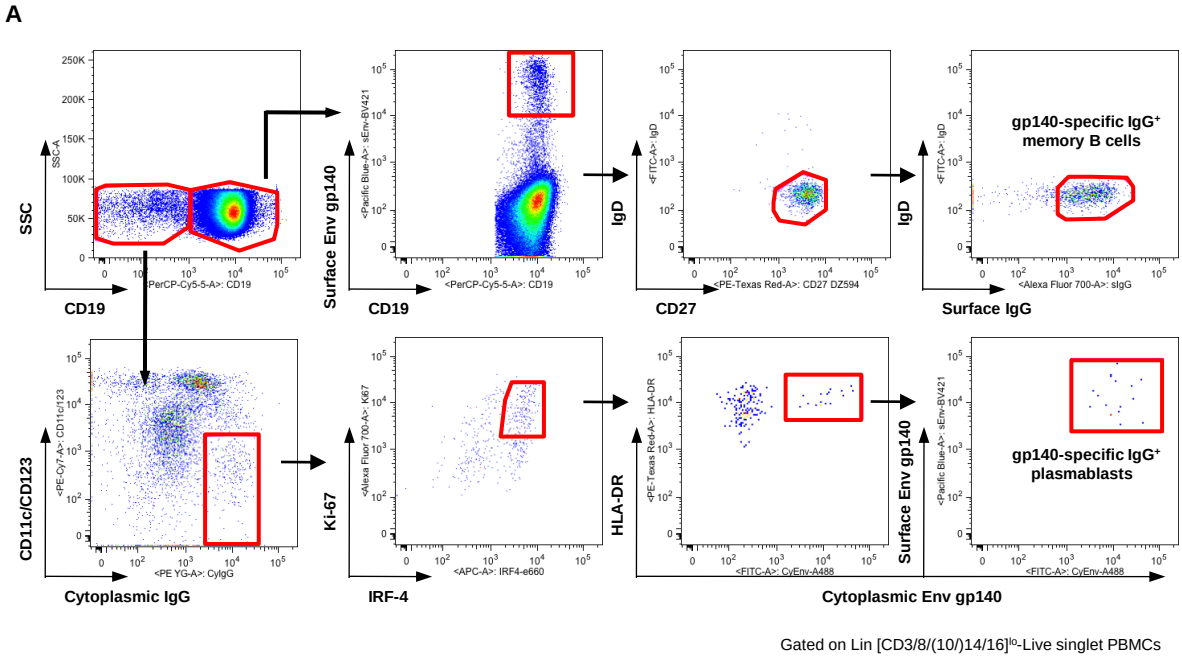
A
SSC
CD19
Surface Env gp140
CD19
IgD
CD27
IgD
Surface IgG
gp140-specific IgG+ memory B cells
CD11c/CD123
Cytoplasmic IgG
Ki-67
IRF-4
HLA-DR
Surface Env gp140
Cytoplasmic Env gp140
gp140-specific IgG+ plasmablasts
Gated on Lin [CD3/8/(10)/14/16]lo-Live singlet PBMCs

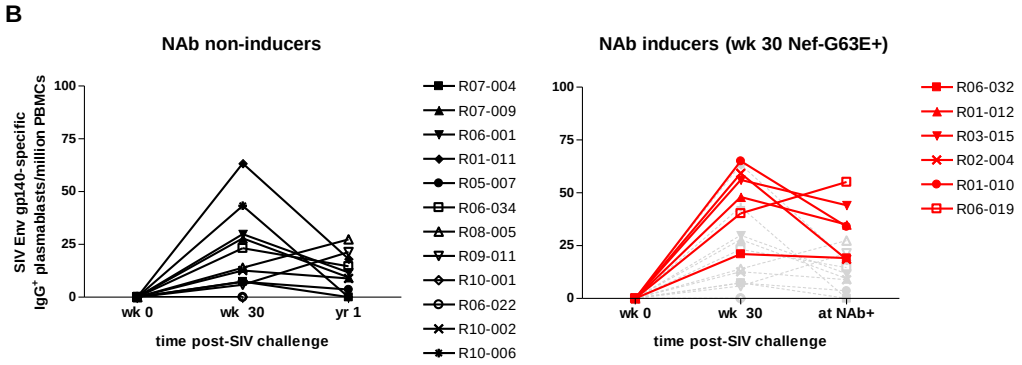
B
NAb non-inducers
NAb inducers (wk 30 Nef-G63E+)
SIV Env gp140-specific IgG+ plasmablasts/million PBMCs
time post-SIV challenge
wk 0
wk 30
yr 1
at NAb+
R07-004
R07-009
R06-001
R01-011
R05-007
R06-034
R08-005
R09-011
R10-001
R06-022
R10-002
R10-006
R06-032
R01-012
R03-015
R02-004
R01-010
R06-019

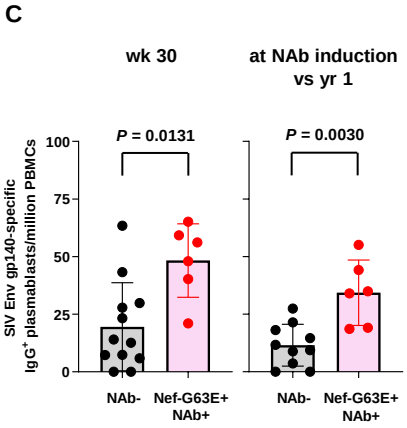
C
wk 30
at NAb induction vs yr 1
P = 0.0131
P = 0.0030
SIV Env gp140-specific IgG+ plasmablasts/million PBMCs
NAb-
Nef-G63E+ NAb+

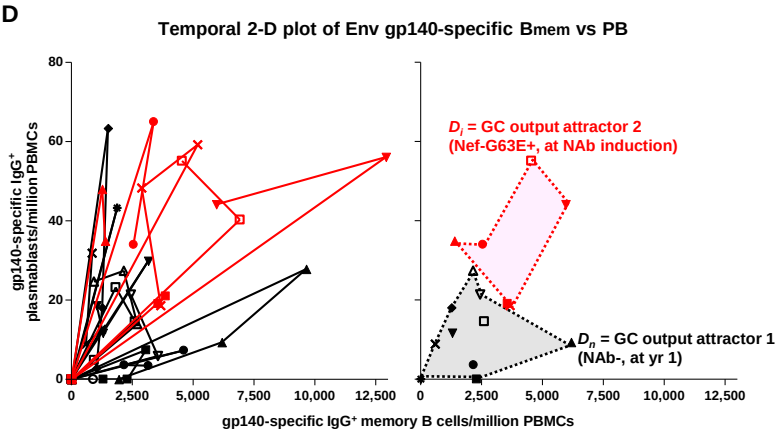
D
Temporal 2-D plot of Env gp140-specific Bmem vs PB
gp140-specific IgG+ plasmablasts/million PBMCs
gp140-specific IgG+ memory B cells/million PBMCs
Di = GC output attractor 2 (Nef-G63E+, at NAb induction)
Dn = GC output attractor 1 (NAb-, at yr 1)

NAb non-inducer cohort (*n* = 19)

MHC-I/ID	SIV$_{mac239}$ neutralization at 1:2 plasma dilution by 10TCID$_{50}$ killing assay (wks p.i.) wk11–20	wk21–30	wk31–40	wk41–50	wk51–60	wk61–70	wk71–80	wk81–90	wk91–104	pVL at 6 mo	Nef G63E at 1 yr	Detected *Mamu* alleles
A+												
R06-037		wk25 -		wk46 +/-			wk72 -	wk87 -	wk95 -	6.4×10^2	- (pVL < 400)	
R07-001		wk25 -		wk42 -				wk88 +/-	wk96 -	< 400	- (pVL < 400)	*A1*032:02*
R07-004		wk25 -		wk46 -		wk64 -	wk74 -	wk86 -		4.5×10^3	+	*B*039:01*
R07-009		wk25 -		wk46 -		wk64 -	wk74 -			4.5×10^3	-	
B+												
R06-001		wk25 -		wk48 -	wk60 -		wk80 -	wk90 -		8.2×10^3	-	
R06-039		wk25 -		wk46 -	wk56 -					8.5×10^6	-	*A1*032:02* , *B*004:01*
E+												
R01-011		wk22 -	wk40 -		wk52 -		wk71 -	wk85 -	wk104 -	1.3×10^5	-	*B*004:01*
R05-007		wk26 -			wk55 +/-		wk71 -	wk89 -	wk97 -	1.6×10^4	-	
R08-007		wk21 -		wk46 -		wk69 -		wk82 +/-		8.5×10^6	-	
R09-011	wk18 -		wk36 -		wk52 -					8.5×10^6	-	
R06-038		wk25 -			wk58 +/-		wk80 +/-		wk95 -	1.1×10^5	-	
J+												
R04-014	wk12 -	wk25 -	wk40 -							1.5×10^5	+ (wk40)	*B*039:01*
R06-022	wk12 -	wk23 -								1.4×10^7	- (wk23)	*B*039:01*
R10-001	wk14 -	wk30 -	wk37 -							1.9×10^7	- (wk37)	*B*039:01*
D+												
R05-006		wk25 -		wk48 -			wk80 -	wk90 -	wk98 -	5.4×10^2	-	*A1*032:02* , *B*004:01*
R06-034		wk25 -		wk42 -		wk61 -	wk80 +/-	wk88 +/-	wk96 -	4.5×10^3	-	*A1*032:02* , *B*004:01*
R08-005		wk25 -		wk48 -		wk68 -			wk100 -	9.0×10^2	-	*A1*032:02* , *B*004:01*
Others												
R10-002	wk14 -				wk59 -				wk104 -	5.7×10^5	-	
R10-006	wk14 -	wk30 -			wk55 -					1.0×10^6	-	

Group	Rhesus ID	mg/ml (IgG)	Collected/pooled (wks post-challenge)	10 $TCID_{50}$ SIV_{mac239} 100% killing titer
NAb (+)	R06-032	30	wk 76	1:16
	R01-012	30	wk 73–87	1:32
	R03-015	30	wk 112	1:8
	R02-004	30	wk 76	1:4
	R01-010	30	wk 77	1:16
	R06-019	30	wk 85	1:4
	R-360	30	wk 60–86	1:4
	R02-007	30	wk 42–70	1:32
	R05-010	30	wk 71	1:64
NAb (-)	R01-011	42	wk 104	< 1:2
uninfected	pooled	36	-	< 1:2

A

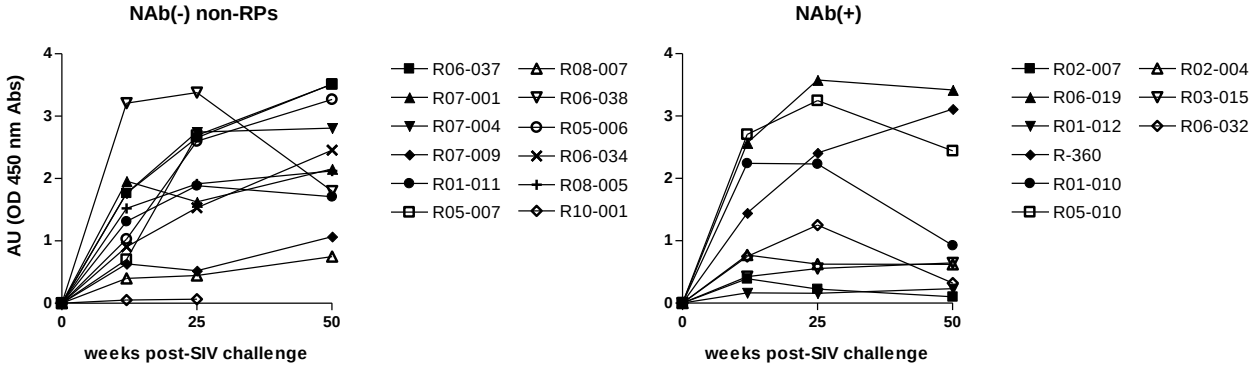
NAb(-) non-RPs
AU (OD 450 nm Abs)
weeks post-SIV challenge
R06-037
R07-001
R07-004
R07-009
R01-011
R05-007
R08-007
R06-038
R05-006
R06-034
R08-005
R10-001
NAb(+)
AU (OD 450 nm Abs)
weeks post-SIV challenge
R02-007
R06-019
R01-012
R-360
R01-010
R05-010
R02-004
R03-015
R06-032

B

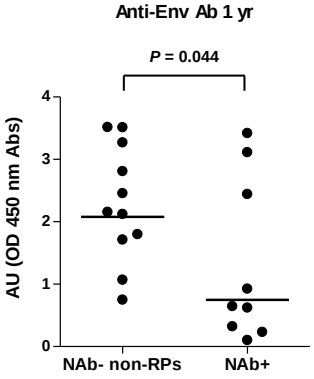
Anti-Env Ab 1 yr
P = 0.044
AU (OD 450 nm Abs)
NAb- non-RPs
NAb+

C

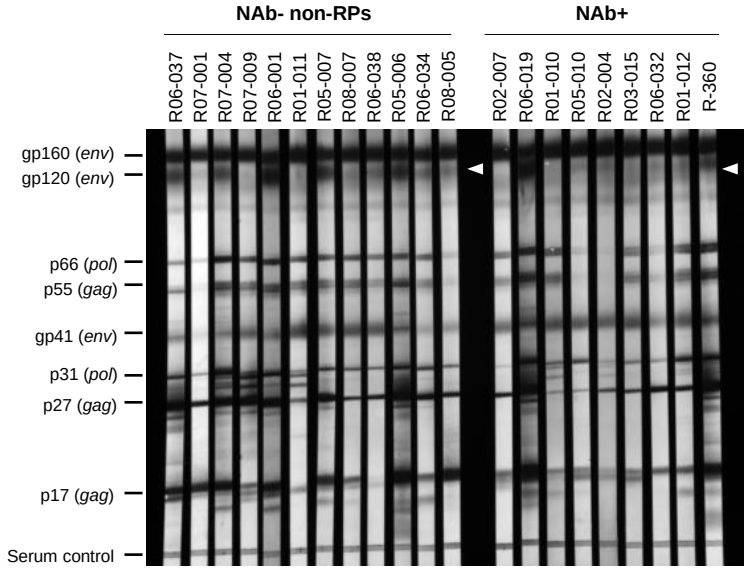
NAb- non-RPs
NAb+
R06-037
R07-001
R07-004
R07-009
R06-001
R01-011
R05-007
R08-007
R06-038
R05-006
R06-034
R08-005
R02-007
R06-019
R01-010
R05-010
R02-004
R03-015
R06-032
R01-012
R-360
gp160 (env)
gp120 (env)
p66 (pol)
p55 (gag)
gp41 (env)
p31 (pol)
p27 (gag)
p17 (gag)
Serum control

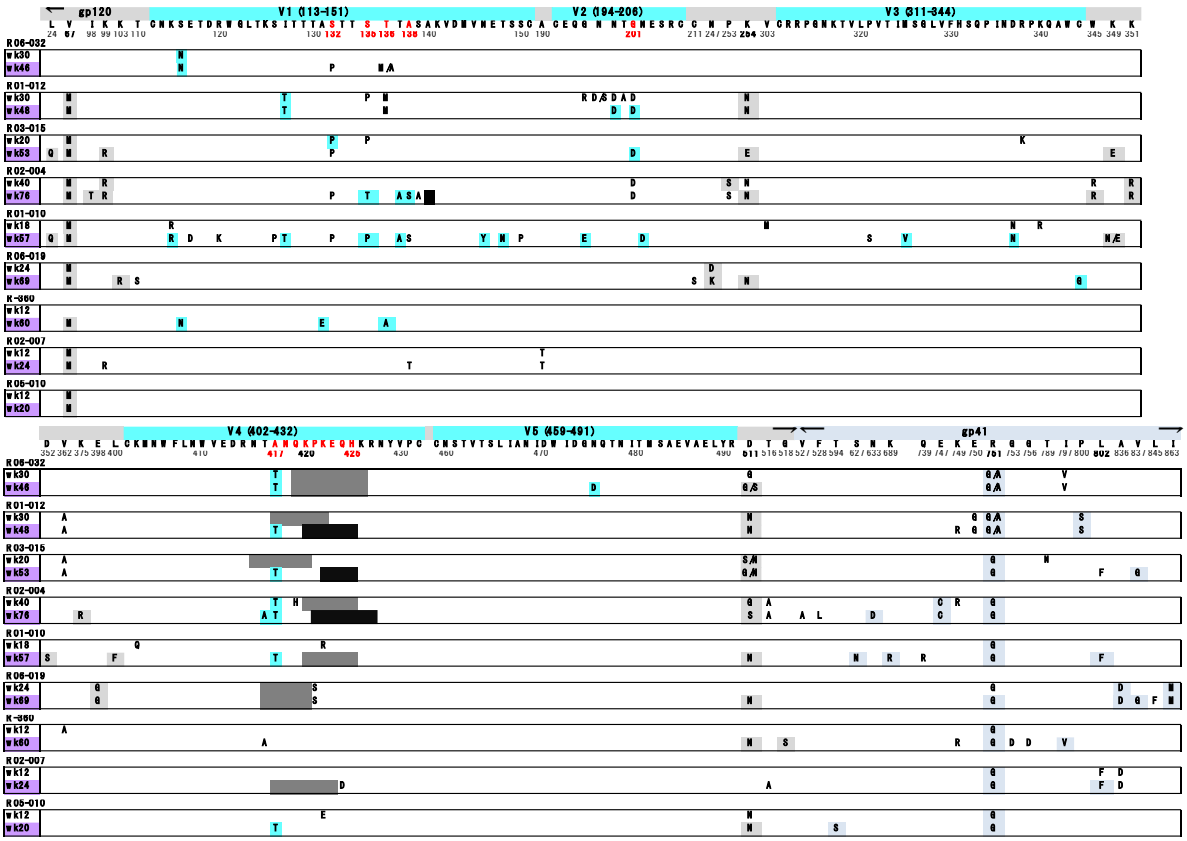
gp120
V1 (113-151)
V2 (194-206)
V3 (311-344)
R06-032
wk30
wk46
R01-012
wk30
wk48
R03-015
wk20
wk53
R02-004
wk40
wk76
R01-010
wk18
wk57
R06-019
wk24
wk69
K-560
wk12
wk60
R02-007
wk12
wk24
R05-010
wk12
wk20
V4 (402-432)
V5 (459-491)
gp41

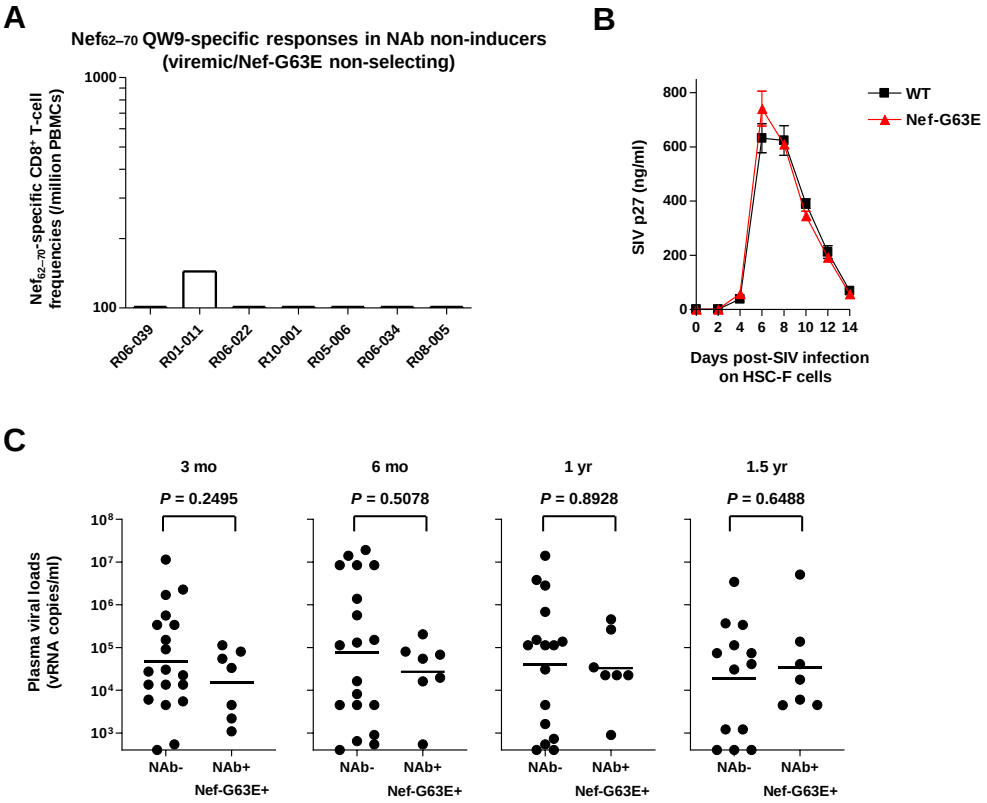
A
Nef62–70 QW9-specific responses in NAb non-inducers
(viremic/Nef-G63E non-selecting)
Nef62–70-specific CD8+ T-cell frequencies (/million PBMCs)
1000
100
R06-039
R01-011
R06-022
R10-001
R05-006
R06-034
R08-005
B
SIV p27 (ng/ml)
800
600
400
200
0
0 2 4 6 8 10 12 14
Days post-SIV infection on HSC-F cells
WT
Nef-G63E
C
3 mo
6 mo
1 yr
1.5 yr
P = 0.2495
P = 0.5078
P = 0.8928
P = 0.6488
Plasma viral loads (vRNA copies/ml)
10^8
10^7
10^6
10^5
10^4
10^3
NAb-
NAb+
Nef-G63E+

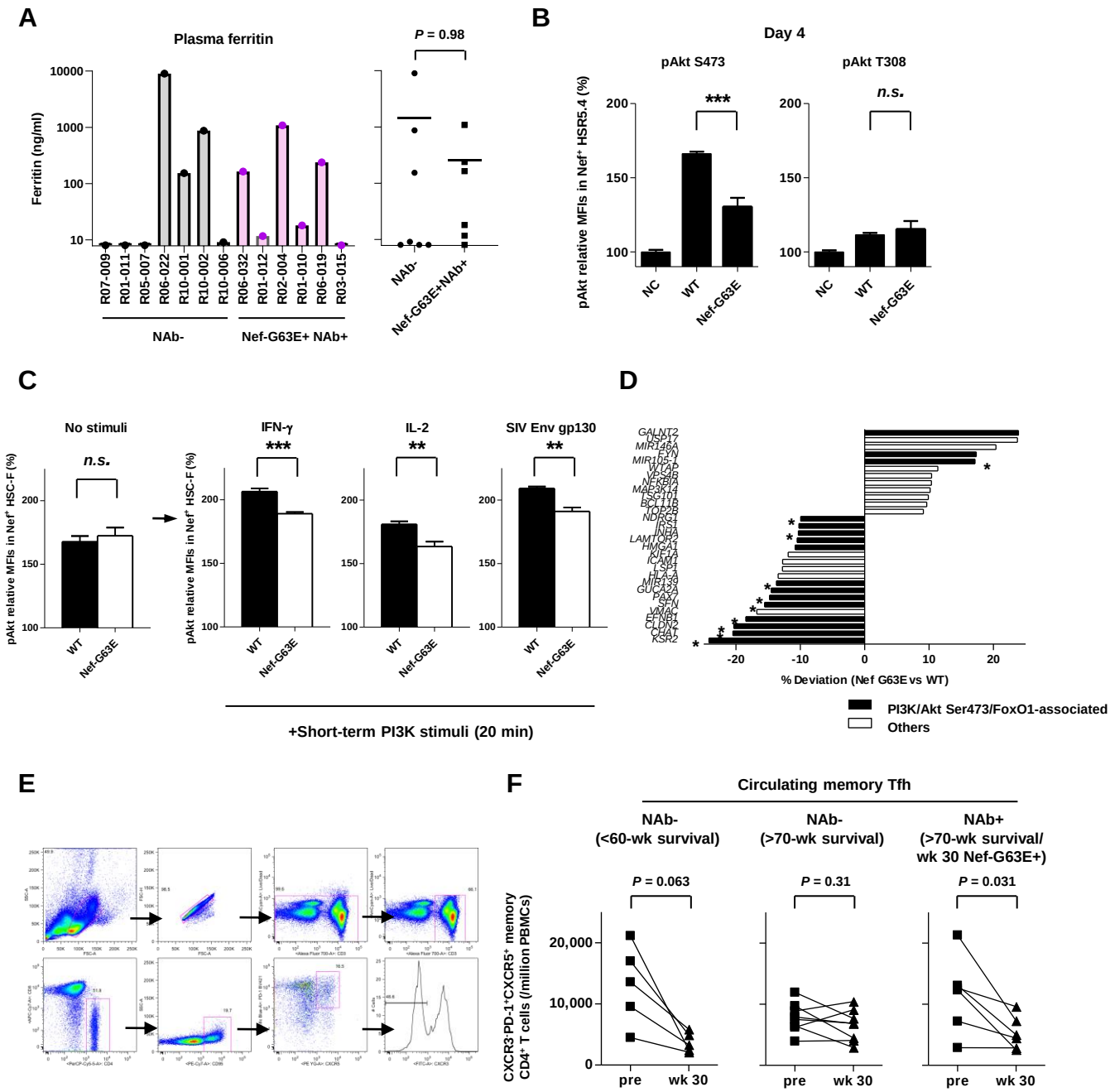
A
Plasma ferritin
Ferritin (ng/ml)
10000
1000
100
10
R07-009
R01-011
R05-007
R06-022
R10-001
R10-002
R10-006
R06-032
R01-012
R02-004
R01-010
R06-019
R03-015
NAb-
Nef-G63E+ NAb+
P = 0.98
NAb-
Nef-G63E+NAb+
B
Day 4
pAkt S473
pAkt T308
pAkt relative MFIs in Nef+ HSR5.4 (%)
***
n.s.
200
150
100
NC
WT
Nef-G63E
C
No stimuli
IFN-γ
IL-2
SIV Env gp130
pAkt relative MFIs in Nef+ HSC-F (%)
n.s.
***
**
**
WT
Nef-G63E
+Short-term PI3K stimuli (20 min)
D
GALNT2
USP17
MIR146A
FYN
MIR105-1
WTAP
VPS4B
NFKBIA
MAP3K14
TSG101
BCL11B
TOP2B
NDRG1
IRS1
INPA
LAMTOR2
HMGA1
KIF1A
ICAM1
LSP1
HLA-A
MIR139
GUCA2A
PAX2
SFN
VMAC
EFNB1
CLDN2
CHAT
KSR2
-20
-10
0
10
20
% Deviation (Nef G63E vs WT)
PI3K/Akt Ser473/FoxO1-associated
Others
E
F
Circulating memory Tfh
NAb-
(<60-wk survival)
NAb-
(>70-wk survival)
NAb+
(>70-wk survival/
wk 30 Nef-G63E+)
P = 0.063
P = 0.31
P = 0.031
CXCR3-PD-1+CXCR5+ memory
CD4+ T cells (/million PBMCs)
20,000
10,000
0
pre
wk 30

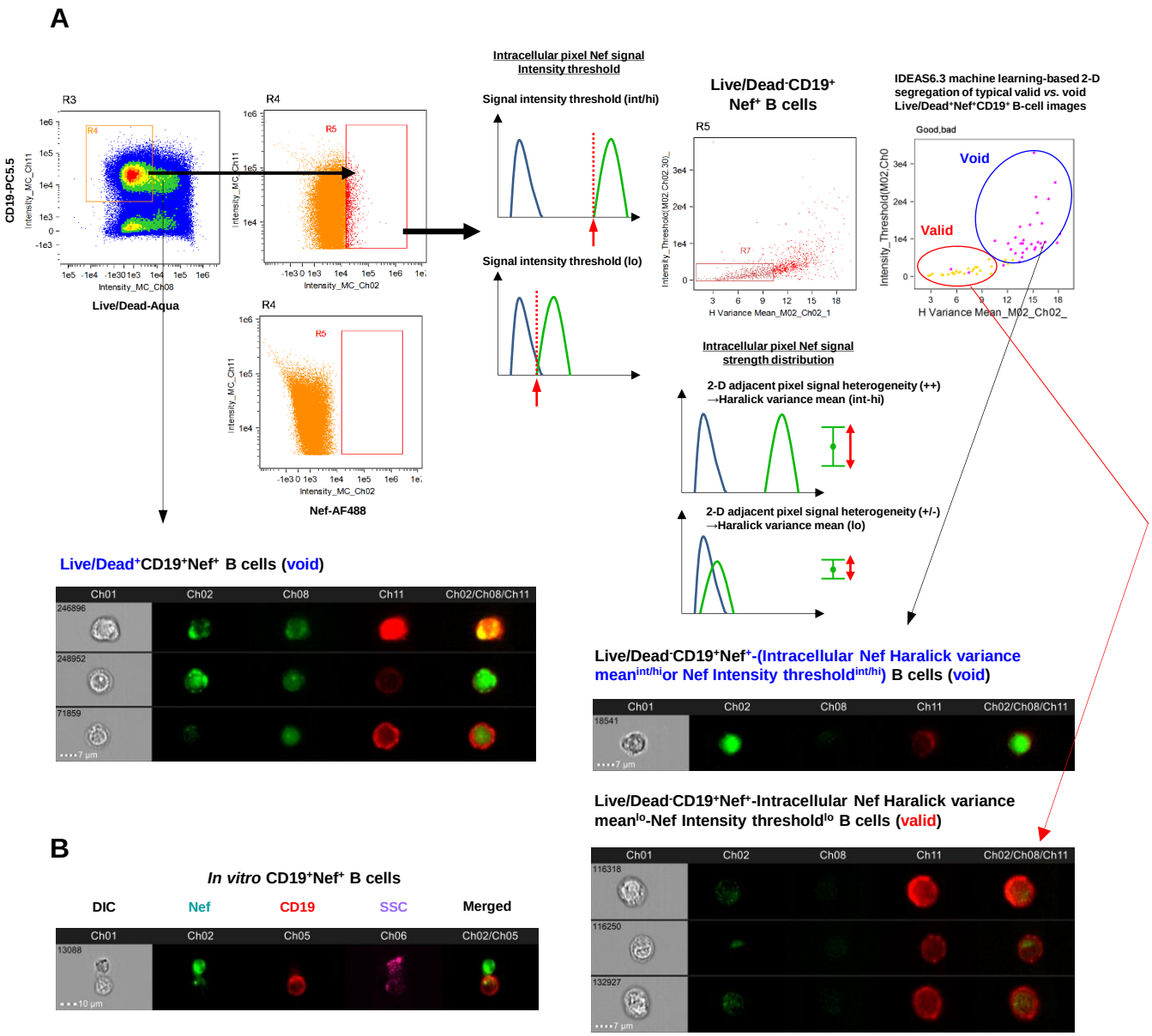
A
CD19-PC5.5
R3
R4
Intensity_MC_Ch11
Intensity_MC_Ch08
Live/Dead-Aqua
R4
R5
Intensity_MC_Ch11
Intensity_MC_Ch02
R4
R5
Intensity_MC_Ch11
Intensity_MC_Ch02
Nef-AF488
Intracellular pixel Nef signal
Intensity threshold
Signal intensity threshold (int/hi)
Signal intensity threshold (lo)
Live/Dead-CD19+
Nef+ B cells
R5
R7
H Variance Mean_M02_Ch02_1
IDEAS6.3 machine learning-based 2-D
segregation of typical valid vs. void
Live/Dead+Nef+CD19+ B-cell images
Good,bad
Void
Valid
H Variance Mean_M02_Ch02_
Intracellular pixel Nef signal
strength distribution
2-D adjacent pixel signal heterogeneity (++)
→Haralick variance mean (int-hi)
2-D adjacent pixel signal heterogeneity (+/-)
→Haralick variance mean (lo)
Live/Dead+CD19+Nef+ B cells (void)
Ch01
Ch02
Ch08
Ch11
Ch02/Ch08/Ch11
246896
248952
71859
7 µm
Live/Dead-CD19+Nef+-(Intracellular Nef Haralick variance
mean int/hi or Nef Intensity threshold int/hi) B cells (void)
Ch01
Ch02
Ch08
Ch11
Ch02/Ch08/Ch11
18541
7 µm
Live/Dead-CD19+Nef+-Intracellular Nef Haralick variance
mean lo-Nef Intensity threshold lo B cells (valid)
Ch01
Ch02
Ch08
Ch11
Ch02/Ch08/Ch11
116318
116250
132927
7 µm
B
In vitro CD19+Nef+ B cells
DIC
Nef
CD19
SSC
Merged
Ch01
Ch02
Ch05
Ch06
Ch02/Ch05
13088
10 µm

A

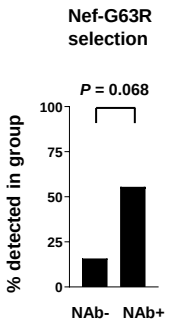
Nef-G63R selection
P = 0.068
% detected in group
100
75
50
25
0
NAb-
NAb+

B

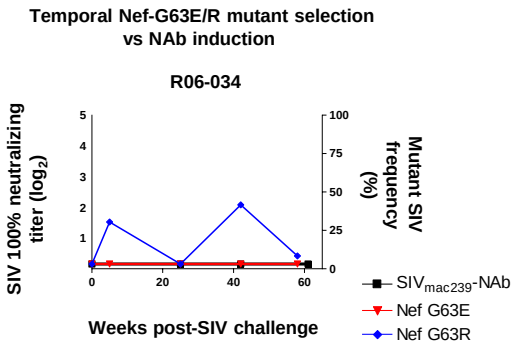
Temporal Nef-G63E/R mutant selection vs NAb induction
R06-034
SIV 100% neutralizing titer (log2)
Mutant SIV frequency (%)
Weeks post-SIV challenge
SIVmac239-NAb
Nef G63E
Nef G63R

C

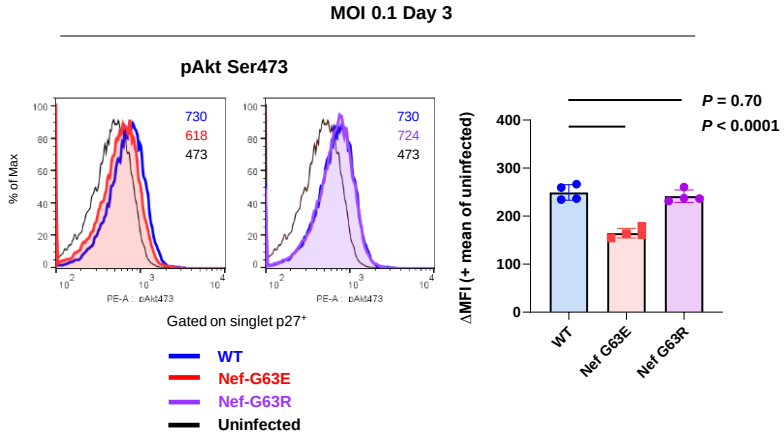
MOI 0.1 Day 3
pAkt Ser473
% of Max
730
618
473
730
724
473
PE-A :: pAkt473
Gated on singlet p27+
WT
Nef-G63E
Nef-G63R
Uninfected
ΔMFI (+ mean of uninfected)
P = 0.70
P < 0.0001
WT
Nef G63E
Nef G63R

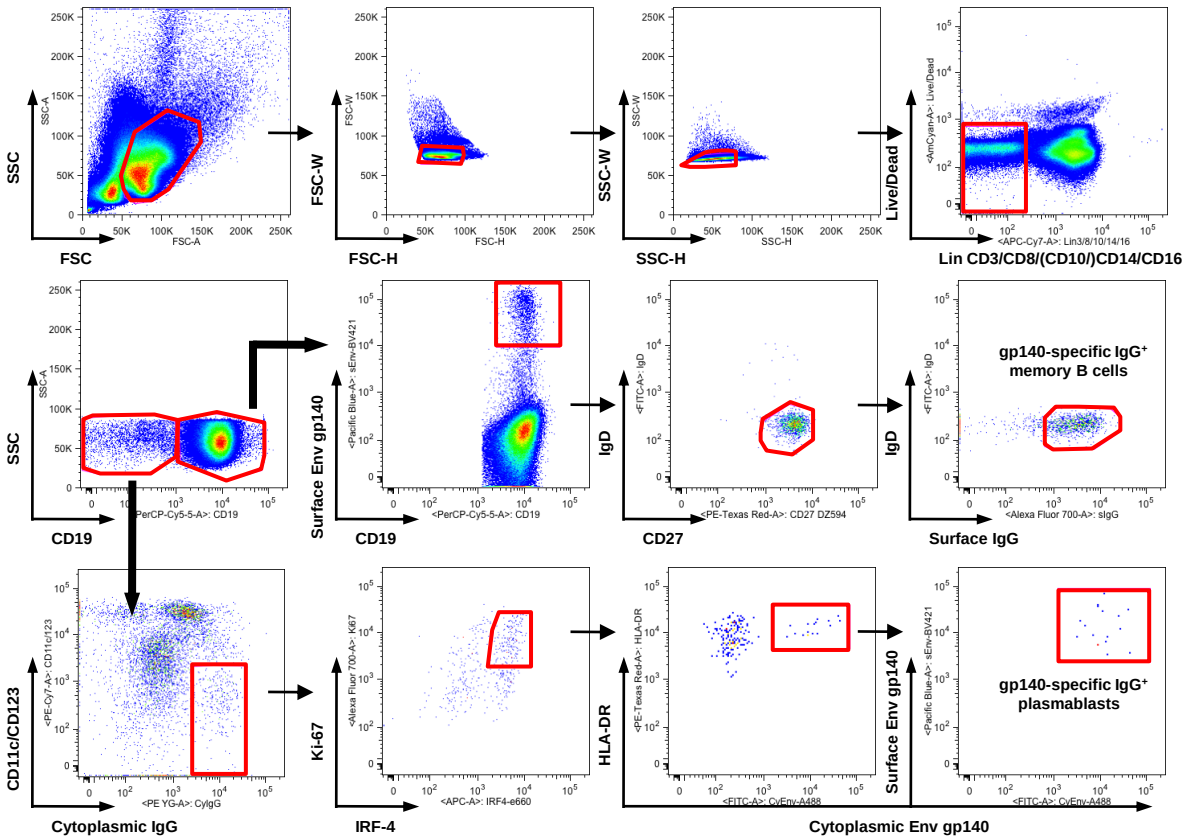
SSC
FSC
FSC-W
FSC-H
SSC-W
SSC-H
Live/Dead
Lin CD3/CD8/(CD10/)CD14/CD16
CD19
Surface Env gp140
IgD
CD27
Surface IgG
gp140-specific IgG+ memory B cells
CD11c/CD123
Cytoplasmic IgG
Ki-67
IRF-4
HLA-DR
Cytoplasmic Env gp140
gp140-specific IgG+ plasmablasts

Key Resources Table				
Reagent type (species) or resource	**Designation**	**Source or reference**	**Identifiers**	**Additional information**
gene (*Lentivirus*)	*env*, *nef*	GenBank	M33262.1	SIV_{mac239}
strain, strain background (*Lentivirus*)	SIV_{mac239}	PMID: 2032289		Obtained via COS-1 transfection of pBR_{mac239} and repropagation on MT4-R5 cells
strain, strain background (*Escherichia coli*)	One Shot™ TOP10 Chemically Competent *E. coli*	Invitrogen (Thermo Fisher Scientific)	Cat#:C404003	For subcloning sequencing
cell line (*Homo-sapiens*)	MT4-R5	PMID: 27122584		STR profiling (+)
cell line (*Chlorocebus aethiops*)	COS-1	ATCC	CRL-1650	STR profiling (+)
cell line (*Macaca fascicularis*)	HSC-F cells (CD4+ T-cell line)	PMID: 8610465	Gift from producer (Dr. Hirofumi Akari)	
cell line (*Macaca mulatta*)	HSR5.4 cells (CD4+ T-cell line)	PMID: 8610465	Gift from producer (Dr. Hirofumi Akari)	
cell line (*Homo-sapiens*)	Ramos B cell line	ATCC	CRL-1596	STR profiling (+)
biological sample (*Macaca mulatta*)	Primary simian PBMCs from SIV-infected macaques	Japan SLC	http://www.jslc.co.jp/service/	Cryopreserved from *Macaca mulatta*

biological sample (*Macaca mulatta*)	Primary simian lymph node cells from SIV-infected macaques	Japan SLC	http://www.jslc.co.jp/service/	Cryopreserved from *Macaca mulatta*
antibody	Mouse monoclonal anti-human CD4-FITC (M-T477)	BD Pharmingen	Cat#556615	FACS (5 µl per test)
antibody	Mouse monoclonal anti-human CD8-PerCP (SK1)	BD Biosciences	Cat#347314	FACS (5 µl per test)
antibody	Mouse monoclonal anti-human CD3-APC (SP34-2)	BD Pharmingen	Cat#557597	FACS (5 µl per test)
antibody	Mouse monoclonal anti-human IFN-γ-PE (4S.B3)	BioLegend	Cat#502510	FACS (5 µl per test)
antibody	Mouse monoclonal anti-SIV_{mac251} Gag p27 mAb	ABL	Cat#4324	FACS (1:500 with conjugation)
antibody	Mouse monoclonal anti-SIV_{mac251} Nef mAb (clone 17)	Themo Fisher Scientific	Cat#MA1-71522	FACS, PLA, immuno-blotting and imaging cytometry (FACS and imaging cytometry, 1:500 with conjugation; PLA, 1:100; immuno-blotting, 1:1000)
antibody	Mouse IgG1 isotype control mAb (P3.6.2.8.1)	Themo Fisher Scientific	Cat#14-4714-85	PLA (1:100)

antibody	Rabbit monoclonal Alexa Fluor 488-conjugated anti-human phospho-Akt (Ser473) (D9E)	Cell Signaling Technology	Cat#4071	FACS (5 µl per test)
antibody	Rabbit monoclonal Alexa Fluor 488-conjugated anti-human phospho-Akt (Thr308) (C31E5E)	Cell Signaling Technology	Cat#2918	FACS (5 µl per test)
antibody	Rabbit monoclonal PE-conjugated anti-human phospho-Akt (Ser473) (D9E)	Cell Signaling Technology	Cat#5315	FACS and imaging cytometry (1:100)
antibody	Rabbit monoclonal Alexa Fluor 647-conjugated anti-human phospho-Akt (Ser473) (D9E)	Cell Signaling Technology	Cat#4075	FACS (5 µl per test)
antibody	Rabbit monoclonal Alexa Fluor 647-conjugated anti-human phospho-Akt (Thr308) (C31E5E)	Cell Signaling Technology	Cat#3375	FACS (5 µl per test)
antibody	Mouse monoclonal anti-human CD19-PC-5.5 (J3-119)	Beckman Coulter	Cat#66328	FACS and imaging cytometry (5 µl per test)
antibody	Mouse monoclonal anti-human CD4, purified (clone L200)	BD Biosciences	Cat#550625	FACS (25 µg/ml per test for blockade)
antibody	Mouse monoclonal anti-human CD3-	BD Pharmingen	Cat#557757	FACS (5 µl per test)

	APC-Cy7 (SP34-2)			
antibody	Mouse monoclonal anti-human CD8-APC-Cy7 (RPA-T8)	BD Pharmingen	Cat#557760	FACS (5 µl per test)
antibody	Mouse monoclonal anti-human CD14-APC-Cy7 (M5E2)	BioLegend	Cat#301820	FACS (5 µl per test)
antibody	Mouse monoclonal anti-human CD16-APC-Cy7 (3G8)	BioLegend	Cat#302018	FACS (5 µl per test)
antibody	Mouse monoclonal anti-human CD10-APC-Cy7 (HI10a)	BioLegend	Cat#312212	FACS (5 µl per test)
antibody	Mouse monoclonal anti-human CD11c-PE-Cy7 (3.9)	BioLegend	Cat#301608	FACS (5 µl per test)
antibody	Mouse monoclonal anti-human CD123-PE-Cy7 (6H6)	BioLegend	Cat#306010	FACS (5 µl per test)
antibody	Mouse monoclonal anti-human HLA-DR-PE-Texas Red (TU36)	Invitrogen (Thermo Fisher Scientific)	Cat# MHLDR17	FACS (5 µl per test)
antibody	Mouse monoclonal anti-human CD27-PE/Dazzle 594 (M-T271)	BioLegend	Cat#356422	FACS (5 µl per test)
antibody	Mouse monoclonal anti-human CD10-PE-Cy7 (HI10a)	BioLegend	Cat#312214	FACS (5 µl per test)

antibody	Rabbit polyclonal anti-human IgD-FITC $F(ab')_2$	DaKo	Cat#F0189	FACS (5 µl per test)
antibody	Mouse monoclonal anti-human CD38-Alexa 647 (AT1)	Santa Cruz Biotechnology	Cat# sc-7325 AF647	FACS (5 µl per test)
antibody	Mouse monoclonal anti-human IgG-Alexa 700 (G18-145)	BD Pharmingen	Cat#561296	FACS (5 µl per test)
antibody	Mouse monoclonal anti-human CD138-PE (DL-101)	eBioscience (Thermo Fisher Scientific)	Cat#12-1389-42	FACS (5 µl per test)
antibody	Mouse monoclonal anti-human IgG-PE (G18-145)	BD Biosciences	Cat#555787	FACS (5 µl per test)
antibody	Rat monoclonal anti-human/mouse IRF4-eFluor 660 (3E4)	eBioscience (Thermo Fisher Scientific)	Cat#50-9858-80	FACS (5 µl per test)
antibody	Mouse monoclonal anti-human Ki67-Alexa 700 (B56)	BD Pharmingen	Cat#561277	FACS (5 µl per test)
antibody	Mouse monoclonal anti-human anti-CD4-PerCP (L200)	BD Pharmingen	Cat#550631	FACS (5 µl per test)
antibody	Mouse monoclonal anti-human anti-CD3-Alexa 700 (SP34-2)	BD Pharmingen	Cat#561805	FACS (5 µl per test)
antibody	Mouse monoclonal anti-human anti-CD95-PE-Cy7 (DX2)	eBioscience (Thermo Fisher Scientific)	Cat#25-0959-42	FACS (5 µl per test)

antibody	Mouse monoclonal anti-human anti-CXCR5-PE (87.1)	eBioscience (Thermo Fisher Scientific)	Cat#12-1859-42	FACS (5 µl per test)
antibody	Mouse monoclonal anti-human PD-1-Brilliant Violet 421 (EH12.2H7)	BioLegend	Cat#329920	FACS (5 µl per test)
antibody	Mouse monoclonal anti-human CXCR3-Alexa 488 (G025H7)	BioLegend	Cat#353710	FACS (5 µl per test)
antibody	Mouse monoclonal anti-human HLA-ABC-FITC (G46-2.6)	BD Biosciences	Cat#557348	FACS (5 µl per test)
antibody	Mouse monoclonal anti-human CXCR4-APC (12G5)	BioLegend	Cat#306510	FACS (5 µl per test)
antibody	Mouse monoclonal anti-human BST2-Alexa647 (RS38E)	BioLegend	Cat#348404	FACS (5 µl per test)
antibody	Mouse monoclonal anti-human CD20 (2H7)	Biolegend	Cat#302324	FACS (5 µl per test)
antibody	Rabbit monoclonal anti-GβL (86B8)	Cell Signaling Technology	Cat#3274	PLA (1:100)
antibody	Rabbit monoclonal anti-mTOR (7C10)	Cell Signaling Technology	Cat#2983	PLA (1:100)
antibody	Rabbit polyclonal anti-human PI3K p85	Merck Millipore	Cat#ABS1856	PLA (1:100)

antibody	Rabbit monoclonal anti-PI3 Kinase p110α (C73F8)	Cell Signaling Technology	Cat#4249	PLA (1:100)
antibody	Goat polyclonal HRP-conjugated anti-monkey IgG (H+L)	Bethyl Laboratory	Cat# A140-102P	ELISA (1:1000)
antibody	Rabbit monoclonal anti-Sin1 (D7G1A)	Cell Signaling Technology	Cat#12860	Co-immuno-precipitation (1:50)
antibody	Mouse TrueBlot™ ULTRA anti-mouse Ig HRP (eB144)	Rockland Immuno-chemicals	Cat# 18-8817-30	Immuno-blotting (1:1000)
antibody	Mouse monoclonal anti-CD3 (FN-18)	Abcam	Cat#ab25109	Stimulation assay (1 µg/ml)
antibody	CD20 MicroBeads, non-human primate	Miltenyi Biotec	Cat#130-091-105	
recombinant DNA reagent	pBR_{mac239}	PMID: 2032289	GenBank M33262	coding full sequence of *nef*-open SIV_{mac239}
sequence-based reagent	9520GA-F	This paper	PCR primers	GGGACAG AAATACAA TCAGGAA CAGTATAT GAATACTC CATGGAG
sequence-based reagent	9520GA-R	This paper	PCR primers	CTCCATG GAGTATTC ATATACTG TTCCTGAT TGTATTTC TGTCCC
sequence-based reagent	9519GA-F	This paper	PCR primers	GAGGGAC AGAAATAC AATCAGA GACAGTA

				TATGAATA CTCCAT
sequence-based reagent	9519GA-R	This paper	PCR primers	ATGGAGT ATTCATAT ACTGTCTC TGATTGTA TTTCTGTC CCTC
peptide, recombinant protein	Peptide Nef_{62-70}	Sigma Aldrich	CTL epitope peptide	QGQYMNT PW
peptide, recombinant protein	Peptide Nef_{62-70}.G63E	Sigma Aldrich	Mutant CTL epitope peptide	QEQYMNT PW
peptide, recombinant protein	Peptide Nef_{62-70}.G63R	Sigma Aldrich	Mutant CTL epitope peptide	QRQYMNT PW
peptide, recombinant protein	GolgiStop	BD Biosciences	Cat#554724	
peptide, recombinant protein	recombinant SIV_{mac251} Env gp130	ImmunoDx	Cat#5001	Ligand stimulation assay (10 µg/ml)
peptide, recombinant protein	recombinant human IL-2	Roche Diagnostics	Cat#1114752 8001	Ligand stimulation assay (100 IU/ml)
peptide, recombinant protein	recombinant human IFN-γ	Gibco (Thermo Fisher Scientific)	Cat#PHC403 3	Ligand stimulation assay (40 ng/ml)
peptide, recombinant protein	recombinant SIV_{mac239} Env gp140 (biotin-conjugated)	Immune Technology	Cat#IT-001-140p	FACS and imaging cytometry (10µg/ml for probing)

peptide, recombinant protein	streptavidin-Brilliant Violet 421	BioLegend	Cat#405225	FACS (1:100)
peptide, recombinant protein	streptavidin-Alexa Fluor 488	BioLegend	Cat#405235	FACS (1:100)
peptide, recombinant protein	streptavidin-PE-Cy7	BioLegend	Cat#405206	Imaging cytometry (1:100)
peptide, recombinant protein	Recombinant Human IL-4 Protein (carrier-free)	R&D Systems	Cat# 204-IL-050/CF	Functional assay (40 ng/ml)
commercial assay or kit	High Pure Viral RNA kit	Roche Diagnostics	Cat#11858882001	
commercial assay or kit	SIV p27 ELISA	ABL	Cat#5436	
commercial assay or kit	SureBlue TMB 1-Component Microwell Peroxidase Substrate	KPL	Cat# 5120-0075	
commercial assay or kit	Prime-Script one-step RT-PCR kit v2	TaKaRa	Cat#RR055A	
commercial assay or kit	KOD-Plus v2	Toyobo	Cat#KOD-211	
commercial assay or kit	Zero Blunt TOPO PCR cloning kit for sequencing	Invitrogen (Thermo Fisher Scientific)	Cat#K287540	
commercial assay or kit	Cytofix/Cytoperm kit	BD Biosciences	Cat#554714	
commercial assay or kit	Monkey Ferritin (Sandwich	LS Bio	Cat#LS-F36490-1	

	ELISA) ELISA Kit			
commercial assay or kit	QuikChange II XL site-directed mutagenesis kit	Agilent Technologies	Cat#200522	
commercial assay or kit	RNeasy Plus Mini kit	Qiagen	Cat#74136	
commercial assay or kit	GeneChip WT Plus reagent	Affymetrix (Thermo Fisher Scientific)	Cat#902280	
commercial assay or kit	GeneChip Human Gene 2.0 ST Array	Affymetrix (Thermo Fisher Scientific)	Cat#902113	
commercial assay or kit	Alexa Fluor™ 488 Antibody Labeling Kit	Invitrogen (Thermo Fisher Scientific)	Cat#A20181	
commercial assay or kit	Alexa Fluor™ 647 Antibody Labeling Kit	Invitrogen (Thermo Fisher Scientific)	Cat# A20186	
commercial assay or kit	Duolink In Situ PLA Probe anti-mouse PLUS	Sigma (Merck)	Cat#DUO92001	
commercial assay or kit	Duolink In Situ PLA Probe anti-rabbit MINUS	Sigma (Merck)	Cat#DUO92005	
commercial assay or kit	Duolink flow PLA detection kit-Green	Sigma (Merck)	Cat#DUO94002	
commercial assay or kit	FuGENE6	Promega	Cat#E2691	
commercial assay or kit	Capturem IP & Co-IP Kit	Clontech/Takara	Cat#635721	

software, algorithm	FACS Diva	BD Biosciences	http://www.bdbiosciences.com/jp/instruments/software/facsdiva/	
software, algorithm	FlowJo v10.7.1	BD/Treestar	https://www.flowjo.com/solutions/flowjo	
software, algorithm	Affymetrix Expression Console Software	Affymetrix/Thermo Fisher Scientific	https://www.thermofisher.com/jp/ja/home/life-science/microarray-analysis/microarray-analysis-instruments-software-services/microarray-analysis-software/affymetrix-transcriptome-analysis-console-software.html	
software, algorithm	IDEAS 6.3 (+Machine learning module)	Amnis/Merck Millipore/Luminex	https://www.luminexcorp.com/imaging-flow-cytometry/	
software, algorithm	Image Lab software	BioRad	https://www.bio-rad.com/en-jp/product/image-lab-software	
software, algorithm	Prism 8	GraphPad Software	https://www.graphpad.com	
other	LIVE/DEAD® Fixable Aqua stain	Invitrogen (Thermo Fisher Scientific)	Cat#L34957	FACS and imaging cytometry (1:1000)

other	APC Annexin V	Biolegend	Cat#640920	FACS (5 µl per 100 µl test)
other	Annexin V Binding Buffer	Biolegend	Cat#422201	Diluent
other	LIVE/DEAD® Fixable Near-IR stain	Invitrogen (Thermo Fisher Scientific)	Cat#L10119	FACS (1:1000)
other	phorbol-12-myristate-13-acetate (PMA)	Sigma/Merck	Cat#P1585	Stimulation assay (10 ng/ml)
other	ionomycin	Sigma/Merck	Cat#I3909	Stimulation assay (10 ng/ml)
other	4–15% Mini-PROTEAN® TGX™ Precast Protein Gels	BioRad	Cat#4561085	
other	SuperSignal West Pico	Thermo Fisher Scientific	Cat#34580	